

A NEW APPROACH FOR TURBULENT SIMULATIONS IN  
COMPLEX GEOMETRIES

by  
Daniel M. Israel

---

Copyright © Daniel M. Israel 2005

A Dissertation Submitted to the Faculty of the  
DEPARTMENT OF AEROSPACE & MECHANICAL ENGINEERING

In Partial Fulfillment of the Requirements  
For the Degree of

DOCTOR OF PHILOSOPHY  
WITH A MAJOR IN AEROSPACE ENGINEERING

In the Graduate College  
THE UNIVERSITY OF ARIZONA

2 0 0 5

THE UNIVERSITY OF ARIZONA  
GRADUATE COLLEGE

As members of the Dissertation Committee, we certify that we have read the dissertation

prepared by Daniel M. Israel

entitled “A New Approach for Turbulent Simulations in Complex Geometries”

and recommend that it be accepted as fulfilling the dissertation requirement for the

Degree of Doctor of Philosophy

\_\_\_\_\_  
Hermann F. Fasel Date: July 26, 2005

\_\_\_\_\_  
Edward Kerschen Date: July 26, 2005

\_\_\_\_\_  
Jeffrey Jacobs Date: July 26, 2005

\_\_\_\_\_  
Anatoli Tumin Date: July 26, 2005

\_\_\_\_\_  
Robert Indik Date: July 26, 2005

Final approval and acceptance of this dissertation is contingent upon the candidate's submission of the final copies of the dissertation to the Graduate College.

I hereby certify that I have read this dissertation prepared under my direction and recommend that it be accepted as fulfilling the dissertation requirement.

\_\_\_\_\_  
Dissertation Director: Hermann F. Fasel Date: July 26, 2005

## STATEMENT BY AUTHOR

This dissertation has been submitted in partial fulfillment of requirements for an advanced degree at The University of Arizona and is deposited in the University Library to be made available to borrowers under rules of the Library.

Brief quotations from this dissertation are allowable without special permission, provided that accurate acknowledgment of source is made. Requests for permission for extended quotation from or reproduction of this manuscript in whole or in part may be granted by the copyright holder.

SIGNED: \_\_\_\_\_  
Daniel M. Israel

## ACKNOWLEDGMENTS

The heavens tell the glory of God, and the firmament  
speaks of his handiwork.

PSALMS 19:1

It is with a heart full of gratitude to the Almighty that I present this dissertation, praising him by expounding on a small part of his works. May the wondrous discoveries of science continue to be an inspiration to those who seek truth through the light of Torah.

A special thank you to my advisor, Dr. Hermann Fasel, who has waited for this dissertation as long as I have, and whose direction and patience has allowed me to develop as a researcher. Thanks as well to my committee, Drs. Robert Indik, Jeffery Jacobs, Edward Kerschen, and Anatoli Tumin for all their time, patience, and helpful feedback.

The number of teachers and mentors whose help getting me to this point has earned my sincerest gratitude is too numerous to list, but a few deserve special mention. Thanks to Drs. Vittorio Canuto, Jeffery Chasnov, and Oleg Schilling for introducing me to the field of turbulence during my time at the NASA Goddard Institute for Space Science. And special thanks to Dr. John Lumley for allowing a lowly undergraduate in his turbulence course.

I also must acknowledge the support of the NASA Langley Research Center through the Graduate Student Research Program Fellowship, and in particular the help and collaboration of several individuals at LaRC. Thanks to Dr. Bart Singer, my supervisor during the GSRP Fellowship. Thanks to Drs. Avi Seifert and David Greenblatt for providing experimental data and generous amounts of time to discuss them. Dr. Christopher Rumsey provided invaluable help with CFL3D. And thanks to Dr. Thomas Gatski for his continued interest and encouragement.

All research is a collaboration. I am therefore indebted to all my colleagues at the University of Arizona Computational Fluid Dynamics Laboratory. In particular I want to thank Drs. Hubert Meitz, Cary Bachman, Jurgen Seidel, and Stefan Wernz for many helpful discussions and for allowing me to bounce ideas off of them. Thanks to Dr. Dominic von Terzi for many discussions and his feedback on this manuscript, to Dr. Dieter Postl for his collaboration on the “hump” model, and Dr. Paul Harris for his code. And thanks to Pietro Valsecchi for taking over the very time consuming job of systems administrator.

Finally, I want to thank all my friends and family in Tucson, for their years of support. I also wish to thank my parents, Philip and Lenore Israel, the memory of whom has been a constant source of inspiration.

## DEDICATION

To my parents

Philip Israel

The righteous walk in perfection, happy are their sons after them. PROVERBS 20:7

and

Lenore Israel

Give her the fruit of her hand, and let her be praised in the gates for her own deeds.  
PROVERBS 31:31

# CONTENTS

LIST OF FIGURES . . . . .	<b>9</b>
LIST OF TABLES . . . . .	<b>11</b>
NOMENCLATURE . . . . .	<b>12</b>
ABSTRACT . . . . .	<b>16</b>
CHAPTER 1. INTRODUCTION . . . . .	<b>18</b>
1.1. A Brief History of Turbulence Modeling . . . . .	22
1.1.1. Early History . . . . .	22
1.1.2. Reynolds Averaged Navier-Stokes Models . . . . .	25
1.1.3. Large-Eddy Simulation . . . . .	29
1.1.4. Hybrid Methods . . . . .	33
1.2. Terminology . . . . .	35
1.3. Validation Geometry . . . . .	37
CHAPTER 2. THE EQUATIONS OF MOTION FOR A TURBULENT FLUID . .	<b>39</b>
2.1. Exact Transport Equations . . . . .	39
2.2. Filtering . . . . .	43
2.2.1. The Implicit Filter . . . . .	43
2.2.2. Explicit Filtering . . . . .	47
2.2.3. Implicit LES and the Grid Filter . . . . .	50
2.3. Flow Simulation Methodology . . . . .	51
2.3.1. The Contribution Function . . . . .	52
2.3.2. RANS Model . . . . .	56
2.4. Compressible Equations . . . . .	56
2.4.1. Thermodynamic Equations . . . . .	57
2.4.2. The Favre Filter . . . . .	58
2.4.3. Compressible Filtered Navier-Stokes . . . . .	59
2.4.4. Resolved Scale Energy Equation . . . . .	60
2.4.5. Compressible FSM . . . . .	63
CHAPTER 3. NUMERICAL METHOD . . . . .	<b>66</b>
3.1. Virtual Fluid Dynamics . . . . .	67
3.1.1. Curvilinear Coordinate Transform . . . . .	69
3.1.2. Boundary Conditions . . . . .	72
3.2. CFL3D . . . . .	72

CONTENTS—*Continued*

3.3. Grid Generation . . . . .	74
<b>CHAPTER 4. ERROR ANALYSIS AND TURBULENCE MODEL VALIDATION .</b>	<b>79</b>
4.1. Numerical Errors . . . . .	80
4.1.1. Grid Convergence for Large-Eddy Simulation . . . . .	80
4.1.2. Model of the Error . . . . .	82
4.1.3. Convergence of Chaotic Systems . . . . .	85
4.2. Averaging Errors . . . . .	90
4.3. A Posteriori Analysis . . . . .	91
4.3.1. Mean Flow . . . . .	92
4.3.2. Phase Averages . . . . .	93
4.3.3. A Note on Ensemble Averages . . . . .	95
<b>CHAPTER 5. RESULTS I: LAMINAR SIMULATIONS . . . . .</b>	<b>97</b>
5.1. Baseline Case . . . . .	98
5.2. Periodic Forcing . . . . .	100
5.2.1. Effect of Amplitude . . . . .	100
5.2.2. Effect of Frequency . . . . .	103
5.3. Suction . . . . .	106
5.4. Summary . . . . .	109
<b>CHAPTER 6. RESULTS II: NASA WORKSHOP SIMULATIONS . . . . .</b>	<b>110</b>
6.1. Numerical Convergence . . . . .	113
6.1.1. Subiterations . . . . .	113
6.1.2. Time Step Refinement . . . . .	114
6.1.3. Grid Refinement . . . . .	116
6.2. Comparison to Experiments . . . . .	118
6.2.1. Baseline . . . . .	118
6.2.2. Steady Suction . . . . .	122
6.2.3. Oscillatory Blowing . . . . .	125
6.3. Model Performance . . . . .	130
6.3.1. Pressure Drag . . . . .	131
6.3.2. Surface Pressure Distribution . . . . .	132
6.3.3. Reynolds Stresses . . . . .	133
6.3.4. Phase Averaged Structures . . . . .	135
6.3.5. Spectra . . . . .	141
6.3.6. Instantaneous . . . . .	142
<b>CHAPTER 7. CONCLUSIONS . . . . .</b>	<b>144</b>

CONTENTS—*Continued*

APPENDIX A. THE GENERALIZED MOMENT EQUATIONS . . . . .	<b>147</b>
A.1. Properties of the Generalized Moments . . . . .	147
A.2. Generalized Moment Equations . . . . .	149
A.2.1. Generalized Subfilter Stress Equations . . . . .	149
A.2.2. Generalized Subgrid Dissipation Rate Equations . . . . .	150
A.2.3. Generalized $k - \varepsilon$ Equations . . . . .	152
APPENDIX B. BOUNDARY LAYER SOLVERS . . . . .	<b>154</b>
B.1. Compressible Laminar Boundary Layer . . . . .	154
B.2. Turbulent Boundary Layer . . . . .	156
REFERENCES . . . . .	<b>159</b>



## LIST OF FIGURES

FIGURE 1.1.	The NASA CFDVal 2004 Workshop “hump” experiment. . . . .	21
FIGURE 1.2.	Profiles of the experimental geometries . . . . .	38
FIGURE 2.1.	Schematic of the turbulent spectrum. . . . .	55
FIGURE 3.1.	Computational domain . . . . .	66
FIGURE 3.2.	Parallel speedup . . . . .	69
FIGURE 3.3.	Schematic of the grid mapping . . . . .	76
FIGURE 3.4.	Computational grid . . . . .	78
FIGURE 4.1.	Error model . . . . .	84
FIGURE 4.2.	100 iteration of $x$ for the Hénon map . . . . .	86
FIGURE 4.3.	The Hénon attractor . . . . .	87
FIGURE 5.1.	Veclocity vectors and vorticity contours for the unforced flow . . . . .	98
FIGURE 5.2.	Reattachment location as a function of forcing amplitude . . . . .	101
FIGURE 5.3.	Effect of forcing on the downstream distribution of $C_p$ . . . . .	102
FIGURE 5.4.	Downstream evolution of the Fourier amplitude . . . . .	103
FIGURE 5.5.	Downstream evolution of the phase . . . . .	104
FIGURE 5.6.	Effect of forcing frequency on reattachment location . . . . .	105
FIGURE 5.7.	Effect of forcing frequency on $C_p$ . . . . .	106
FIGURE 5.8.	Downstream evolution of the frequency response . . . . .	107
FIGURE 5.9.	Time evolution of the wall vorticity for $f = 1.6F_0$ . . . . .	108
FIGURE 6.1.	Boundary layer profile at $x/c = -2.14$ . . . . .	112
FIGURE 6.2.	Convergence history . . . . .	115
FIGURE 6.3.	Time convergence . . . . .	116
FIGURE 6.4.	Grid refinement . . . . .	117
FIGURE 6.5.	Pressure and skin-friction coefficents for the unforced flow . . . . .	119
FIGURE 6.6.	$u$ -velocity profies for the unforced flow . . . . .	120
FIGURE 6.7.	Pressure spectra for the unforced flow . . . . .	121
FIGURE 6.8.	Mass flow rate as a function of back pressure in the slot . . . . .	123
FIGURE 6.9.	Pressure and skin-friction coefficents for the flow with steady suction . . . . .	124
FIGURE 6.10.	$u$ -velocity profies for the flow with steady suction . . . . .	125
FIGURE 6.11.	Pressure spectra for the flow with steady suction . . . . .	126
FIGURE 6.12.	Pressure and skin-friction coefficents for the flow with oscillatory forcing . . . . .	127
FIGURE 6.13.	$u$ -velocity profies for the flow with oscillatory forcing . . . . .	128
FIGURE 6.14.	Phase averaged vorticity and velocity vectors near the slot . . . . .	129
FIGURE 6.15.	Pressure spectra for the flow with oscillatory forcing . . . . .	130

LIST OF FIGURES—*Continued*

FIGURE 6.16. Pressure drag as a function of filter width . . . . .	131
FIGURE 6.17. Pressure coefficient profiles for various filter widths . . . . .	132
FIGURE 6.18. $R_{xx}$ profiles . . . . .	134
FIGURE 6.19. $R_{yy}$ profiles . . . . .	135
FIGURE 6.20. $R_{zz}$ profiles . . . . .	136
FIGURE 6.21. $R_{xy}$ profiles . . . . .	137
FIGURE 6.22. Phase averaged vorticity . . . . .	138
FIGURE 6.23. Phase averaged pressure. . . . .	139
FIGURE 6.24. Reynolds stress terms for several filter widths . . . . .	140
FIGURE 6.25. Spectra for various values of $\beta$ . . . . .	142
FIGURE 6.26. Isosurfaces of $\lambda_2$ vortex identification criteria . . . . .	143

## LIST OF TABLES

TABLE 3.1.	Splitting algorithm. . . . .	68
TABLE B.1.	Parameters for the similarity solution for the laminar boundary layer. . . . .	155

# NOMENCLATURE

## Roman Letters

$a$	speed of sound
$A^+$	van Driest ramping constant
$b$	slot width
$C$	Chapman-Rubesin parameter, $\frac{\rho\mu}{\rho_e\mu_e}$
$c$	chord
$C_\mu$	eddy viscosity model coefficient
$\langle c_\mu \rangle$	oscillatory momentum coefficient, $\frac{2b}{c} \frac{\langle \rho U_{\text{jet}}^2 \rangle}{\rho_\infty U_\infty^2}$
$c_f$	skin-friction coefficient, $\tau_{\text{wall}} / \frac{1}{2} \rho_0 U_0^2$
$C_p$	constant pressure specific heat
$C_p$	pressure coefficient, $p / \frac{1}{2} \rho_0 U_0^2$
$C_s$	Smagorinsky constant
$C_v$	constant volume specific heat
$C_{\varepsilon 1}, C_{\varepsilon 2}$	turbulence model coefficients
$C_{D_p}$	coefficient of pressure drag
$C_{ij}$	cross stress
$D_p$	pressure drag
$f$	frequency
$F^+$	reduced frequency, $\frac{f}{U_0} \frac{c}{2}$
$f_{\varepsilon 2}$	wall damping function
$H$	stagnation enthalpy, $h + \frac{u^2}{2}$
$h$	enthalpy

NOMENCLATURE—*Continued*

$\ell$	mixing length
$\mathcal{L}$	integral length scale
$l_{\text{sep}}$	separation length
$L_{ij}$	Leonard stress
$p$	pressure
$q_i$	molecular heat flux
$R_{ij}$	Reynolds stress
$S_{ij}$	rate-of-strain tensor, $\frac{1}{2} \left( \frac{\partial u_i}{\partial x_j} + \frac{\partial u_j}{\partial x_i} \right)$
$T$	temperature
$t$	time
$U_{\text{jet}}$	jet exit velocity
$u_i, \mathbf{u}$	velocity
$x_i, \mathbf{x}$	position

**Greek Letters**

$\beta$	FSM contribution coefficient
$\Delta x, \Delta y, \Delta z$	grid spacing
$\Delta$	characteristic grid spacing
$\Delta$	characteristic grid scale
$\eta$	wall normal similarity variable
$\eta$	Kolmogorov length scale
$\kappa$	von Kamen constant, $\sim 0.4$
$\lambda$	thermal conductivity
$\lambda_2$	vortex idenification criteria

NOMENCLATURE—*Continued*

$\mu$	molecular viscosity
$\mu_T$	eddy viscosity
$\nu$	kinematic viscosity
$\nu_t$	eddy viscosity
$\omega$	vorticity
$\rho$	density
$\sigma_{ij}$	viscous stress tensor
$\xi$	downstream similarity variable

**Nondimensional Parameters**

Ma	Mach number, $\frac{U}{a}$
Pr	Prandtl number, $\frac{C_p \mu}{\lambda}$
Re	Reynolds number, $\frac{\rho U L}{\mu}$

**Superscripts**

'	fluctuating part
"	fluctuations of Favre filtered quantities
+	inner coordinates

**Subscripts**

$\infty$	free stream value
$e$	external flow quantity

**Operators**

$\hat{f}$	phase averaged $f$
$\langle f \rangle$	Reynolds averaged $f$
$\overline{f}$	filtered $f$
$\tilde{f}$	Favre filtered $f$

NOMENCLATURE—*Continued***Acronyms**

ASM	Algebraic Stress Model
CFL	Courant Fedrichs-Lewy
DES	Detached-Eddy Simulation
DNS	Direct Numerical Simulation
FNS	Filtered Navier-Stokes
FSM	Flow Simulation Methodology
ILES	implicit large-eddy simulation
LaRC	Langley Research Center
LES	Large Eddy Simulation
MPI	Message Passing Interface
PDE	partial differential equation
PIV	Particle Imaging Velocimetry
RANS	Reynolds Averaged Navier-Stokes
SA	Spalart-Almaras model
SFS	subfilter stress
URANS	Unsteady Reynolds Averaged Navier-Stokes
VLES	Very Large Eddy Simulation

## ABSTRACT

Historically turbulence modeling has been sharply divided into Reynolds averaged Navier-Stokes (RANS), in which all the turbulent scales of motion are modeled, and large-eddy simulation (LES), in which only a portion of the turbulent spectrum is modeled. In recent years there have been numerous attempts to couple these two approaches either by patching RANS and LES calculations together (zonal methods) or by blending the two sets of equations. In order to create a proper bridging model, that is, a single set of equations which captures both RANS and LES like behavior, it is necessary to place both RANS and LES in a more general framework.

The goal of the current work is threefold: to provide such a framework, to demonstrate how the Flow Simulation Methodology (FSM) fits into this framework, and to evaluate the strengths and weaknesses of the current version of the FSM. To do this, first a set of filtered Navier-Stokes (FNS) equations are introduced in terms of an arbitrary generalized filter. Additional exact equations are given for the second order moments and the generalized subfilter dissipation rate tensor. This is followed by a discussion of the role of implicit and explicit filters in turbulence modeling.

The FSM is then described with particular attention to its role as a bridging model. In order to evaluate the method a specific implementation of the FSM approach is proposed. Simulations are presented using this model for the case of a separating flow over a “hump” with and without flow control. Careful attention is paid to error estimation, and, in particular, how using flow statistics and time series affects the error analysis. Both mean flow and Reynolds stress profiles are presented, as well as the phase averaged turbulent structures and wall pressure spectra. Using the phase averaged data it is possible to examine how the FSM partitions the energy between the coherent resolved scale motions, the random resolved scale fluctuations, and the subfilter quantities.



The method proves to be qualitatively successful at reproducing large turbulent structures. However, like other hybrid methods, it has difficulty in the region where the model behavior transitions from RANS to LES. Consequently the phase averaged structures reproduce the experiments quite well, and the forcing does significantly reduce the length of the separated region. Nevertheless, the recirculation length is significantly too large for all the cases.

Overall the current results demonstrate the promise of bridging models in general and the FSM in particular. However, current bridging techniques are still in their infancy. There is still important progress to be made and it is hoped that this work points out the more important avenues for exploration.

## Chapter 1

# INTRODUCTION

The only thing new in the world is the history you  
don't know.

HARRY S. TRUMAN

Turbulence modeling is a strangely bifurcated field; on one side recent decades have brought an explosion of new turbulence models, yet at the same time the techniques used in engineering applications are often the same ones developed thirty years ago or more - with the basic modeling assumptions dating back to the early 1900s. For simple canonical flows (e. g., homogeneous isotropic turbulence or zero pressure gradient boundary layer) current modeling techniques are in excellent agreement with experiments, yet the scientists studying such flows report that the underlying physics still eludes us, while the engineer reports that these models are unsatisfactory for more practical applications. Although our computational resources grow exponentially (a typical current day desktop machine can beat the performance of the supercomputers of the 1970s), enabling awesome benchmark calculations (e.g., 4096<sup>3</sup> simulation of homogeneous isotropic turbulence, Uno et al., 2003), progress towards robust and reliable models for simulating flows in real world applications seems to inch forward.

One fundamental reason for this dichotomy is that low Reynolds number turbulence is more difficult to model than high Reynolds number turbulence. This is because turbulence modeling relies on the assumption of universality in the modeled scales. The universality of turbulence is only valid for scales which are much smaller than the large scale inhomogeneities introduced by the flow geometry and much larger than the scales at which molecular dissipation occurs. The assumption of universality is therefore only good at high Reynolds number where both of these limits can be achieved simultaneously. Low Reynolds number flows do not have a

universal range, and in this sense many engineering flows are low Reynolds number flows. Furthermore, even in high Reynolds number flows the local Reynolds number near the boundaries goes to zero, so in this critical region much of the modeling breaks down.

If our only goal was to observe turbulence the Navier-Stokes equations would be an adequate tool since they govern the behavior of all flows, laminar and turbulent. But solving the Navier-Stokes equations directly is not a satisfactory way of predicting turbulent flows just as kinetic theory is a poor way to study laminar fluid flow. Aside from the enormous practical objection of computational cost, which is considerable, detailed information on the motion of individual small eddies may obscure the large scale physical processes taking place. In other words, we may lose the forest for the trees. Turbulence modeling, that is the development of equations which describe the large scale development of the flow, allows focusing on just the physical mechanisms of interest, as well as giving a considerable savings in computational cost.

The development of turbulence models is divided into two distinct approaches, Reynolds averaged Navier-Stokes (RANS) and large-eddy simulation (LES). In the former all the turbulent scales of motion are modeled, whereas in the latter the model only replaces smaller scale motions, while the remaining large scales are resolved explicitly. RANS is consequently less computationally expensive. It also provides certain flow statistics directly, as opposed to LES which requires averaging over a long time or an ensemble of simulations. RANS, however, can not be used in situations where the time dependent behavior of the turbulent structures is important. Examples include fluid structure interaction problems (where, for example, the frequency of the unsteady flow may resonate with the structure) or active flow control. For these situations LES or DNS (direct numerical simulation) is required. However, the computational cost for even a relatively coarse LES of a significant portion of an engineering system is currently prohibitive.

In order to make simulations of such flows practical various methods have been

proposed for combining LES and RANS models in a single simulation. These are generally referred to as hybrid RANS-LES models. The simplest such approach is called a zonal method. In this approach regions of the flow are designated as either RANS or LES at the start of the computation, and two separate models are used, one in each region. Other hybrid formulations attempt to mix RANS and LES equations, either through a blending function or other more complex equations, with varying degrees of success.

The ideal hybrid model would actually eliminate the RANS/LES distinction, replacing both with a single model that is capable of doing the job of either one. Germano (1999) suggests the term “bridging model” for a model that bridges the gap between RANS and LES. The following definition is adopted here: *a bridging model is a turbulence model characterized by a user specified filter cutoff scale which models the turbulent motions smaller than that cutoff scale*. Conventional LES models fail to meet this definition in the coarse grid limit; when the cutoff length scale exceeds the integral scale the LES is miscalibrated in that the model contribution continues to increase.

This dissertation examines the Flow Simulation Methodology (FSM) originally proposed by Speziale (1996) which is arguably the first approach which satisfies the definition of a bridging model. In addition to this, development of the FSM was motivated by the desire to incorporate the benefits of state of the art closure techniques developed for RANS models into unsteady LES type simulations. In doing so the FSM also extends the promise of accurate unsteady simulations with much coarser grids (and consequently much lower computational costs) than conventional LES approaches.

The plan of this dissertation is as follows. The remainder of this chapter consists of a short history of turbulence modeling intended to give an historical motivation for the approach taken in the rest of the work. Chapter 2 first develops the exact equations for the filtered flow variables and for the subfilter scale quantities in a

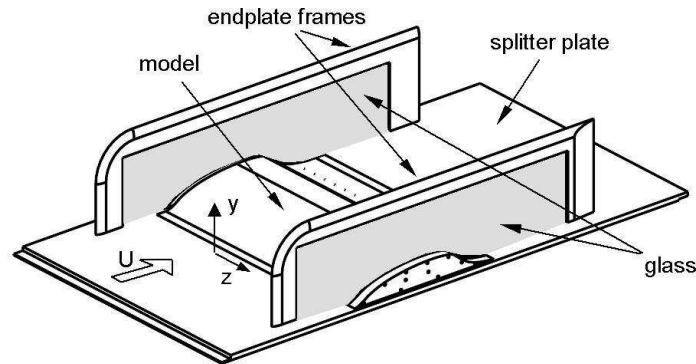


FIGURE 1.1. The NASA CFDVal 2004 Workshop “hump” experiment.

general form which is more consistent with a bridging model. This naturally leads into a discussion of the nature of the filter and filtering techniques in turbulence model. Finally the FSM closure equations are introduced.

The various numerical techniques used in solving the FSM equations are presented in chapter 3. Chapter 4 examines the issue of error analysis for turbulent flows, in particular the distinctions between numerical and modeling errors and the nature of numerical error analysis in the context of stochastic problems.

Chapters 5 and 6 present results for a separating flow with active flow control. The chosen geometry, the “hump” model from the NASA Langley Research Center Workshop: “CFD Validation of Synthetic Jets and Turbulent Separation Control,” is shown in figure 1.1. Chapter 5 contains preliminary laminar simulations which illustrate some of the basic physics of this flow. Turbulent results corresponding to the workshop case are presented in chapter 6. These results are used to validate the FSM model, and to investigate and evaluate the behavior of this new modeling approach.

Finally some brief conclusions are presented in chapter 7. Additional detail on some of the material can be found in the appendices.

## 1.1 A Brief History of Turbulence Modeling

As in most branches of science, the literature of turbulence modeling has long since outstripped the ability of even the most dedicated researcher to absorb all of the ideas that have been proposed in the last decades. Still, even a brief perusal of the key publications will quickly convince the reader that many supposedly new ideas are actually old ideas long neglected, that many often cited papers are apparently not often read, and that many key concepts are routinely and quietly misunderstood. As a consequence, the perspective motivating the body of this work is to demonstrate how a proper application of many classical ideas in turbulence modeling naturally leads to a formulation which is better suited for the development of the latest hybrid model concepts.

The object of this review is not merely to acknowledge credit due, although this would be sufficient justification, but to justify and motivate the approach taken to the development of the principle equations in chapter 2. Hopefully this brief history will elucidate how a framework for developing a bridging model for turbulence is the natural consequence of many early ideas in turbulence modeling.

### 1.1.1 Early History

Descriptions of turbulence predate modern science, the most famous being those of Leonardo da Vinci, but attempts to model turbulence, that is, to formulate mathematical equations governing turbulent flows, dates to the work of Osborne Reynolds. In Reynolds (1883), the first of his two classic papers on turbulent flow, he noted that flow in pipes could be either laminar or turbulent (what he termed “direct” and “sinuous” respectively) depending on a certain dimensionless parameter, now known as the Reynolds number. He further noted that for the laminar case the flow behaved as predicted by a steady solution of the Navier-Stokes equations. For the turbulent case, however, the flow no longer behaved according to the steady solution, presumably due

to the physical effects of the turbulent motions.

Building on these observations Reynolds second paper (1895) gives an equation for what he termed the “mean-mean-motion.” Motivated by the kinetic theory of gases (Maxwell, 1867), which related the Navier-Stokes equations to the dynamics of the “mean-motion” of large numbers of particles, Reynolds proposed decomposing turbulent flow into “mean-mean-motion” and “relative-mean-motion” by averaging the velocity at each point over a small volume. Denoting this average by a bracket,  $\langle \cdot \rangle$ , the velocity is decomposed as

$$f = \langle f \rangle + f', \quad (1.1)$$

where  $f'$  is the fluctuations relative to the average.

Applying this average to the Navier-Stokes equations yields a new set of equations for the averaged velocities,

$$\frac{\partial \langle u_i \rangle}{\partial t} + \langle u_j \rangle \frac{\partial \langle u_i \rangle}{\partial x_j} = -\frac{\partial \langle p \rangle}{\partial x_i} - \frac{\partial}{\partial x_i} [\langle \sigma_{ij} \rangle + \langle u'_i u'_j \rangle]. \quad (1.2)$$

These equations are formally identical to the original equations except that they contain a new term of the form  $\langle u'_i u'_j \rangle$ . This term, which plays the same role in the equations as a stress, is known as the Reynolds stress. In obtaining these equations Reynolds assumed that  $\langle u_i u_j \rangle = \langle u_i \rangle \langle u_j \rangle + \langle u'_i u'_j \rangle$ , or, more generally,  $\langle \langle f \rangle g' \rangle = 0$ . This property is not actually correct for spatial averages, a fact that Reynolds himself noted. The term Reynolds average is commonly used to refer to any average with the properties

$$\begin{aligned} \langle \langle f \rangle g \rangle &= \langle f \rangle \langle g \rangle \\ \langle f' \rangle &= 0. \end{aligned} \quad (1.3)$$

This definition will be adopted here, with the convention that angle brackets always denote a Reynolds average, in spite of the fact that this definition differs somewhat with the postulates in Reynolds original paper.

Reynolds did not propose a model for the unknown velocity correlation terms, merely noting that a solution for the fluctuating quantities  $u'_i$  is “practically impos-

sible.” It was Taylor (1915) who made the first step toward closing the equations by proposing a simple conceptual model for the turbulent heat flux. Taylor considered the heat transfer due to an eddy which is initially at the same temperature as its surroundings, and which then breaks away and travels a distance  $\ell$  before mixing with its new surroundings. If such eddies have a characteristic velocity  $v$ , the heat flux,  $q$ , due to such eddies is

$$q \sim v\ell \frac{\partial \langle \theta \rangle}{\partial y} \quad (1.4)$$

where  $\theta$  is the temperature. Noting the similarity between this estimate and the heat flux term in the conduction equation, Taylor dubbed the coefficient  $v\ell$  the “eddy-conductivity.” The length scale  $\ell$  is commonly called the mixing length, and this decomposition is known as the mixing length model. Although momentum is not a passive scalar, Taylor postulated that the same argument might apply for the mixing of momentum, in which case the coefficient

$$\nu_T \sim v\ell \quad (1.5)$$

is known as the “eddy-viscosity.”

It was Prandtl (1925) who introduced a practical model for the eddy-viscosity. Basing his ideas on the work of Boussinesq (1877), rather than Taylor, Prandtl proposed that the velocity scale used in the mixing length could be estimated dimensionally by

$$v \sim \ell \left| \frac{\partial \langle u \rangle}{\partial y} \right|. \quad (1.6)$$

The eddy-viscosity is then given by

$$\nu_T \sim \ell^2 \left| \frac{\partial \langle u \rangle}{\partial y} \right|. \quad (1.7)$$

(An alternate argument to arrive at this scaling without using the Taylor estimate (1.5) is to note that  $\langle u'_1 u'_2 \rangle \sim v^2$ . Using Prandtl’s estimate (1.6) we have  $\langle u'_1 u'_2 \rangle \sim \ell^2 |\partial \langle u \rangle / \partial y|^2$ , which would imply that  $\nu_T$  must scale like eq. 1.7). All that remains



to close the equation is a value for  $\ell$ . This may be estimated from geometric considerations, and similarity laws for several simple shear flows have been derived on this basis.

### 1.1.2 Reynolds Averaged Navier-Stokes Models

The mixing length model for turbulent diffusion does not specify a choice for the length and velocity scales but it is natural, perhaps, to associate these scales with the scales of the primary energy containing eddies, which are responsible for the bulk of the turbulent mixing. With this choice the resulting mean flow is expected to include no turbulent fluctuations, as they have been entirely filtered out, and their effect on the mean flow is entirely modeled by the Reynolds stress. Consequently it is common to replace Reynolds original local spatial average with a long time average,

$$\langle u \rangle(\mathbf{x}) = \lim_{T \rightarrow \infty} \frac{1}{T} \int_{t_0}^{t_0+T} u(\mathbf{x}, t) dt, \quad (1.8a)$$

a homogeneous spatial average over  $n$  dimensions,

$$\langle u \rangle(\mathbf{y}, t) = \lim_{V \rightarrow \infty} \frac{1}{V} \int_V u(\mathbf{x}, t) d^n \mathbf{x} \quad (1.8b)$$

or an ensemble average

$$\langle u \rangle(\mathbf{x}, t) = \lim_{N \rightarrow \infty} \frac{1}{N} \sum_{i=1}^N u^{(i)}(\mathbf{x}, t), \quad (1.8c)$$

where  $u^{(i)}$  are individual realizations of the flow. All of these averages satisfy the Reynolds averaging properties, (1.3), and models of this type are therefore called Reynolds averaged Navier-Stokes (RANS) models. Section 2.2 includes a more detailed discussion of the significance of the various averages, but regardless of the definition of the average the fundamental characteristic of the RANS approach is the assumption that all important turbulent scales are modeled.

This assumption generally implies that the modeled turbulence is completely specified by one set of scales. This is a powerful assumption as it enables making dimensional arguments for the various model quantities. These types of arguments have been used to obtain scaling laws and similarity solutions for a number of basic flows. However, it was the advent of the computer as a tool for scientific research that enabled the validation and further development of progressively more complex turbulence models as well as their application to more complex flows. As a result a profusion of new turbulence models has appeared over the last forty years.

The simplest models are algebraic or zero-equation models, in which the length scale is specified algebraically. These models are essentially equivalent to the Prandtl (1925) model near the wall (1.7), except that numerical solutions can be obtained using algebraically more complex estimates for the length scale  $\ell$ . The most popular of these models are probably the Baldwin-Lomax and the Cebicci-Smith models, both of which use the distance from the wall for the length scale in the inner part of the boundary layer:

$$\nu_T = \ell^2 |\omega|, \quad (1.9)$$

where  $\omega$  is the vorticity and the mixing length  $\ell$  is the wall distance modified by the ramping function of van Driest (1956),

$$\ell = \kappa y \left(1 - e^{-y^+/A^+}\right).$$

Here  $\kappa$  is the von Kármán constant,  $y^+$  is the wall distance scaled in inner coordinates, and  $A^+$  is a constant. In the outer part of the layer the eddy-viscosity is formulated using the Taylor mixing length hypothesis, with  $v$  and  $\ell$  specified using boundary layer scales.

The second World War and the subsequent cold war meant that communications between the major centers of turbulence research in Germany, Russia, and the West was often minimal. As a result much important work was duplicated independently

by multiple researchers. The technical literature is therefore often unclear as to the precise genealogy of certain critical advances. What is clear is that by the early 1940s it was realized that a better estimate of the turbulent scales could be obtained by solving additional transport equations.

Reynolds 1895 paper already included an exact equation for  $k = \frac{1}{2} \langle u'_i u'_i \rangle$ . Prandtl (1945) proposed solving a modeled form of this equation to obtain an estimate for  $v$ . The terms which must be modeled in order to close this equation are the turbulent diffusion of  $k$  and the turbulent dissipation rate. The turbulent diffusion of  $k$  can reasonably be modeled using the same eddy-viscosity coefficient as used for the diffusion of momentum, and the dissipation can be estimated dimensionally as

$$\varepsilon \sim \frac{v^3}{\ell}. \quad (1.10)$$

The exact production term includes the Reynolds stress, which has already been modeled to obtain a closure for the momentum equation. Setting  $v \sim k^{1/2}$ , and again estimating  $\ell$  based on an algebraic formulation, Prandtl proposed a one-equation turbulence model. This model, however, is not *complete*, since it still requires  $\ell$  to be specified.

Simultaneous with the work Prandtl, Kolmogorov proposed a two-equation model for  $k$  and  $\omega$ , where  $\omega$  is a characteristic inverse time scale of the flow. Kolmogorov's  $k$  equation is identical to Prandtl's, except that the dissipation estimate is now based on  $\omega$ :

$$\varepsilon \sim k\omega. \quad (1.11)$$

The  $\omega$  equation is a transport equation derived purely on heuristic grounds. Despite the fact that the precise physical meaning of  $\omega$  is not entirely clear,  $k - \omega$  models have been used very successfully.

Many researchers have preferred to choose a physically well defined quantity for the second turbulent scale. A natural choice is  $\varepsilon$ , which would also allow replacing the dimensional estimate (1.10) in the  $k$  equation. It is possible to derive an exact

transport equation for  $\varepsilon$ , but it contains a very large number of new terms which must be modeled. Early attempts to model this equations include the work of Harlow and Nakayama (1968). The Jones and Launder (1972) formulation is the most common  $k - \varepsilon$  model. In the  $k - \varepsilon$  model the exact  $\varepsilon$  equation is replaced with a model equation which is largely justified on dimensional grounds, although Speziale and Gatski (1997) derive a somewhat modified form based on more formal mathematical arguments. The dimensional estimate (1.10) is now used to compute the turbulent length scale.

Other two-equation models have been developed; one of the more common choices is to solve for the turbulent length scale directly ( $k - \ell$  models). The  $k - \ell$  approach relies on an ad-hoc transport equation to obtain the turbulent length scale. (A more rigorous  $\ell$  equation was proposed by Lumley et al., 1999, the derivation of which relies on a somewhat different definition of  $\ell$ .)

Just as Reynolds introduced exact equations for the mean momentum, Rotta (1951),<sup>1</sup> reasoned one could derive exact transport equations for the Reynolds stresses, rather than modeling them algebraically. An additional equation is also needed in order to obtain a length scale estimate. Of course, these new transport equations include new unknown terms which must be modeled. Reynolds stress models are not often used because of the high computational cost involved in solving seven additional transport equations.

Another attempt at moving away from the mixing length hypothesis is the constituent relation approach of Lumley (1970). He suggested using the tools developed in continuum mechanics for deriving a constituent relation for a substance with complex properties, such as the stress-strain relation for a non-Newtonian fluid, to replace the linear eddy-viscosity relationship with a more general non-linear function. This approach principally provides guidance on the functional dependencies and tensor form for the Reynolds stress, with coefficient functions which still must be determined

---

<sup>1</sup>Available in English as a NASA Technical Translation, Rotta (1972).

by physical investigations. However it does provide a rational basis for determining which tensor products should be used to go from a linear eddy-viscosity model to a non-linear expression.

Combining the Reynolds stress approach with the constituent relation technique Pope (1975), and later Gatski and Speziale (1993), proposed using the exact Reynolds stress equations to extract a constituent relation based not just on continuum properties, but on the actual structure of the fluid equations. By making an equilibrium, or near equilibrium, assumption the time derivative term in the Reynolds stress anisotropy equations can be eliminated. The result is a set of algebraic equations for the Reynolds stresses in terms of the turbulence quantities and the tensor invariants of the velocity gradient tensor which can be solved without integration. Two transport equations are still necessary to set the turbulent length and velocity scales. Algebraic stress models (ASM) have proved to be very successful at simulating many effects that are not well captured by conventional two-equation models.

It should be noted that several one-equation models have been proposed for quantities other than  $k$ . The most popular of this type is the Spalart-Almaras (SA) model (Spalart and Allmaras, 1994), which solves for a quantity which is essentially an eddy-viscosity. It is important to recognize that models like the SA model are not based on exact transport equations, rather they are postulated in an ad-hoc manner, unlike the  $k$  equation. There is also some disagreement as to whether the SA model should be considered complete since it requires wall-distance based ramping functions, but does not explicitly invoke  $\ell$  as a turbulent scale (Pope, 2000).

### 1.1.3 Large-Eddy Simulation

There are many problems for which it is necessary to obtain information about the temporal evolution of some of the unsteady turbulent structures, either because the modeling is not capable of accurately reproducing their net effect on the flow, or

because their time history is an important part of the information needed by the researcher. Of course a DNS could be used, but for many flows DNS is not computationally feasible. Astrophysical and meteorological flows are particularly difficult in this regard. The gap between the scales of interest to climatologists and the smallest scales present in the planetary boundary layer is so extreme that an attempt to resolve the entire flow is clearly impossible. Smagorinsky (1963) proposed modeling all the turbulent motions within a grid cell using a mixing length model; however, instead of using a turbulence length scale to estimate the mixing length, as done in RANS, he used the grid cell size,  $\Delta$ . This approach is called large eddy simulation (LES) since it models only the small eddies and the large eddies are explicitly resolved.

Smagorinsky's original formulation was specific to the planetary boundary layer; in its more general form the Smagorinsky model is

$$\nu_T = (C_s \Delta)^2 |\overline{\mathbf{S}}|, \quad (1.12)$$

where  $C_s$  is a (hopefully) universal constant, called the Smagorinsky constant, and  $\mathbf{S}$  is the rate-of-strain tensor. The overbar represents a filter operator with a width corresponding to the LES mixing length. The Smagorinsky formulation is based on the observation that the Taylor mixing length hypothesis applies to mixing by any well defined scale of eddies. Prandtl's mixing length model for the velocity scale is essentially a dimensional argument, and therefore cannot formally be applied in this case where there are now multiple length scales. However Lilly (1967) demonstrated that the scaling of the Smagorinsky model is consistent with the classical Kolmogorov -5/3 inertial scaling. Comparing (1.9) and (1.12) to Prandtl's estimate (1.7) reinforces the underlying similarity between RANS and LES formulations.

Lilly (1967) mathematically formalized the LES formulation by applying a *spatial mesh cube average* to the Navier-Stokes equations, and Leonard (1974) further generalized it to filters of the form:

$$\overline{f}(\mathbf{x}, t) = \int_{-\infty}^{\infty} G(x_i - \xi'_i) f(\xi'_i) d\xi'_i. \quad (1.13)$$

The resulting equations are formally identical to the RANS equations except that the turbulent stress tensor is now

$$\tau_{ij} = \overline{u_i u_j} - \overline{u_i} \overline{u_j}. \quad (1.14)$$

In addition to this first order theory, Lilly proposed a second order theory in which he derived transport equations for  $\tau_{ij}$  and for the subgrid energy,  $k = \frac{1}{2}\tau_{ii}$ . These equations contain unknown third-order moment terms which must be modeled. This is the LES equivalent of the Rotta (1951) approach, except that in LES there is no need for an additional equation to set the length scale.

Deardorff (1970) applied the first order theory of Lilly to plane Poiseuille flow at high Reynolds number. This result confirmed the usefulness of the LES approach, although the magnitude of the velocity profile was significantly overpredicted. Furthermore, Deardorff's simulations suggested that the theoretical value of the Smagorinsky coefficient suggested by Lilly was too high. Noting certain physical processes that are not adequately captured by the standard Smagorinsky model, Deardorff (1973) tested a variant of the second order theory of Lilly, in which transport equations were solved for the turbulent stress tensor, as well as for the moments associated with the dispersion of a passive scalar ( $\overline{u_i \theta}$ ).

Subsequent researchers have also tried one or more LES equation closures. For LES, since one scale is defined by the filter width, a one-equation model can be considered complete. Perhaps for this reason, several variants of the one-equation model have been proposed (Schumann, 1975; Yoshizawa, 1982); in general these models solve a transport equation for  $k$  and estimate the eddy-viscosity as

$$\nu_T = Ck^{1/2}\Delta,$$

similar to the Prandtl estimate for RANS. Schmidt and Schumann (1989) proposed a one-equation closure with a nonlinear eddy viscosity; the model is very similar to an ASM.

Several other approaches, all algebraic in nature should be noted. Germano (1992) proposed the dynamic subgrid stress (DSGS) model. In DSGS the filtered variables are explicitly refiltered, and by assuming a sort of similarity across the various filter scales an expression can be derived for the Smagorinsky constant. This allows the constant to be dynamically computed, which produces somewhat better results than the conventional Smagorinsky model. The procedure does not, however, introduce any meaningful new physics into the model and suffers from many of the disadvantages of the Smagorinsky model. Also, the dynamic procedure is not numerically robust and requires clipping and smoothing of the constant in order to remain stable, and is only formally correct in flows in which  $C_S$  is a constant over the region of support of the test filter kernel.

The scale similarity model (Bardina et al., 1980) models the stress tensor as

$$\tau_{ij} = \overline{\overline{u_i u_j}} - \overline{u_i} \overline{u_j}.$$

This approach has the advantage of not enforcing an alignment of turbulent stress and mean strain, but generally underpredicts the turbulent stress. The scale similarity model has proved somewhat more successful when added to other models (so called “mixed models”).

It has also been suggested that an LES formulation can be derived in which the filter consists of a projection onto a set (finite or infinite) of basis functions. In this case the LES equations can be represented as a nonlinear set of ordinary differential equations for the evolution of those basis functions. Pope (2001) proposed using a Galerkin projection which has the advantage that the basis functions can be exactly represented by the numerical method. Others have suggested using proper orthogonal decomposition (POD) modes with the expectation that these modes would best represent the turbulent eddies. To date such approaches have yielded little success.

In spite of the development of more advanced models, the bulk of LES research



continues to rely on algebraic closures, typically variants of the Smagorinsky model. This is in stark contrast to the world of RANS modeling, in which two-equation models are extremely common. No clear reason for this discrepancy exists; perhaps it is felt that for well resolved LES, where the unresolved scales are relatively isotropic, the significant computational costs of higher-order closures are not justified by the marginal improvements in results.

#### 1.1.4 Hybrid Methods

For flows in complex geometries it is often the case that even the most advanced RANS models are not able to predict the flow. RANS is also insufficient for problems in which details of the flow structures are important. For example, in fluid structure interaction problems the frequency of the large coherent motions of the flow must be known in order to check for resonances of the mechanical structure. Yet the prohibitive cost of LES for large problems often makes it an impractical alternative. Hybrid models are an attempt to combine RANS and LES in some fashion to allow for the best of both techniques to be used on the same problem.

The most straightforward hybrid approach is a zonal model, in which two calculations are patched together, one RANS and one LES. This may include feedback from the LES to the RANS, or may simply use RANS to generate boundary conditions for the LES. An example of an approach of this type is Felten and Lund (2005). Although conceptually simple, zonal models are quite complex to implement, because of the information mismatch at the boundary; the RANS data represents the mean flow, and the LES includes large scale fluctuations. Zonal models have also received much attention as a method of wall modeling (Piomelli et al., 2002; Tucker and Davidson, 2004); in this approach a RANS in the near wall region is patched to an LES in the outer region of the flow.

The first hybrid approach that can really be considered a bridging model is the

Flow Simulation Methodology (Speziale, 1996). As the FSM is the primary focus of this work, it will not be described in detail here. The underlying concept is to use a conventional RANS model to obtain a Reynolds stress tensor, and then use a separate scaling function, called the contribution function, to rescale the stresses to values appropriate to the local filter scale. The limited numerical scales (LNS) method of Batten et al. (2000) is another hybrid approach which is loosely based on Speziale’s proposal.

Other hybrid techniques have been proposed; the most popular is probably the detached eddy-simulation (DES) introduced by Spalart et al. (1997). In its original formulation it is a modification of the SA model, in which the wall distance length scale is replaced by a grid width parameter in the outer flow. Thus it recovers a RANS model near the wall, but there is no formal justification for the equations used in the LES region.

Strelets (2001) attempted to generalize the DES approach to the  $k - \omega$  model. The SA-DES relies on a modification of the destruction term in the eddy-viscosity transport equation. In extending this to the  $k - \omega$  equations, Strelets modified only the destruction term in the  $k$  equation; other terms in which length scale estimates appear are not modified. In particular, the eddy viscosity is still formed using the RANS length scale estimate of  $k^{1/2}/\omega$ . This estimate has no validity in the LES region. In fact, the length scale estimates used in the various terms of the equations proposed by Strelets are completely inconsistent.

Travin et al. (1999) claim to place DES on a more rigorous footing. To this end they formally define DES as “a three-dimensional unsteady numerical solution using a single turbulence model, which functions as a sub-grid-scale model in regions where the grid density is fine enough for a large-eddy simulation, and as a Reynolds-averaged model in regions where it is not.” This definition is absurdly broad as it includes most hybrid approaches; at the same time it fails to include any mathematical statement of how a DES is formulated.

## 1.2 Terminology

Due to the multiplicity of approaches to turbulence modeling, there is some disagreement in the literature as to the definitions of the various categories of models. In order to avoid contributing further to this confusion the definitions employed in the present work are clarified here.

The distinction between RANS and LES is usually drawn in terms of which average is applied. However, as will be discussed in section 2.2, the average is generally a consequence of the model rather than the reverse. Consequently the term RANS is reserved for models in which the effect of all turbulent scales of motion are included in the model. Approaches in which some scales are modeled and others are resolved will be termed LES.

In order to distinguish between different types of LES simulations, some authors have introduced the term VLES (very large-eddy simulation). This term is somewhat inconsistently used in the literature. Pope (2000) suggests that the term VLES should be reserved for models which capture at least 20% of the turbulent energy. If we assume a classical Kolmogorov scaling for the decay of the energy in spectral space, this is equivalent to resolving approximately one decade below the cutoff wavenumber, which is probably close to the coarsest we can go without significantly distorting the large scale turbulent structures. It is not always clear how much energy is actually being modeled in a given calculation, and the line between LES and VLES is not a sharp one, but modeling at least 20% of the energy seems like a reasonable rough minimum for VLES.

A term which is much misused in the literature is unsteady RANS or URANS. In a URANS simulation a RANS model is used with the unsteady terms retained in the transport equations. URANS models are often incorrectly used as VLES: by definition the RANS model already accounts for all the turbulent structures and is therefore too dissipative to predict the evolution of even the largest turbulent

structures. By way of example, consider the flow over a deflecting flap. If the rate of flap deflection is very slow, the flow is quasi-steady, and a URANS will produce no additional insight as compared to a series of steady RANS calculations, one for each of a series of intermediate flap deflection angles. Conversely, if the flap deflection happens quickly, it will produce a large vortical structure which will interact with the turbulence in a manner inconsistent with the RANS assumption that all turbulent scales are modeled. Cases where URANS is useful are limited to flows in which there is a large scale turbulent diffusion or transport on a scale much slower than the turbulence. For example, the dispersion of a passive contaminant where the net effect of turbulent mixing is important in the time evolution, but the local details of even the largest structures may not be of interest. URANS is also applicable to the decay of homogeneous isotropic turbulence since there is a temporal variation even with all of the spatial scales filtered out. In fact, many RANS models are calibrated by matching the theoretically predicted rate of energy decay for decaying homogeneous isotropic turbulence. Unfortunately URANS is generally not used for these type of problems but is instead applied to flows where it has no chance of correctly predicting the scales of interest.

Just as RANS and LES do not refer to specific models, but to a general modeling approach or class of models, the FSM also is a modeling approach, rather than a specific model. As will be further detailed in section 2.3, the FSM uses an underlying RANS closure and a contribution function to obtain the subfilter stresses. Although certain RANS models may be better suited to the FSM approach, in principle FSM can be formulated using any RANS model. Furthermore, a wide variety of contribution functions have been suggested. For testing purposes a particular model has been adopted in the current work, but this represent just one possible implementation of the FSM philosophy.

### 1.3 Validation Geometry

Evaluating advanced turbulence models for use in real world applications requires an extremely well documented set of experiments. The experimental geometry has to be sufficiently complex to be representative of relevant engineering applications. Yet it also has to be simple enough that the computational costs of performing all the necessary parameter studies remain practical. Fortunately a series of experiments performed at NASA Langley Research Center (LaRC), first by Seifert and Pack (2000b), and continued by Greenblatt et al. (2004, 2005), fills these requirements perfectly.

The original experiments were performed using a NACA 0015 airfoil to which periodic excitation was introduced at 10% chord. The airfoil was pitched up and active flow control was used to keep the flow attached or minimize the effects of separation. Further experiments revisited the flow control research of Glauert (1945) and Glauert et al. (1948). These experiments used very thick airfoils with a relatively sharp corner at about 60% chord, followed by a pressure recovery ramp. As a result the flow would separate at zero angle of attack. The intention was to use steady suction to reattach the flow and thereby improve the pressure recovery on the rear of the airfoil. Drawing on this earlier work, Seifert and Pack (1999) proposed a similar airfoil. Retaining just the upper surface, which was mounted directly to the wall of the wind tunnel, they created a generic “hump” that would separate at the sharp corner if no control was applied. This “hump” geometry was designed specifically to facilitate comparison with CFD. The advantage to this setup is that circulation effects are removed from the problem. Additionally, the grid generation is much simplified. Using this geometry Pack and Seifert (2000) investigated the effects of steady forcing (blowing or suction) as well as periodic zero-mass flux excitation. The experiments were performed in the transonic 0.3-meter cryogenic wind tunnel at NASA Langley Research Center so that the effects of compressibility could also be studied (Seifert and Pack, 2000a).

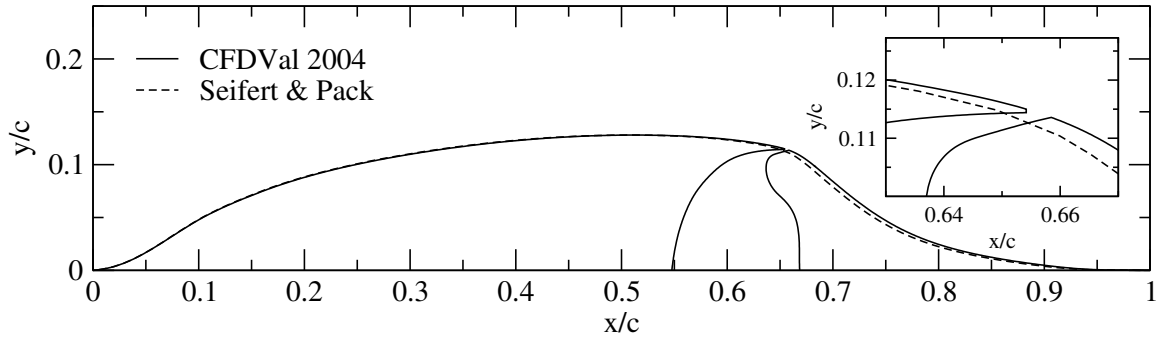


FIGURE 1.2. Profiles of the geometries used in the experiments of Seifert and Pack (1999) and in the CFDVal 2004 Workshop, based on the QA data.

Interest in these experiments was sufficiently high that the geometry was adopted by NASA as one of the three test cases for the Langley Research Center Workshop: “CFD Validation of Synthetic Jets and Turbulent Separation Control.” Largely due to the difficulty of obtaining flow field data in the transonic wind tunnel a new experiment was built, using an almost identical profile scaled up by a factor of two. This made it possible to obtain flow field data using particle imaging velocimetry (PIV). Very detailed measurements have been made for these experiments (Greenblatt et al., 2004, 2005) and the data has been made available via the World Wide Web (<http://cfdval2004.larc.nasa.gov>). Additionally this case was included in the 11th ERCOFTAC/IAHR Workshop on Refined Turbulence Modelling.

Over the course of the numerical investigations presented here both the Seifert and Pack and the CFD Validation 2004 geometries were used. The earlier laminar simulations in chapter 5 were all performed using the original Seifert and Pack version of the “hump.” The FSM validation results presented in chapter 6 were performed using the later NASA Workshop “hump.” The two profiles are shown in figure 1.2; they are almost identical. A comparison of baseline results for the two experiments shows almost no difference in surface pressure distributions (Greenblatt et al., 2004).

## Chapter 2

# THE EQUATIONS OF MOTION FOR A TURBULENT FLUID

Yon foaming flood seems motionless as ice;  
Its dizzy turbulence eludes the eye,  
Frozen by distance.

W. WORDSWORTH, *Address to Kilchurn Castle*

We have seen that historically a sharp distinction is drawn in the derivation of RANS and LES closures. The equations that result are nonetheless formally identical. The hybrid approach, and especially zonal methods, although offering important functional improvements over conventional RANS and LES, continues very much in the traditional paradigm, treating RANS and LES as two irreconcilable procedures. Any attempt towards creating a truly integrated approach must, from the outset, make use of the formal similarity of the RANS and LES equations.

This chapter develops the governing equations for a fluid in turbulent motion in precisely such a light. After presenting the exact equations in the most general form the nature and requirements of the filter are discussed. Finally the Flow Simulation Methodology (FSM) is presented, along with the underlying RANS closure which it requires.

## 2.1 Exact Transport Equations

The governing equations for fluid flow, whether laminar or turbulent, are the Navier-Stokes equations:

$$\frac{\partial \rho}{\partial t} + \frac{\partial \rho u_i}{\partial x_i} = 0 \tag{2.1}$$

$$\frac{\partial \rho u_i}{\partial t} + \frac{\partial \rho u_i u_j}{\partial x_j} = -\frac{\partial p}{\partial x_i} + \frac{\partial \sigma_{ij}}{\partial x_j}, \tag{2.2}$$

where  $\rho$  is the density,  $p$  is the pressure,  $u_i$  is the velocity, and  $\sigma_{ij}$  is the viscous stress tensor. (Here, as throughout this work, the Einstein convention for repeated indices is employed.) For a Newtonian fluid we assume the deviatoric part of the viscous stress and the rate of strain tensors are proportional so

$$\sigma_{ij} = 2\mu \left( S_{ij} - \frac{1}{3} S_{kk} \delta_{ij} \right) \quad (2.3)$$

where  $\mu$  is the molecular viscosity and

$$S_{ij} = \frac{1}{2} \left( \frac{\partial u_i}{\partial x_j} + \frac{\partial u_j}{\partial x_i} \right) \quad (2.4)$$

is the rate of strain tensor. If we assume the fluid is incompressible the Navier-Stokes equations reduce to

$$\frac{\partial u_i}{\partial x_i} = 0 \quad (2.5)$$

$$\frac{\partial u_i}{\partial t} + u_j \frac{\partial u_i}{\partial x_j} = -\frac{1}{\rho} \frac{\partial p}{\partial x_i} + \nu \nabla^2 u_i, \quad (2.6)$$

where  $\nu = \mu/\rho$  is the kinematic viscosity.

The velocity and pressure are now decomposed into large and small scale components by the introduction of a filter operator denoted by an overbar,

$$f = \overline{f} + f'. \quad (2.7)$$

(The following notation is adopted in the present work:  $\overline{f}$  represents a general filter, whereas  $\langle f \rangle$  represents a filter which satisfies the Reynolds averaging properties, 1.3.) In order to maintain the greatest generality the filter operator is not specified; it is simply assumed that it in some sense removes the turbulent motions that are not of interest and retains only those that need to be explicitly resolved. Also, it is required that the filter operator be linear and commute with differentiation. Armed with just these two properties, the filter can be applied to the incompressible continuity equation (2.5), to obtain

$$\frac{\partial \overline{u_i}}{\partial x_i} = 0. \quad (2.8)$$



Applying the filter to the momentum equation (2.6) gives

$$\frac{\partial \overline{u_i}}{\partial t} + \overline{u_j \frac{\partial u_i}{\partial x_j}} = -\frac{1}{\rho} \frac{\partial \overline{p}}{\partial x_i} + \nu \nabla^2 \overline{u_i}, \quad (2.9)$$

or,

$$\frac{\partial \overline{u_i}}{\partial t} + \overline{u_j} \frac{\partial \overline{u_i}}{\partial x_j} = -\frac{1}{\rho} \frac{\partial \overline{p}}{\partial x_i} + \nu \nabla^2 \overline{u_i} - \frac{\partial}{\partial x_j} [\tau(u_i, u_j)], \quad (2.10)$$

where

$$\tau(f, g) = \overline{fg} - \overline{f} \overline{g} \quad (2.11)$$

is the generalized moment operator of Germano (1992). (The generalized moment operator is further described in appendix A.1.) The moment  $\tau(u_i, u_j)$  is the subfilter stress (SFS) tensor and it represents the stress on the filtered field produced by the motions in the subfiltered scales. Here the term “subfilter” is used rather than the more common “subgrid” since at this stage the equations are still continuous partial differential equations and are therefore not dependent on a grid. This is a critical point: the filtering operation produces a new set of *differential* equations; although it may be practically useful at a later point to link the filter width to a grid spacing there is no intrinsic connection between the two.

These two equations, (2.8) and (2.10), are the filtered Navier-Stokes (FNS) equations. Formally they are identical to the traditional RANS or LES equations; their significance lies in the fact that in this form they are valid for any linear commuting filter. As written they are exact but not closed since the SFS is still unknown. We are looking for model equations which are closed, although not exact, and which will be obtained by replacing the SFS term with a model.

One approach would be to close (2.10) directly using an algebraic model. However, in order to derive higher order moment closures it is instructive to develop transport equations for turbulence quantities in this generalized notation. (Details of the derivation can be found in appendix A.2, only the primary results are given

here). We define the subfilter energy as

$$k = \frac{1}{2} \tau(u_i, u_i). \quad (2.12)$$

Introducing a Navier-Stokes operator defined such that (2.6) can be expressed as

$$\mathcal{N}[u_i] = 0, \quad (2.13)$$

then a set of evolution equations can be derived for the SFS by forming the moment equation

$$\tau(u_i, \mathcal{N}[u_j]) + \tau(u_j, \mathcal{N}[u_i]) = 0. \quad (2.14)$$

Taking one half the trace of this equation we obtain the evolution equation for the subfilter energy,

$$\frac{\partial k}{\partial t} + \overline{u_j} \frac{\partial k}{\partial x_j} = \mathcal{P} - \varepsilon + \mathcal{D} + \nu \nabla^2 k, \quad (2.15a)$$

where

$$\mathcal{D} = -\frac{1}{\rho} \frac{\partial}{\partial x_i} [\tau(u_i, p)] - \frac{1}{2} \frac{\partial \tau(u_i, u_i, u_k)}{\partial x_k} \quad (2.15b)$$

$$\mathcal{P} = -\frac{\partial \overline{u_i}}{\partial x_k} \tau(u_i, u_k) \quad (2.15c)$$

$$\varepsilon = \nu \tau \left( \frac{\partial u_i}{\partial x_k}, \frac{\partial u_i}{\partial x_k} \right) \quad (2.15d)$$

are the turbulent diffusion, production, and dissipation of subfilter energy, respectively. (The generalized third order moment  $\tau(f, g, h)$  is defined in appendix A.2.)

Similarly we can form the moment equation

$$2\nu \left[ \tau \left( \frac{\partial u_i}{\partial x_k}, \frac{\partial \mathcal{N}[u_j]}{\partial x_k} \right) + \tau \left( \frac{\partial u_j}{\partial x_k}, \frac{\partial \mathcal{N}[u_i]}{\partial x_k} \right) \right] = 0. \quad (2.16)$$

Again taking one half the trace we obtain the equation for the dissipation rate scalar,

$$\frac{\partial \varepsilon}{\partial t} + \overline{u_j} \frac{\partial \varepsilon}{\partial x_j} = \mathcal{P}^\varepsilon - \Phi^\varepsilon + \mathcal{D}^\varepsilon + \nu \nabla^2 \varepsilon, \quad (2.17a)$$

where

$$\mathcal{D}^\varepsilon = -\frac{\nu}{\rho} \left[ \frac{\partial}{\partial x_i} \left[ \tau \left( \frac{\partial u_i}{\partial x_k}, \frac{\partial p}{\partial x_k} \right) \right] \right] - \nu \frac{\partial}{\partial x_l} \left[ \tau \left( u_l, \frac{\partial u_i}{\partial x_k}, \frac{\partial u_i}{\partial x_k} \right) \right] \quad (2.17b)$$

$$\mathcal{P}^\varepsilon = -\frac{\partial \overline{u_i}}{\partial x_l} \varepsilon_{il} - 2\nu \frac{\partial \overline{u_l}}{\partial x_k} \tau \left( \frac{\partial u_i}{\partial x_k}, \frac{\partial u_i}{\partial x_l} \right) - 2\nu \frac{\partial^2 \overline{u_i}}{\partial x_l \partial x_k} \tau \left( \frac{\partial u_i}{\partial x_k}, u_l \right) \quad (2.17c)$$

$$-2\nu \tau \left( \frac{\partial u_i}{\partial x_k}, \frac{\partial u_l}{\partial x_k}, \frac{\partial u_i}{\partial x_l} \right) \quad (2.17d)$$

$$\Phi^\varepsilon = 2\nu^2 \tau \left( \frac{\partial^2 u_i}{\partial x_k \partial x_l}, \frac{\partial^2 u_i}{\partial x_k \partial x_l} \right), \quad (2.17e)$$

are the turbulent diffusion, production, and dissipation of the subfilter dissipation rate scalar.

## 2.2 Filtering

Contrary to the procedure generally adopted in the literature it is clear from the preceding section (and the supplemental details in appendix A.2) that the equations for the filtered flow variables can be derived without specifying a particular filter *a priori*. It is therefore logical to ask what the filter is and how is it imposed. This point is widely misunderstood, and has led many investigators to explicitly filter turbulence simulations, a procedure which, as we shall see, is not necessarily consistent with the equations.

### 2.2.1 The Implicit Filter

Pope (2000) argues that, for the Smagorinsky model, the filter is implicitly defined by the the form of the model. He terms this filter the *implicit Smagorinsky filter*. In fact his argument is generally applicable to most models. Because of the importance of this point it is expanded on here.

Consider as a simple model the one-dimensional wave equation,

$$\frac{\partial u}{\partial t} + c \frac{\partial u}{\partial x} = 0, \quad (2.18)$$

on the domain  $x \in \mathbb{R}$  and  $t > 0$ , along with the initial condition

$$u(x, 0) = f(x). \quad (2.19)$$

The solution is known to be

$$u(x, t) = f(x - ct). \quad (2.20)$$

We can apply our linear commuting filter to obtain the filtered wave equation

$$\frac{\partial \bar{u}}{\partial t} + c \frac{\partial \bar{u}}{\partial x} = 0. \quad (2.21)$$

An initial condition is now required for  $\bar{u}$ . If we put

$$\bar{u}(x, 0) = g(x) \quad (2.22)$$

then we can solve the filtered equation (2.21) analytically, treating  $\bar{u}$  as the dependent variable in the conventional manner, to get

$$\bar{u}(x, t) = g(x - ct). \quad (2.23)$$

If we set  $g = \bar{f}$ , then the value of  $\bar{u}$  is identical to the one which would be obtained by filtering the solution obtained from the unfiltered equation (2.18) directly. That is, comparing the solutions of equations (2.18) and (2.21), the filter observed in the latter case is entirely determined by the initial data.

Of course the Navier-Stokes equations are non-linear. To introduce non-linear effects into our model consider the inviscid Burgers equation,

$$\frac{\partial u}{\partial t} + u \frac{\partial u}{\partial x} = 0. \quad (2.24)$$

Applying the filter produces a model term of the same form as the one seen in the FNS equations:

$$\frac{\partial \bar{u}}{\partial t} + \bar{u} \frac{\partial \bar{u}}{\partial x} = \frac{1}{2} \frac{\partial}{\partial x} [\bar{u} \bar{u} - \overline{uu}]. \quad (2.25)$$

Consider a particular solution of the unfiltered equation (2.24) which we will denote  $u^*$ . We wish to solve (2.25) for the filtered solution corresponding to  $u^*$  for a certain filter. Writing the equation as

$$\frac{\partial \bar{u}}{\partial t} + \bar{u} \frac{\partial \bar{u}}{\partial x} = S(x, t), \quad (2.26)$$

we can, in principle, solve this equation for any value of the source term  $S(x, t)$ . In particular if we set the source term to

$$S(x, t) = \frac{1}{2} \frac{\partial}{\partial x} [\overline{u^* u^*} - \overline{u^* u^*}], \quad (2.27)$$

and appropriately filter the initial conditions, we will obtain a solution for the filtered field directly without applying any filter during the solution procedure. (Of course a filter is needed to obtain the source term, but this can be done independently of solving the equation.) Again, as in the case of the wave equation, the filter is entirely determined implicitly. If we evaluate  $S(x, t)$  using a different filter the solution to (2.26) will change to correspond to that filter. That is, the value of the source term (along with the initial condition) sets the filter.

As in the FNS equations we can replace the unclosed term  $S(x, t)$  with a model. (In fact the study of so-called “Burgers turbulence” has been used as model for real fluid turbulence, although the dynamics of the two turn out to be significantly different.) In that case it is not obvious that the solution to the filtered equation corresponds to a specific solution of the original unfiltered equation. But what is clear is that, insofar as there exists a well defined filter, the shape of that filter is entirely determined by the model, along with the initial condition, and no explicit filtering is necessary or warranted in the solution procedure.

The same argument carries over exactly to the Navier-Stokes and FNS equations. That is, the filter is defined implicitly by the form of the turbulence model. In principle the initial and boundary data should also affect the implicit filter. However, we assume that the universality of turbulence means that the effect of the boundary

conditions on the filter becomes unimportant within a very short distance from a boundary. The effect of a mismatch between the boundary data and the model can be observed by, for example, feeding a RANS inflow into an LES, or vice versa. For an open flow problem the initial condition can be assumed to have little effect after some initial flow through time. For a closed flow the initial condition could, in theory, change the implicit filter, however this is unlikely as the physics of the turbulence will generally act to quickly fill any available scales, while the dissipation of the model will tend to damp scales smaller than the filter width.

There are several important practical ramifications of this analysis. The first is that most of the discussion in the literature as to the optimal choice of a filter is irrelevant, since in general the researcher has little control over which specific filter is actually employed. By changing the model the shape of the implicit filter will be affected, but not in any generally predictable way. Also, this underscores the fundamental connection between RANS and LES in that any real difference between the two must proceed from the assumptions in the model rather than the filter used to derive the equations. In a RANS it is assumed that all turbulent scales are modeled whereas LES only models a certain range of scales. Furthermore, both RANS and LES can be formulated in terms of either space or time averages. For LES filtering the width of the filter is usually well defined, at least at the level of a dimensional estimate, but the shape is unknown. This significantly complicates *a posteriori* analysis in which DNS data is filtered and compared to LES data, since it is the unknown implicit LES filter which should be applied for such comparisons to be valid.

Another consideration is related to the Leonard stress term. It is common in LES to decompose the SFS tensor into three parts,

$$\begin{aligned}\tau(u_i, u_j) &= \overline{(\overline{u_i} + u'_i)(\overline{u_j} + u'_j)} - \overline{u_i} \overline{u_j} \\ &= \underbrace{\overline{\overline{u_i} \overline{u_j}} - \overline{u_i} \overline{u_j}}_{L_{ij}} + \underbrace{\overline{\overline{u_i} u'_j} + \overline{u'_i \overline{u_j}}}_{C_{ij}} + \underbrace{\overline{u'_i u'_j}}_{R_{ij}},\end{aligned}\tag{2.28}$$

the Leonard stress ( $L_{ij}$ ), the cross-stress ( $C_{ij}$ ) and the Reynolds stress ( $R_{ij}$ ). If the SFS model is taken as a model of the Reynolds stress (as it is by many authors) the Leonard and cross-stresses remain to be modeled. It has been suggested that the Leonard stress, which is only a function of the filtered velocities, can be calculated explicitly. This is not correct, or at best, only approximately true, since the filter that needs to be applied to maintain consistency is the unknown implicit filter. It should be noted that this is not a problem for the present approach since the model equations in sections 2.1 and A.2 are equations for the entire SFS tensor. Additionally, the Leonard and cross-stresses are not separately Galilean invariant; modeling the entire SFS tensor makes it much easier to assure that the SFS model remains Galilean invariance.

### 2.2.2 Explicit Filtering

From the foregoing analysis it would appear that explicit filtering is fundamentally unjustified. Given that it is very commonly applied, it is instructive to examine why it is used, what its effect is, and whether it is ever appropriate.

In part the origin may lie in a fundamental misunderstanding of the filtering operation. In contrast to the procedure followed in section 2.1 it is common to derive the LES equations by applying a specific filter to the Navier-Stokes equations. Following such a procedure it is natural that one might presume that a specific filter can be imposed and the only clear way to do that might appear to be to filter the solution at each time step. Of course, as has been shown above, this would be an incorrect interpretation; rather the specific filter must be taken as a constraint on the model (albeit one which may be practically impossible to impose).

The other reason for explicit filtering can be seen by examining the FNS momentum equation,

$$\frac{\partial \overline{u_i}}{\partial t} + \overline{u_j} \frac{\partial \overline{u_i}}{\partial x_j} = -\frac{1}{\rho} \frac{\partial \overline{p}}{\partial x_i} + \nu \nabla^2 \overline{u_i} - \frac{\partial}{\partial x_j} [\tau(u_i, u_j)].$$

Note that the purpose of the filter is to remove the “small scales” (in some sense). In integrating the FNS equation the time rate of change term, the pressure gradient term, and the viscous diffusion term are all linear, so they cannot generate new small scale motions. The only terms which generate small scales are the nonlinear advection term and the turbulence model. Theoretically, in order for the solution to remain “filtered” the “small scale” part of each of these terms should exactly cancel. This argument can be made precise for a filter which is a projection operator, in which case the filtered fields are restricted to a specific subspace. In practice the model is only meaningful for the large scales. This means that the non-linear behavior of the advection term and the model may combine to produce small scale noise which could contaminate or even destabilize the simulation. Of course the model term should primarily be diffusive, so we might expect that the small scale noise will tend to be damped.

In order to eliminate this small scale contamination the FNS momentum equation can be reformulated (Lund, 1997) as

$$\frac{\partial \overline{u_i}}{\partial t} + \overline{u_j \frac{\partial \widehat{u_i}}{\partial x_j}} = -\frac{1}{\rho} \frac{\partial \overline{p}}{\partial x_i} + \nu \nabla^2 \overline{u_i} - \frac{\partial}{\partial x_j} \left[ \overline{u_i u_j} - \widehat{\overline{u_i u_j}} \right], \quad (2.29)$$

where the hat represents a filter which is not the same as the original implicit filter. (Lund neglects the implicit nature of the filter and assumes the two filters are the same. Thus his proposal is not practically feasible because the implicit filter is actually unknown.) Now we are required to model a slightly different quantity, although this new model term should only differ from the old one in the “small scales” where the model is not accurate anyway.

In order to examine the effect of explicit filtering after each time step (which is how explicit filters are often applied) consider the following equation:

$$u_t = f(u). \quad (2.30)$$

We can semi-discretize in time using a forward-Euler method,



$$\frac{u^{n+1} - u^n}{\Delta t} = f(u^n), \quad (2.31)$$

or

$$u^{n+1} = u^n + \Delta t f(u^n) \quad (2.32)$$

$$= u^0 + \Delta t \sum_{i=1}^n f(u^i). \quad (2.33)$$

Applying a linear filter operator we have

$$\overline{u^{n+1}} = \overline{u^0} + \Delta t \sum_{i=0}^n \overline{f(u^i)} \quad (2.34)$$

which is the correct solution. If instead we apply an explicit filter at each timestep we have the following numerical procedure:

$$u^{n+1} = \overline{u^n + \Delta t f(u^n)} \quad (2.35)$$

$$= \overline{u^0}^{(n+1)} + \Delta t \sum_{i=0}^n \overline{f(u^i)}^{(i+1)} \quad (2.36)$$

where  $\overline{f}^{(n)}$  represents  $f$  filtered  $n$  times. If the filter is a projection operator,  $\overline{\overline{f}} = \overline{f}$ , then these two formulations are the same. Otherwise the effect is that the components of the solution which are older are repeatedly filtered over the course of the calculation.

Combining the above analysis with the modified FNS formulation in (2.29), one approach is to project the entire FNS equations into some subspace. The non-linear terms then can be formally decomposed and only the parts in the projected subspace retained. Since the linear terms are already in the projected subspace, it no longer matters whether the projection is applied to the individual non-linear terms or the whole solution after each time step. However, since the projection operator is different from the implicit model filter this procedure does change the model, since the original model was a function of the filtered velocities,  $\overline{u}_i$ , and it is now being computed in terms of the projected component,  $\widehat{u}_i$ .

### 2.2.3 Implicit LES and the Grid Filter

It is worthwhile to take note here of so-called implicit LES (ILES), in which the dissipation of the numerical scheme is used as a turbulence model. This is related to the identification by some authors of the effect of discretizing the model equations with a “grid filter.”

Due to the widespread confusion regarding the implicit nature of the filter discussed in the previous section, many authors attempted to explain the source of the “missing” filter operation as associated with the effect of restricting the flow variables to a finitely resolved discrete grid. Although analysis of this so-called “grid filter” continues today (e. g. Carati et al., 2001), it is simply incorrect. The filter that appears in the governing equations is the implicit filter defined by the model, and is therefore a property of the PDE, not the grid. The effect of discretizing the equations is the same as for any problem in numerical analysis; there is a great body of literature on how to analyze the discretization error (comprehensive treatments include Hirsch, 1988; Tannehill et al., 1997).

Pope (2003) suggests that practitioners of LES can be divided into two schools, one that treat the model in a continuum, and one that considers LES to be a numerical procedure (or perhaps, more accurately, a discrete model). There have, in fact, been a few attempts to construct proper discrete models for LES. One approach would be to use POD modes to reduce the LES equations to a smaller number of ODEs for the evolution of the POD modes. Another is to attempt to produce a closure model for Galerkin basis functions directly (Pope, 2001). However, aside from these relatively unsuccessful suggestions the remaining work in discrete LES is either “grid filter” analysis which is just a confusion of numerics and modeling, and ILES.

ILES grows out of the realization that under-resolved simulations of the exact Navier-Stokes equations are sometimes surprisingly successful at predicting turbulent flows. While this is not expected, it can perhaps be understood in the light of the

success in simulating low dimensional chaotic systems with finite accuracy discrete numerics. This will be discussed further in section 4.1.3. The primary difficulty with ILES methods is applying physical insight derived from continuum models directly to ILES methods. Partisans of ILES point to the similarity in the form of the numerical error and the leading order turbulence model terms. However, it is difficult to examine the behavior of these terms since ILES methods cannot be subjected to grid resolution studies directly. This is because traditional numerical analysis relies on grid convergence studies and the discrete equations for ILES methods converge not to a model equation, but rather to the Navier-Stokes equations.

There have been attempts to do more formal analysis of ILES methods. Margolin and Rider (2002) proposed discretizing and simulating the modified equation of an ILES method which would make it possible to do a proper grid refinement study of for ILES. Domaradzki et al. (2003) examined the spectral behavior of the numerical viscosity in an ILES scheme and compared it to the eddy-viscosity as predicted from DNS data in order to see to what extent the numerics mimics the physics.

It is true that, as will be shown in more detail in section 4.1.2, it must be expected that most LES will continue to run in an intermediate region where both model and numerical effects are significant. However, the conclusion of Pope (2003) that we must embrace both discrete and continuous LES formulations is unwarranted. Firstly, even for coarse grids, numerical analysis still provides tools for understanding the numerical error without resorting to conflation of numerics and modeling. Secondly, although numerical effects may be significant for conventional LES, they may be dramatically less so for VLES. And, as it is hoped that this work will demonstrate, bridging models provide a real promise for the future importance of VLES.

## 2.3 Flow Simulation Methodology

Speziale (1996) proposed the first bridging approach. His idea was to combine existing

RANS closures with a *contribution function* that would be used to scale the magnitude of the Reynolds stress term depending on the local state of the turbulence and the local grid resolution. The function is designed to scale the model contribution depending on how well the turbulence is resolved on the particular grid. The approach assures that the method recovers a correct RANS closure in the coarse grid limit, and DNS when the grid is fine enough to resolve down to the Kolmogorov length scale. This procedure also avoids the need for multiple filter levels or for defiltering. Mathematically the an FSM is any model which takes the form:

$$\tau(u_i, u_j) = f_{\Delta} R_{ij}^{\text{RANS}}, \quad (2.37)$$

where  $f_{\Delta}$  is a contribution function, and  $R_{ij}^{\text{RANS}}$  is the Reynolds stress computed from some conventional RANS model.

The Flow Simulation Methodology is therefore not a single model, but a general designation for any model that takes this form. The methodology consists of two parts: a contribution function, and an underlying RANS model. In order to calculate the length scales of the turbulence needed by the contribution function, it is preferable to use a two-equation RANS model, since such models are complete. To date, all work on the FSM has employed two-equation models. A variety of possible contribution functions have been explored. In addition to those discussed here, Hussaini et al. (2003) attempt to use renormalization group (RNG) methods to arrive at a form for the contribution function. Also, the limited numerical scales (LNS) approach of Batten et al. (2000), although not exactly taking the form (2.37), is basically a variation on the FSM.

### 2.3.1 The Contribution Function

The contribution function should locally approach unity in regions of coarse resolution and approach zero when the resolution is close to the Kolmogorov length scale.

Speziale (1998a,b) originally proposed a contribution function of the form

$$f_{\Delta} = \left[ 1 - \exp \left( -\frac{\delta}{\eta} \right) \right]^n \quad (2.38)$$

where  $\delta$  is a scale characterizing the filter,

$$\eta = \nu^{3/4} / \varepsilon^{1/4} \quad (2.39)$$

is an estimate of the Kolmogorov length scale, and  $n$  is a constant. For practically computations the filter scale is chosen proportional to the grid scale,  $\delta = \beta \Delta$  where  $\beta$  is a positive constant chosen to provide sufficient numerical resolution at a minimum of computation cost and  $\Delta$  is a characteristic grid spacing, which for the current work is set to  $(\Delta x \Delta y \Delta z)^{1/3}$ . (For further discussion see section 4.1.1). Bachman (2001) evaluated this contribution function for the case of a zero-pressure gradient boundary layer with  $\beta = 0.001 - 0.016$  and  $n = 1$  (Speziale's initial suggestion was  $\beta = 0.001$ ). His results show that the size of the smallest scales observed in the instantaneous flow decrease with increasing  $\beta$ , but the mean flow profile remains relatively unaffected as long as the contribution function does not exceed about 10% in the outer part of the boundary layer ( $\beta = 0.008$ ). Also using this contribution function Fasel et al. (2002) were able to achieve good results for the wall jet. Sandberg (2004) was reasonably successful in predicting the axisymmetric wake using this contribution function.

For flows in which a wider range of length scales are present the contribution function (2.38) was found to be less successful. In particular if the turbulent Reynolds number, which can be interpreted as a ratio of the largest and smallest length scales present in the flow, varies significantly across the flow field, this form for contribution function can have difficulties in properly identifying the coarse grid limit (Israel and Fasel, 2002). This suggests that the integral length scale, which represents the characteristic size of the largest eddies, may be important to the proper scaling of the model contribution. An alternative contribution function which replaces the Kol-

mogorov scale with the integral scale is

$$f_{\Delta} = \left[ 1 - \exp \left( -\frac{\delta}{\mathcal{L}} \right) \right]^n, \quad (2.40)$$

where the integral scale is estimated by

$$\mathcal{L} = \frac{k^{3/2}}{\varepsilon}. \quad (2.41)$$

One indication that the integral length scale is physically a good choice is that for this function a good calibration is obtained for  $\beta \sim 1$ . Israel and Fasel (2002) achieved limited success with this contribution function.

For the present investigations it has been found that a form that uses both the integral and Kolmogorov length scales is the least sensitive to  $\beta$  as well as numerically the most robust. An approximate form for the scaling can be obtained by taking the trace of (2.37). Since  $f_{\Delta}$  is a scalar, we must have

$$k = f_{\Delta} E,$$

where  $k$  is the subfilter energy, and  $E$  is the total turbulent energy. For high Reynolds number turbulence the bulk of the energy is contained in the inertial range, which follows a five-thirds decay law, as shown in figure 2.1. Estimating  $E$  as the area in the shaded region, and  $k$  as the area in the dark shaded region, we have

$$\int_{\kappa_{\eta}}^{\kappa_L} \kappa^{-5/3} d\kappa = f_{\Delta} \int_{\kappa_{\eta}}^{\kappa_c} \kappa^{-5/3} d\kappa$$

where  $\kappa_{\eta}$  is the wavenumber of the Kolmogorov dissipation scale,  $\kappa_L$  is the wavenumber of the integral scale, and  $\kappa_c$  is the wavenumber of the filter, or cutoff, scale. Integrating and solving for  $f_{\Delta}$  yields the following form, which is the contribution function used in the present work:

$$f_{\Delta} = \frac{\delta^{2/3} - \eta^{2/3}}{\mathcal{L}^{2/3} - \eta^{2/3}}. \quad (2.42)$$

Clipping is applied to insure that  $0 < f_{\Delta} < 1$ . This function is designed so as to recover a RANS model as the grid spacing approaches the integral scale, and a

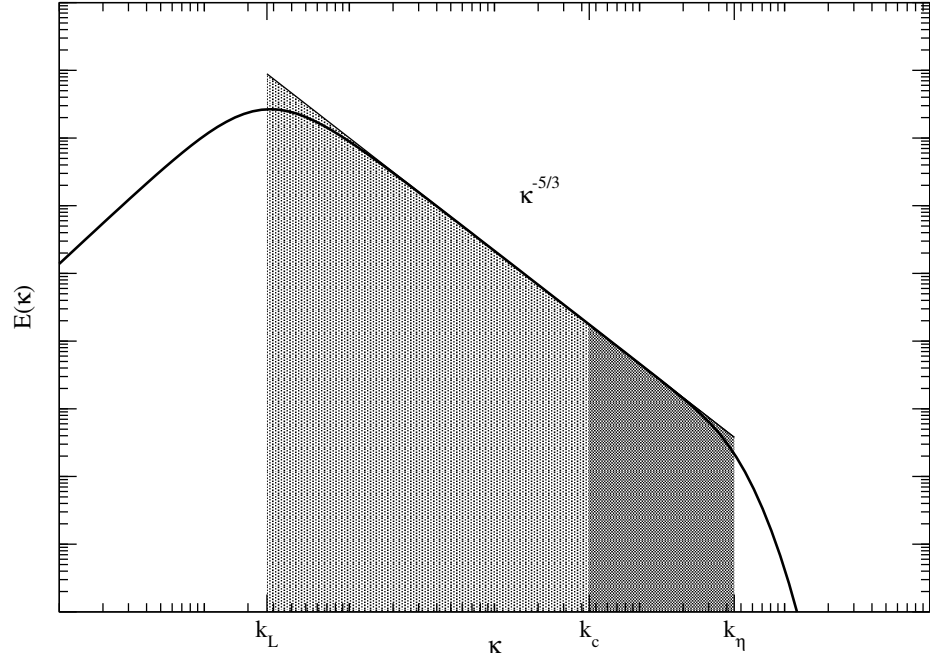


FIGURE 2.1. Schematic of the turbulent spectrum.

DNS as the grid spacing approaches the Kolmogorov length scale. Setting  $\delta = \beta\Delta$ , the limiting cases of  $\beta = 0$  and  $\beta \rightarrow \infty$  correspond to no model and a pure RANS simulation respectively. The specific form is motivated by a Kolmogorov inertial range five-thirds decay law, however this should not be considered a rigorous derivation since we do not necessarily expect to see a significant inertial spectrum in most of the flow domain. Except where otherwise noted a value of  $\beta = 1$  is used.

In principle, RANS values should be used for  $k$  and  $\varepsilon$  in the various length scale estimates above. However, in keeping with Speziale's original proposal, the subfilter values are used. This change should only affect  $\eta$  weakly, since most of the subfilter dissipation occurs at the smallest scales;  $L$ , however, will probably be underpredicted.

### 2.3.2 RANS Model

To complete the method, the FSM requires a RANS closure. In order to compute the length scales necessary for the contribution function, a two-equation model is preferred. Speziale (1998a) proposed using the ASM of Gatski and Speziale (1993). It is particularly important to employ a state of the art Reynolds stress closure for the FSM since, even if the mean flow is amenable to a simple closure, the structures themselves may be non-equilibrium, highly anisotropic, and have significant rotation effects. In the current work, the revised ASM model of Gatski and Jongen (2000) is employed. This eliminates this assumption that  $\mathcal{P}/\varepsilon$  is a constant, at the cost of requiring the solution of a cubic equation at each point in the flow field. However, it is found to be more robust.

## 2.4 Compressible Equations

In order to more clearly illustrate the principles underlying the FNS equations, they have thus far been derived under the assumption of incompressibility. However, for many problems it is important to retain the full compressible version of the equations. For aerodynamic applications compressibility effects often play an important role. Also, the compressible equations are hyperbolic in time; consequently, numerical methods for solving the compressible equations do not require the solution of an elliptic equation at each time step, as is the case for the incompressible Navier-Stokes. Since the solution can be advanced at each point using only data from neighboring points, very efficient distributed algorithms are possible for the compressible equations, which perform well on large parallel computers. However, the compressible equations do require certain additional model assumptions.



### 2.4.1 Thermodynamic Equations

In addition to the continuity and momentum equations, (2.1) and (2.2), a third transport equation is required for one of the thermodynamic variables. Expressing the internal energy of the fluid in terms of the temperature, the first law of thermodynamics can be used to obtain the following equation for the temperature,

$$\frac{\partial \rho C_v T}{\partial t} + \frac{\partial \rho C_v T u_i}{\partial x_i} = -p \frac{\partial u_i}{\partial x_i} - \frac{\partial q_i}{\partial x_i} + \sigma_{ij} \frac{\partial u_j}{\partial x_i} \quad (2.43)$$

where

$$q_i = -\lambda \frac{\partial T}{\partial x_i} \quad (2.44)$$

is the conductive heat flux. The thermal conductivity,  $\lambda$ , is obtained by assuming a constant Prandtl number,

$$\text{Pr} = \frac{\mu C_p}{\lambda}. \quad (2.45)$$

Since the mass and momentum are conserved quantities it is useful to express the energy equation in a conservative form. Using the momentum equation to derive an equation for the kinetic energy, and adding this to the temperature equation the following can be obtained for the evolution of the total energy,

$$\frac{\partial E}{\partial t} = \frac{\partial}{\partial x_i} [-u_i (E + p) - q_i + u_j \sigma_{ij}] \quad (2.46)$$

where

$$E = \rho \left( C_v T + \frac{1}{2} u^2 \right) \quad (2.47)$$

is the total energy.

The energy equation is supplemented with an equation of state of the form:

$$p = p(\rho, T),$$

which relates the three thermodynamic variables. For a gas the ideal gas law provides a good approximation to the state relationship as long as extreme thermodynamic

variations are not encountered. Assuming constant thermodynamic properties the ideal gas law is

$$p = C_v (\gamma - 1) \rho T. \quad (2.48)$$

Additionally, in compressible flow simulations it is common to drop the assumption of constant molecular viscosity, and instead use an experimentally derived curve fit to estimate the dependence of the viscosity on temperature. In these investigations the fluid is assumed to be air and Sutherland's law is used for this purpose. Sutherland's law is incorporated into the following dimensional piecewise curve-fits:

$$\mu(T) = \begin{cases} C_1 T_1, & T < T_1 \\ C_1 T, & T_1 < T < T_2 \\ C_2 \frac{T^{3/2}}{T + T_2}, & T > T_2 \end{cases} \quad (2.49)$$

with the constants

$$T_1 = 40.0 \text{ K}$$

$$T_2 = 110.4 \text{ K}$$

$$C_1 = 6.80698413 \times 10^{-8} \text{ N}\cdot\text{s}/\text{m}^2\cdot\text{K}$$

$$C_2 = 14.458 \times 10^{-7} \text{ N}\cdot\text{s}/\text{m}^2\cdot\text{K}^{1/2}$$

### 2.4.2 The Favre Filter

In the equations of motion for a compressible flow, the transport quantities are found in products with the density. In a DNS it is often convenient therefore to solve the Navier-Stokes equations in conservative form. When the equations are filtered this leads to filtered product terms of the form  $\overline{\rho f}$ . The need to model such terms can be avoided, and the filtered equations can be considerably simplified by introducing the Favre filter (denoted by a tilde) defined as:

$$\tilde{\rho f} = \overline{\rho f}. \quad (2.50)$$

Favre filtered variables are sometimes referred to as mass averaged. In the incompressible limit,  $\rho$  is a constant and  $\tilde{f} = \bar{f}$ . The fluctuating component relative to the Favre filter will be denoted by a double prime,

$$f = \tilde{f} + f''. \quad (2.51)$$

### 2.4.3 Compressible Filtered Navier-Stokes

Filtering the continuity equation (2.1) and using (2.50) we obtain for the filtered continuity equation,

$$\frac{\partial \bar{\rho}}{\partial t} + \frac{\partial \bar{\rho} \tilde{u}_i}{\partial x_i} = 0. \quad (2.52)$$

Spatial filtering the momentum equation (2.2) as before, and using (2.50) we obtain:

$$\frac{\partial \bar{\rho} \tilde{u}_i}{\partial t} + \frac{\partial \bar{\rho} \tilde{u}_i \tilde{u}_j}{\partial x_j} = -\frac{\partial \bar{p}}{\partial x_i} + \frac{\partial}{\partial x_j} [\bar{\sigma}_{ij} - \tau_{ij}] \quad (2.53)$$

where for the compressible equation

$$\tau_{ij} = \bar{\rho}(\widetilde{u_i u_j} - \tilde{u}_i \tilde{u}_j). \quad (2.54)$$

The filtered viscous stress tensor,

$$\bar{\sigma}_{ij} = 2 \left( \overline{\mu S_{ij}} - \frac{1}{3} \overline{\mu S_{kk}} \delta_{ij} \right) \quad (2.55)$$

introduces new unknown correlations of the form

$$\overline{\mu \frac{\partial u_i}{\partial x_j}}.$$

Erlebacher et al. (1992) and Zang et al. (1992) both assume that for small temperature fluctuations, it is adequate to assume

$$\bar{\sigma}_{ij} = 2 \left( \bar{\mu} \tilde{S}_{ij} - \frac{1}{3} \bar{\mu} \tilde{S}_{kk} \delta_{ij} \right) \quad (2.56)$$

where

$$\bar{\mu} = \mu(\tilde{T}). \quad (2.57)$$

#### 2.4.4 Resolved Scale Energy Equation

Unfortunately, directly filtering the total energy equation (2.46) leads to an equation that contains several new terms that need to be modeled. Worse, the resulting equation is for filtered total energy,

$$\overline{E_t} = \bar{\rho} \left( C_v \tilde{T} + \frac{1}{2} \tilde{u}^2 \right). \quad (2.58)$$

This quantity is not closed since  $\tilde{u}^2$  is not known. It is therefore preferable to construct the quantity  $E_R$ , resolved scale energy, which is defined as

$$E_R = \bar{\rho} \left( C_v \tilde{T} + \frac{1}{2} \tilde{u}^2 \right). \quad (2.59)$$

This quantity can be related to  $\overline{E_t}$  using the relation

$$\overline{E_t} = E_R - \frac{1}{2} \tau_{ii} \quad (2.60)$$

We can now derive the governing equation for  $E_R$  in the same manner as the equation for  $E_t$  is derived.

First we need to derive an equation for the resolved kinetic energy,  $\tilde{u}^2$ . Multiplying the resolved scale momentum equation (2.53) by  $\tilde{u}_i$ , yields

$$\tilde{u}_i \frac{\partial \bar{\rho} \tilde{u}_i}{\partial t} + \tilde{u}_i \frac{\partial \bar{\rho} \tilde{u}_i \tilde{u}_j}{\partial x_j} = -\tilde{u}_i \frac{\partial \bar{p}}{\partial x_i} + \tilde{u}_i \frac{\partial}{\partial x_j} [\overline{\sigma_{ij}} - \tau_{ij}] \quad (2.61)$$

$$\frac{\partial \bar{\rho} \tilde{u}_i \tilde{u}_i}{\partial t} + \frac{\partial \bar{\rho} \tilde{u}_i \tilde{u}_i \tilde{u}_j}{\partial x_j} = \tilde{u}_i \left[ \bar{\rho} \frac{\partial \tilde{u}_i}{\partial t} + \bar{\rho} \tilde{u}_j \frac{\partial \tilde{u}_i}{\partial x_j} \right] - \tilde{u}_i \frac{\partial \bar{p}}{\partial x_i} + \tilde{u}_i \frac{\partial}{\partial x_j} [\overline{\sigma_{ij}} - \tau_{ij}]. \quad (2.62)$$

Multiplying the continuity equation (2.52) by  $\tilde{u}_i$  we can rewrite the term in brackets to obtain

$$\frac{\partial \bar{\rho} \tilde{u}_i \tilde{u}_i}{\partial t} + \frac{\partial \bar{\rho} \tilde{u}_i \tilde{u}_i \tilde{u}_j}{\partial x_j} = \tilde{u}_i \left[ \frac{\partial \bar{\rho} \tilde{u}_i}{\partial t} + \frac{\partial \bar{\rho} \tilde{u}_i \tilde{u}_j}{\partial x_j} \right] - \tilde{u}_i \frac{\partial \bar{p}}{\partial x_i} + \tilde{u}_i \frac{\partial}{\partial x_j} [\overline{\sigma_{ij}} - \tau_{ij}]. \quad (2.63)$$

The right hand side can now be rewritten using the momentum equation (2.53), to get the equation for resolved scale turbulent kinetic energy:

$$\frac{1}{2} \frac{\partial \bar{\rho} \tilde{u}^2}{\partial t} + \frac{1}{2} \frac{\partial \bar{\rho} \tilde{u}^2 \tilde{u}_j}{\partial x_j} = \tilde{u}_i \left( -\frac{\partial \bar{p}}{\partial x_i} + \frac{\partial}{\partial x_j} [\overline{\sigma_{ij}} + \tau_{ij}] \right). \quad (2.64)$$

To obtain the filtered temperature equation for a compressible fluid we can filter (2.43) in a similar manner as the momentum equation:

$$\frac{\partial \bar{\rho} C_v \tilde{T}}{\partial t} + \frac{\partial \bar{\rho} C_v \widetilde{T u_i}}{\partial x_i} = -\overline{p \frac{\partial u_i}{\partial x_i}} - \frac{\partial \bar{q}_i}{\partial x_i} + \overline{\sigma_{ij} \frac{\partial u_i}{\partial x_j}}. \quad (2.65)$$

Introducing a subfilter-scale heat flux, corresponding to the subfilter-scale stress tensor (2.54)

$$Q_i = \bar{\rho} C_v (\widetilde{T u_i} - \tilde{T} \tilde{u}_i) \quad (2.66)$$

we can write

$$\frac{\partial \bar{\rho} C_v \tilde{T}}{\partial t} + \frac{\partial \bar{\rho} C_v \tilde{T} \tilde{u}_i}{\partial x_i} = -\overline{p \frac{\partial u_i}{\partial x_i}} - \frac{\partial}{\partial x_i} [\bar{q}_i + Q_i] + \overline{\sigma_{ij} \frac{\partial u_i}{\partial x_j}} \quad (2.67)$$

where right hand side is still not closed without additional assumptions to model the filtered correlations. The filtered convective heat flux requires similar treatment to the viscous stress tensor term,

$$\bar{q}_i = -\bar{\lambda} \frac{\partial \tilde{T}}{\partial x_i}. \quad (2.68)$$

We can now write the equation for resolved scale energy,  $E_R$ , by summing (2.64) and (2.67), and rearranging indices,

$$\frac{\partial E_R}{\partial t} + \frac{\partial \tilde{u}_i E_R}{\partial x_i} = -\overline{p \frac{\partial u_i}{\partial x_i}} - \frac{\partial}{\partial x_i} [\bar{q}_i + Q_i] + \overline{\sigma_{ij} \frac{\partial u_i}{\partial x_j}} + \tilde{u}_i \left( -\frac{\partial \bar{p}}{\partial x_i} + \frac{\partial}{\partial x_j} [\bar{\sigma}_{ij} - \tau_{ij}] \right). \quad (2.69)$$

We would like to rewrite this equation in a form similar to (2.46) so that we can work with the same simple form of the equations. This is rendered difficult due to the presence of disparate types of filtering in the pressure and molecular stress terms.

The pressure terms can be rewritten as

$$\begin{aligned} -\overline{p \frac{\partial u_i}{\partial x_i}} - \tilde{u}_i \frac{\partial \bar{p}}{\partial x_i} &= -\frac{\partial \bar{p} \tilde{u}_i}{\partial x_i} + \left( \bar{p} \frac{\partial \tilde{u}_i}{\partial x_i} - \overline{p \frac{\partial u_i}{\partial x_i}} \right) \\ &= -\frac{\partial \bar{p} \tilde{u}_i}{\partial x_i} - \left( \overline{\bar{p} \frac{\partial \tilde{u}_i}{\partial x_i}} - \bar{p} \frac{\partial \tilde{u}_i}{\partial x_i} + \overline{\bar{p} \frac{\partial u_i''}{\partial x_i}} + \overline{p' \frac{\partial \tilde{u}_i}{\partial x_i}} + \overline{p' \frac{\partial u_i''}{\partial x_i}} \right) \end{aligned} \quad (2.70)$$

Following Erlebacher et al. (1992) we conclude that the last three terms in parenthesis are negligible. The first two terms could be calculated explicitly if we knew the

implicit filter, but they give a purely fluctuating component, which can be neglected, since it should not contribute to the evolution of the filtered fields. Based on the discussion in section 2.2.2, this is only exactly true for a projection operator. The viscosity term can be handled similarly,

$$\begin{aligned} \overline{\sigma_{ij} \frac{\partial u_i}{\partial x_j}} + \tilde{u}_i \frac{\partial \overline{\sigma_{ij}}}{\partial x_j} &= \frac{\partial \tilde{u}_i \sigma_{ij}}{\partial x_j} + \left( \overline{\sigma_{ij} \frac{\partial u_i}{\partial x_j}} - \overline{\sigma_{ij}} \frac{\partial \tilde{u}_i}{\partial x_j} \right) \\ &= \frac{\partial \tilde{u}_i \sigma_{ij}}{\partial x_j} + \left( \overline{\sigma_{ij} \frac{\partial \tilde{u}_i}{\partial x_j}} - \overline{\sigma_{ij}} \frac{\partial \tilde{u}_i}{\partial x_j} + \overline{\sigma_{ij} \frac{\partial u_i''}{\partial x_j}} + \sigma'_{ij} \frac{\partial \tilde{u}_i}{\partial x_j} + \sigma'_{ij} \frac{\partial u_i''}{\partial x_j} \right) \end{aligned} \quad (2.71)$$

where we again neglect the terms in parentheses.

The last term of (2.69) can be rewritten as (noting that  $\tau_{ij}$  is symmetric):

$$\begin{aligned} \tilde{u}_j \frac{\partial \tau_{ij}}{\partial x_i} &= \frac{\partial}{\partial x_i} [\tilde{u}_j \tau_{ij}] - \tau_{ij} \frac{\partial \tilde{u}_j}{\partial x_i} \\ &= \frac{\partial}{\partial x_i} [\tilde{u}_j \tau_{ij}] - \frac{1}{2} \left( \tau_{ij} \frac{\partial \tilde{u}_j}{\partial x_i} + \tau_{ji} \frac{\partial \tilde{u}_i}{\partial x_j} \right) \\ &= \frac{\partial}{\partial x_i} [\tilde{u}_j \tau_{ij}] - \tau_{ij} \tilde{S}_{ij} \end{aligned} \quad (2.72)$$

The final form of the resolved energy equation is then:

$$\frac{\partial E_R}{\partial t} = \frac{\partial}{\partial x_i} [-\tilde{u}_i (E_R + \bar{p}) - (\bar{q}_i + Q_i) + \tilde{u}_j (\overline{\sigma_{ij}} - \tau_{ij})] + \tau_{ij} \tilde{S}_{ij} \quad (2.73)$$

This equation is not conservative because of the subfilter dissipation term; this corresponds to the production term in the  $k$  equation and represents the transfer of energy from the resolved to the subfilter scales.

The ideal gas equation (2.48) can be filtered directly,

$$\bar{p} = C_v (\gamma - 1) \bar{\rho} \tilde{T}. \quad (2.74)$$

The thermal conductivity is modeled by a constant Prandtl number,

$$\bar{\lambda} = \frac{\bar{\mu} C_p}{\text{Pr}}. \quad (2.75)$$

### 2.4.5 Compressible FSM

To employ the FSM for compressible flow requires two relatively minor changes. First, a model is required for the subfilter heat flux,  $Q_i$ . Second, the underlying RANS model must be replaced with one designed for compressible flow.

For the subfilter heat flux a contribution function is employed in a manner completely analogous to (2.37):

$$Q_i = f_{\Delta} Q_i^{\text{RANS}}. \quad (2.76)$$

The same contribution function (2.42) is used for both the subfilter stress and the subfilter heat flux.

For the low Mach number flows considered in this work there are no significant compressibility effects that require modeling. The compressible  $k - \varepsilon$  equations are modeled using

$$\frac{\partial \bar{\rho} k}{\partial t} + \frac{\partial \bar{\rho} \tilde{u}_j k}{\partial x_j} = \frac{\partial}{\partial x_j} \left[ \left( \bar{\mu} + \frac{\mu_T}{\text{Pr}_k} \right) \frac{\partial k}{\partial x_j} \right] - \bar{\rho} \tau_{ij} \widetilde{S}_{ij} - \bar{\rho} \varepsilon \quad (2.77)$$

$$\frac{\partial \bar{\rho} \varepsilon}{\partial t} + \frac{\partial \bar{\rho} \tilde{u}_j \varepsilon}{\partial x_j} = \frac{\partial}{\partial x_j} \left[ \left( \bar{\mu} + \frac{\mu_T}{\text{Pr}_{\varepsilon}} \right) \frac{\partial \varepsilon}{\partial x_j} \right] + C_{\varepsilon 1} \frac{\varepsilon}{k} \bar{\rho} \tau_{ij} \widetilde{S}_{ij} - C_{\varepsilon 2} f_{\varepsilon 2} \bar{\rho} \frac{\varepsilon^2}{k} \quad (2.78)$$

For the diffusion terms of the  $k - \varepsilon$  equations the eddy viscosity is computed as

$$\mu_T = C_{\mu} \frac{\bar{\rho} k^2}{\varepsilon}. \quad (2.79)$$

The singularity in the dissipation term of the  $\varepsilon$  equation is removed with the wall damping function

$$f_{\varepsilon 2} = 1 - \exp \left( \frac{y \sqrt{k}}{C^* \nu} \right), \quad (2.80)$$

with  $C^* = 12$ .

To complete the closure requires an algebraic relation for the Reynolds stress tensor, which we compute using a state of the art algebraic stress model (ASM). This model contains higher order algebraic terms of the invariants of the strain rate and vorticity tensors which model non-equilibrium turbulent effects. In his original formulation of the FSM Speziale (1996) proposed using the ASM of Gatski and Speziale

(1993). Although good results were obtained using this model (e. g. Bachman, 2001) the current calculations employ the revised ASM model of Gatski and Jongen (2000).

The stress tensor is written as:

$$R_{ij}^{\text{RANS}} = \frac{2}{3}\rho k - 2\nu_T \left[ \left( S_{ij} - \frac{1}{3}S_{kk}\delta_{ij} \right) a_2 a_4 (S_{ik}W_{kj} - W_{ik}S_{kj}) - 2a_3 a_4 \left( S_{ik}S_{kj} - \frac{1}{3}S_{kl}S_{kl}\delta_{ij} \right) \right] \quad (2.81)$$

where

$$\nu_T = -\alpha_1 \rho \frac{k^2}{\varepsilon} \quad (2.82)$$

and

$$\left( \frac{\alpha_1}{\tau} \right)^3 - p \left( \frac{\alpha_1}{\tau} \right)^2 + q \left( \frac{\alpha_1}{\tau} \right) + r = 0. \quad (2.83)$$

The coefficients in the cubic equation (2.83) are given by

$$p = \frac{\gamma_1^*}{\eta^2 \tau^2 \gamma_0^*} \quad (2.84a)$$

$$q = \frac{1}{(2\eta^2 \tau^2 \gamma_0^2)^2} \left( \gamma_1^{*2} - 2\eta^2 \tau^2 \gamma_0^* a_1 - \frac{2}{3}\eta^2 \tau^2 a_3^2 + 2\xi^2 \tau^2 a_2^2 \right) \quad (2.84b)$$

$$r = \frac{\gamma_1^* a_1}{(2\eta^2 \tau^2 \gamma_0^2)^2} \quad (2.84c)$$

with



$$\eta = \sqrt{S_{ij}S_{ij}} \quad (2.85a)$$

$$\xi = \sqrt{W_{ij}W_{ji}} \quad (2.85b)$$

$$a_1 = \frac{1}{2} \left( \frac{4}{3} - C_2 \right) \quad (2.85c)$$

$$a_2 = \frac{1}{2} (2 - C_4) \quad (2.85d)$$

$$a_3 = \frac{1}{2} (2 - C_3) \quad (2.85e)$$

$$a_4 = \tau \left( \gamma_1^* - 2\gamma_0^* \left( \frac{\alpha_1}{\tau} \right) \eta^2 \tau^2 \right)^{-1} \quad (2.85f)$$

$$\gamma_0^* = \frac{C_1^1}{2} \quad (2.85g)$$

$$\gamma_1^* = \frac{1}{2} C_1^0 + \frac{C_{\varepsilon 2} - C_{\varepsilon 2}}{C_{\varepsilon 1} - 1}. \quad (2.85h)$$

The following value are used for the model constants:

$$\begin{aligned} C_{\varepsilon 1} &= 1.44 & C_{\varepsilon 2} &= 1.83 \\ C_1^0 &= 3.4 & C_1^1 &= 1.8 \\ C_2 &= 0.36 & C_3 &= 1.25 & C_4 &= 0.4 \end{aligned} \quad (2.86)$$

The cubic is solved using the solution procedure outlined in the appendix of Rumsey and Gatski (2001). The turbulent heat flux is modeled using an eddy conductivity,

$$Q_i = \frac{C_v \mu_T}{\text{Pr}_T} \frac{\partial \tilde{T}}{\partial x_i}. \quad (2.87)$$

### Chapter 3

## NUMERICAL METHOD

And yet, someone who might have difficulty consciously working out what  $3 \times 4 \times 5$  comes to would have no trouble in doing differential calculus and a whole host of related calculations so astoundingly fast that they can *actually catch a flying ball*.

DOUGLAS ADAMS, *Dirk Gently's Holistic Detective Agency*

Two different CFD codes were used for the results presented here. The original intention was to perform all the calculations with an high-order accurate explicit code based on the numerical method of Thumm (1991) which was originally designed for investigations of supersonic transition on a flat-plate. The method was subsequently refined by Harris (1995) and was adapted for the plane wake. Preliminary calculations, however, indicated that for the “hump” model at the experimental Reynolds number the timestep requirements for the explicit code were too severe. Since no equivalent high-order accurate implicit code was available, the second-order code CFL3D, developed by NASA Langley Research Center, was employed. This chapter describes the numerical method used by each code.

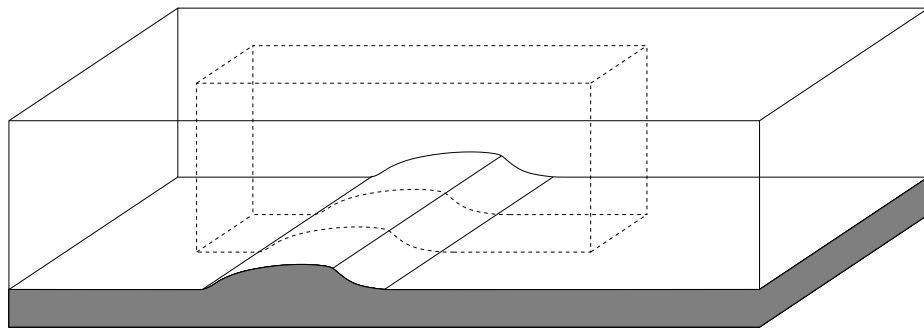


FIGURE 3.1. Computational domain

### 3.1 Virtual Fluid Dynamics

VFD++ (Virtual Fluid Dynamics in C++) is a C++ class library that was developed as part of the research effort to simplify the implementation and testing of a variety of turbulence models. Time-stepping algorithms, spatial discretization schemes, difference equations, and boundary conditions are all implemented using C++ classes and virtual functions. This allows the user to create modules to implement new equations, stencils, boundary conditions, etc., and to combine equations and numerical procedures in a modular fashion. Grid classes provide the vector calculus operators gradient and divergence so that equations can be written independently of the grid transformation. Template meta-programming techniques are used to optimize the most important computational loops in order to be performance competitive with Fortran. (Veldhuizen, 2000) Parallelization uses the Message Passing Interface (MPI) and is implemented in the low level subroutines so that new equations may be implemented independently from the parallelization.

The numerical method for the simulations presented here is essentially the same as that originally developed by Thumm (1991) for linear stability and transition studies, and later adapted by Harris (1995) for the plane wake and von Terzi (2004) for the backward facing step. The time advancement algorithm is a fourth-order explicit Runge-Kutta method in a memory conserving formulation Harris (1995). Spatial differences are computed using second order split-differences at each step with alternating direction so as to sum to fourth-order (Tukel et al., 1976).

The spatial differences stencils are slightly different than those given in Harris (1995), since a third order stencil is used at the boundaries. The stencil used for interior points is

$$(\delta f)_i = \frac{1}{6} (-f_{i+2} + 8f_{i+1} - 7f_i),$$

with the direction of the stencil alternating for the upwind and downwind steps. On the boundaries the same stencil is used for the downwind steps, with the following

Step	$x$ -derivative	$y$ -derivative	$z$ -derivative
1	U	U	U
2	D	D	U
3	U	D	U
4	D	U	U
5	U	U	D
6	D	D	D
7	U	D	D
8	D	U	D
9	U	U	U
$\vdots$	$\vdots$	$\vdots$	$\vdots$

(U) Upwind/(D) Downwind

TABLE 3.1. Splitting algorithm.

stencils used for the upwind steps:

$$\begin{aligned}
 (\delta f)_0 &\simeq \frac{1}{6}(-15f_0 + 28f_1 - 17f_2 + 4f_3) \\
 (\delta f)_1 &\simeq \frac{1}{6}(-4f_0 + f_1 + 4f_2 - f_3).
 \end{aligned}$$

Reducing the order of the stencils on the boundary improves stability, but should not affect the global convergence rate (Gustafsson, 1975).

For three-dimensional simulations Thumm (1991) used a pseudo-spectral decomposition across the span. This yields significant improvement in numerical accuracy for linear stability calculations in which the disturbances are applied in Fourier eigenmodes. In turbulent calculations, where the coherent structures are no longer expected to have a harmonic shape, the advantage of this decomposition is less clear. Furthermore, for the highly nonlinear model equations it is computationally advantageous to work entirely in physical space. All the simulations presented here are therefore performed entirely in physical space. The same split stencils are used for the spanwise derivatives, with the splitting algorithm expanded to an eight step cycle, as shown in table 3.1. Inner derivatives are always taken in the opposite direction as the outer derivatives.

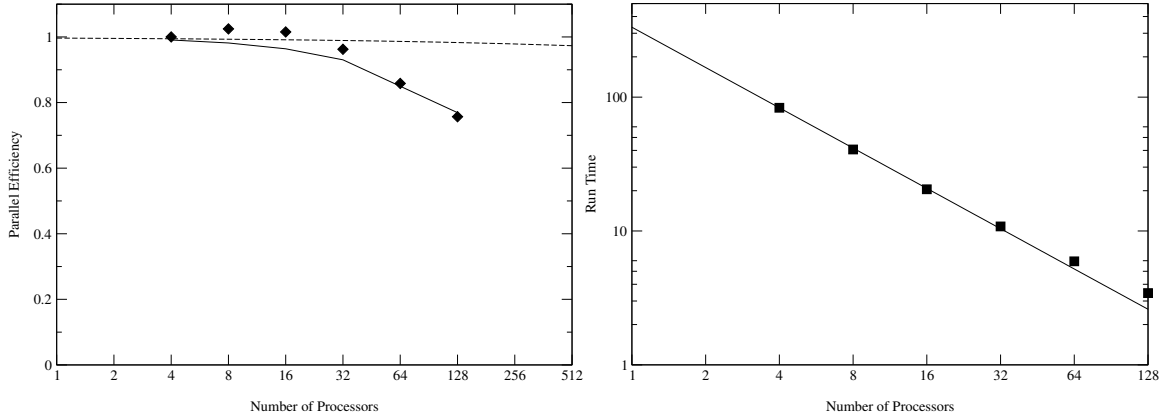


FIGURE 3.2. Parallel efficiency (left) and runtime (right).

The code is parallelized using MPI. Rather than using a traditional ghost cell approach, in which boundary data is updated after each sub-step, the boundary data communication is localized to the differencing subroutine. Spanwise periodicity does not need to be explicitly implemented, instead it is specified using the topology options available through the MPI library. In this approach, communication occurs in every differencing operation, rather than once per sub-step, however only two boundary lines need to be communicated, instead of four. Also, the governing equations are not solved at any duplicate or unnecessary data points. This allows the method to scale to smaller block sizes. The code has been successfully run on up to 128 processors with near linear speed-up. Figure 3.1 shows the run time and the parallel efficiency for various numbers of processors. The parallel efficiency is defined as

$$\eta = \frac{T_{\text{Single Processor}}}{N_{\text{CPUs}} T_{\text{Wallclock}}}. \quad (3.1)$$

The super-linear speed up observed up to 16 processors is due to cache effects.

### 3.1.1 Curvilinear Coordinate Transform

Thumm (1991) designed his code for a uniform rectangular grid. Harris (1995) added affine grid stretching along the  $x$  and  $y$  coordinate axis. The current code further

extends the method by allowing for an arbitrary curvilinear coordinate system. Although the code can support a transform in all three coordinate directions, for the simulations presented here a transform was applied only in the  $x - y$  plane. The implementation is therefore described with that simplification.

The code uses a formulation that is designed to preserve the conservation properties of the Navier-Stokes equations. The FNS equations are not conservative, but by using a slight modification of this formulation, it is assured that those terms which are conservative remain so in the transformed equations. The FNS equations, along with the  $k - \varepsilon$  transport equations, can be expressed in a vector form as

$$\frac{\partial \mathbf{U}}{\partial t} + \frac{\partial \mathbf{E}(\mathbf{U})}{\partial x} + \frac{\partial \mathbf{F}(\mathbf{U})}{\partial y} + \frac{\partial \mathbf{G}(\mathbf{U})}{\partial z} + \mathbf{H}(\mathbf{U}) \quad (3.2a)$$

where  $\mathbf{U} = (\bar{\rho}, \bar{\rho}\tilde{u}, \bar{\rho}\tilde{v}, \bar{\rho}\tilde{w}, E_R, \bar{\rho}k, \bar{\rho}\varepsilon)^T$  and

$$\mathbf{E} = \begin{pmatrix} \bar{\rho}\tilde{u} \\ \bar{\rho}\tilde{u}\tilde{u} - \bar{p}(\bar{\sigma}_{xx} - \tau_{xx}) \\ \bar{\rho}\tilde{u}\tilde{v} - (\bar{\sigma}_{xy} - \tau_{xy}) \\ \bar{\rho}\tilde{u}\tilde{w} - (\bar{\sigma}_{xz} - \tau_{xz}) \\ \tilde{u}(E_R + \bar{p}) + (\bar{q}_x + Q_x) - \tilde{u}(\bar{\sigma}_{xx} - \tau_{xx}) - \tilde{v}(\bar{\sigma}_{xy} - \tau_{xy}) - \tilde{w}(\bar{\sigma}_{xz} - \tau_{xz}) \\ \bar{\rho}\tilde{u}k - \left(\mu + \frac{\mu_T}{\text{Pr}_k}\right) \frac{\partial k}{\partial x} \\ \bar{\rho}\tilde{u}\varepsilon - \left(\mu + \frac{\mu_T}{\text{Pr}_\varepsilon}\right) \frac{\partial \varepsilon}{\partial x} \end{pmatrix} \quad (3.2b)$$

$$\mathbf{F} = \begin{pmatrix} \bar{\rho}\tilde{v} \\ \bar{\rho}\tilde{u}\tilde{v} - (\bar{\sigma}_{xy} - \tau_{xy}) \\ \bar{\rho}\tilde{v}\tilde{v} + \bar{p} - (\bar{\sigma}_{yy} - \tau_{yy}) \\ \bar{\rho}\tilde{v}\tilde{w} - (\bar{\sigma}_{yz} - \tau_{yz}) \\ \tilde{v}(E_R + \bar{p}) + (\bar{q}_y + Q_y) - \tilde{u}(\bar{\sigma}_{xy} - \tau_{xy}) - \tilde{v}(\bar{\sigma}_{yy} - \tau_{yy}) - \tilde{w}(\bar{\sigma}_{yz} - \tau_{yz}) \\ \bar{\rho}\tilde{v}k - \left(\mu + \frac{\mu_T}{\text{Pr}_k}\right) \frac{\partial k}{\partial y} \\ \bar{\rho}\tilde{v}\varepsilon - \left(\mu + \frac{\mu_T}{\text{Pr}_\varepsilon}\right) \frac{\partial \varepsilon}{\partial y} \end{pmatrix} \quad (3.2c)$$

$$\mathbf{G} = \begin{pmatrix} \bar{\rho}\tilde{w} \\ \bar{\rho}\tilde{u}\tilde{w} - (\bar{\sigma}_{xz} - \tau_{xz}) \\ \bar{\rho}\tilde{v}\tilde{w} - (\bar{\sigma}_{yz} - \tau_{yz}) \\ \bar{\rho}\tilde{w}\tilde{w} + \bar{p} - (\bar{\sigma}_{zz} - \tau_{zz}) \\ \tilde{w}(E_R + \bar{p}) + (\bar{q}_z + Q_z) - \tilde{u}(\bar{\sigma}_{xz} - \tau_{xz}) - \tilde{v}(\bar{\sigma}_{yz} - \tau_{yz}) - \tilde{w}(\bar{\sigma}_{zz} - \tau_{zz}) \\ \bar{\rho}\tilde{w}k - \left(\mu + \frac{\mu_T}{\text{Pr}_k}\right) \frac{\partial k}{\partial z} \\ \bar{\rho}\tilde{w}\varepsilon - \left(\mu + \frac{\mu_T}{\text{Pr}_\varepsilon}\right) \frac{\partial \varepsilon}{\partial z} \end{pmatrix} \quad (3.2d)$$

$$\mathbf{H} = \begin{pmatrix} 0 \\ 0 \\ 0 \\ 0 \\ -\bar{\rho}\tau_{ij}\bar{S}_{ij} \\ \bar{\rho}\tau_{ij}\bar{S}_{ij} + \bar{\rho}\varepsilon \\ -C_{\varepsilon 1} \frac{\varepsilon}{k} \bar{\rho}\tau_{ij} (\bar{S}_{ij} - \frac{1}{3}\bar{S}_{kk}\delta_{ij}) + C_{\varepsilon 2} f_{\varepsilon 2} \bar{\rho} \frac{\varepsilon^2}{k} \end{pmatrix} \quad (3.2e)$$

It should be noted that the filtered mass and momentum equations remain conservative, while the resolved scale energy equation has a single dissipation term which represents the transfer of energy to the subfilter scales. The  $k$  and  $\varepsilon$  equation both have production and dissipation terms.

The inner derivatives in the flux vectors can be computed using the chain rule,

$$\frac{\partial}{\partial x} = \xi_x \frac{\partial}{\partial \xi} + \eta_x \frac{\partial}{\partial \eta} \quad (3.3a)$$

$$\frac{\partial}{\partial y} = \xi_y \frac{\partial}{\partial \xi} + \eta_y \frac{\partial}{\partial \eta}. \quad (3.3b)$$

Equation (3.2a) is then expressed in terms of the computational coordinates  $\xi, \eta$  in conservative form as

$$\frac{\partial(J\mathbf{U})}{\partial t} + \frac{\partial}{\partial \xi} [J(\mathbf{E}\xi_x + \mathbf{F}\xi_y)] + \frac{\partial}{\partial \eta} [J(\mathbf{E}\eta_x + \mathbf{F}\eta_y)] + \frac{\partial \mathbf{G}}{\partial z} + J\mathbf{H} \quad (3.4a)$$

where

$$J = \begin{vmatrix} x_\xi & x_\eta \\ y_\xi & y_\eta \end{vmatrix} \quad (3.4b)$$

is the Jacobian of the grid transformation. The Jacobian is evaluated numerically at start up using second-order central differences.

### 3.1.2 Boundary Conditions

The computational domain is shown in figure 3.1. At the lower wall the no-slip condition is enforced for velocity, and a constant temperature is specified. For the  $k-\varepsilon$  equations,  $k$  is set to zero, as is the wall normal derivative of  $\varepsilon$ . For simulations of the LaRC experiments, the upper boundary is treated as a no stress wall to eliminate the necessity of resolving the upper wall boundary layer. The experimental data shows that this boundary layer is thin, and therefore it should have no appreciable impact on the flow field at the lower surface.

Dirichlet conditions are used for all variables at the inflow, and the second derivative of all conservative variables are set to zero at the outflow. Since the flow is subsonic, there is one upstream characteristic, which is fixed by imposing a constant value for pressure at the outflow. To allow disturbances to leave at the inflow, following Harris (1995), the pressure on the inflow is set using extrapolation rather than the state equation.

Disturbances are introduced by wall normal blowing and suction. For the steady suction case (see section 5.3) the slot velocity distribution is given by

$$v(x) = -A\sqrt{\frac{16}{5}}\sin^3(\pi x), \quad (3.5)$$

where  $A$  is the steady suction amplitude. For periodic forcing a dipole slot is used:

$$v(x, t) = A(t)\sqrt{\frac{32}{5}}\sin^2(\pi x)\sin(2\pi x), \quad (3.6)$$

where the amplitude,  $A(t) = A\sin(\omega t)$  is now varies sinusoidally in time.

## 3.2 CFL3D

For the high Reynolds number cases considered in chapter 6 the CFL restriction makes simulation with an explicit code too computationally expensive. (For example, the cases presented here would require  $\sim 200,000$  timesteps per forcing period.) Instead



the simulations were performed using CFL3D, a CFD code developed at NASA Langley Research Center and made freely available by NASA under an export restricted licensing agreement. Although CFL3D is actually a thin-layer Navier-Stokes solver it has been used with reasonable success for complex geometries. It was among the codes used by NASA for their own simulations for the CFD Validation 2004 Workshop. In addition to being an implicit code, CFL3D was chosen because it already includes the Gatski and Jongen (2000) EASM model used in the FSM. The complete capabilities of CFL3D can be found in the User Manual (Krist et al., 1998). The features used in the current investigations are briefly outlined here.

The governing equations in CFL3D are the thin-layer Navier-Stokes equations. The thin-layer approximation is made in each of the three spatial dimensions separately and the remaining viscous terms can be activated for each direction independently. With all viscous terms turned off CFL3D can be used as Euler solver. For the simulations presented here the viscous terms (both laminar and turbulent) are retained in all three directions. This is equivalent to neglecting the cross-derivative terms in the full Navier-Stokes equations. It is not obvious that this approximation should work well in separated flow. However Rumsey et al. (1987) show that CFL3D performs reasonably well even in such cases.

CFL3D is a finite volume code. The spatial derivative terms are separated into convective and viscous flux terms. The viscous flux terms are computed using an upwind biased third order method (`rkap0=0.3333`) with flux difference splitting according to the method of Roe (`ifds=1`) and no flux limiting (`iflim=0`). Both the molecular and turbulent viscous terms are evaluated with second-order central differences.

A pseudo-time ( $\tau$ -TS) time advancement is employed. In addition to the physical time variable  $t$  there is a pseudo-time variable  $\tau$ . At each discrete time step in physical time, the pseudo-time is advanced a fixed number of sub-iterations, ideally until a steady state is reached. The time stepping for the pseudo-time variable,  $\tau$ , is first

order and fully implicit. In the limit of complete convergence for  $\tau$  the resulting scheme for the advancement of physical time,  $t$ , is second order. However, the code is generally run for a fixed number of sub-iterations. The number of subiterations used is discussed in section 6.1.1. For each sub-iteration, the solution can be further improved using a multigrid method. The number of multigrid levels available depend on the details of the grid, and therefore varied among the cases presented here. Further details on the numerical method, as well as precise explanations of the parameters settings listed above can be found in Krist et al. (1998).

The boundary conditions are similar to those used in the explicit code. A steady RANS turbulent profile is imposed at the inflow boundary. In order to allow upstream pressure disturbances to exit the domain, density, velocity,  $k$ , and  $\varepsilon$  are set to fixed values, and the pressure is extrapolated from the interior. (CFL3D boundary condition type `bctype=2008`.) The inflow profile is generated by using the stand alone turbulent boundary layer solver described in appendix B.2, with the leading edge placed the same distance upstream of the inflow boundary as in the experiments.

At the outflow an extrapolation boundary condition is employed with the pressure fixed to the ambient pressure. (`bctype=2002`) The strongly stretched grid serves to dissipate the outgoing disturbances before they reach the boundary since in the highly stretched region the FSM model recovers a steady RANS, i.e.,  $f_\Delta \rightarrow 1$ . As for the explicit code, a no-slip lower wall (`bctype=2004`) and a no-stress upper wall (`bctype=1005`) are employed.

### 3.3 Grid Generation

Both VFD++ and CFL3D are formulated for arbitrary structured Cartesian grids. Orthogonality is not required. Nevertheless it can be shown (Thompson et al., 1985) that the leading order error term is inversely proportional to  $\sin \theta$ , where  $\theta$  is the angle formed by the grid coordinate lines. An orthogonal grid will therefore minimize

the numerical error.

Duraiswami and Prosperetti (1992) propose a method for generating orthogonal grids based on conformal maps. Typically grid generation involves the mapping of a general quadrilateral domain onto a uniform computational rectangle. Conformal mapping alone is not sufficient for this purpose, since a conformal map cannot map a general quadrilateral onto a specific rectangle such that vertices are mapped to vertices. Nevertheless it is possible to use a conformal map to transform a general quadrilateral onto a rectangle if the aspect ratio of the rectangle is left as an additional free parameter of the mapping. The resulting rectangle can then be trivially transformed to onto the computational rectangle by simply rescaling one linear dimension. The resulting map preserves orthogonality but not volume. Such a map is called *quasi-conformal* and the aspect ratio of the intermediate rectangle turns out to be a unique property of the original quadrilateral, called the *quasi-conformal module*.

To control the cluster of grid points Duraiswami and Prosperetti (1992) compose two additional mappings, an affine transform in each grid direction. The complete sequence of mappings is illustrated in figure 3.3. Mathematically the complete mapping can be performed in one step according to the grid transformation equations

$$\frac{\partial}{\partial \xi} \left[ f \frac{\partial x}{\partial \xi} \right] + \frac{\partial}{\partial \eta} \left[ \frac{1}{f} \frac{\partial x}{\partial \eta} \right] = 0 \quad (3.7a)$$

$$\frac{\partial}{\partial \xi} \left[ f \frac{\partial y}{\partial \xi} \right] + \frac{\partial}{\partial \eta} \left[ \frac{1}{f} \frac{\partial y}{\partial \eta} \right] = 0 \quad (3.7b)$$

where  $f(\eta, \xi) = Ma(\eta)b(\xi)$  is a separable function that controls the local grid aspect ratio. The constant  $M$  is the quasi-conformal module of the region. The functions  $a(\eta)$  and  $b(\xi)$  are the affine transformations which control the grid line clustering, and which must satisfy the normalizations

$$\int_0^1 a(\eta) d\eta = 1 \quad (3.8a)$$

$$\int_0^1 b(\xi) d\xi = 1. \quad (3.8b)$$

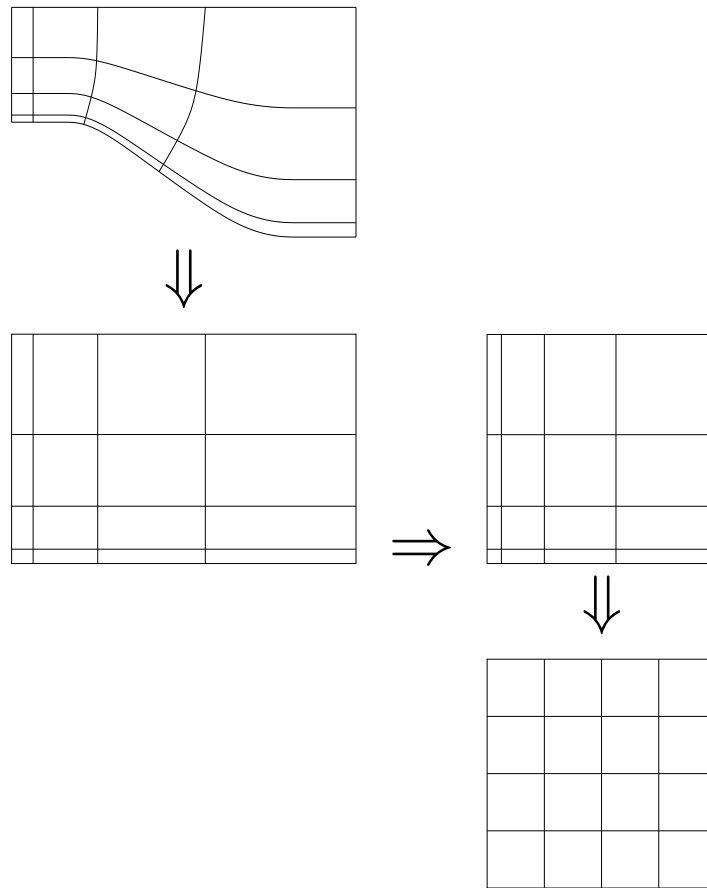


FIGURE 3.3. Schematic of the grid mapping. Starting with the computational domain (top left) a conformal map is applied, followed by a linear stretching onto the unit square, followed by an affine transformation to produce a uniform coordinate distribution (lower right).

As implemented by Duraiswami and Prosperetti, the conformal module of the physical geometry is required in order to solve the grid transform equations. Letting  $Q$  be the general quadrilateral and  $M(Q)$  be the conformal module of  $Q$ , it can be shown that if  $P_i$  is a sequence of polygons such that

$$\lim_{i \rightarrow \infty} P_i = Q \quad (3.9)$$

then

$$\lim_{i \rightarrow \infty} M(P_i) = M(Q). \quad (3.10)$$

Since the quasi-conformal module of a polygon is much easier to compute than that of a general curvilinear quadrilateral, they used a series of polygonal approximations to obtain the module. For the geometry of the hump model the physical domain is almost rectangular. It was found that using the aspect ratio of the enclosing rectangle as an estimate of the quasi-conformal module of the hump geometry was sufficient to produce acceptable grids.

The functions  $a(\eta)$  and  $b(\xi)$  are third order polynomials. For  $a(\eta)$ , which provides the near wall clustering, the function

$$a(\eta) = A + 3(1 - A)\eta^2 \quad (3.11)$$

is used, where  $A$  is the stretching parameter.  $A$  is approximately the proportion by which the spacing at the wall has been reduced (for  $A = 1$  there is no stretching). In order to allow clustering around a point,  $\xi_0$ , in the middle of the domain, the following function is used for  $b(\xi)$ :

$$b(\xi) = B + \frac{1 - B}{\frac{1}{3} - \xi_0 + \xi_0^2}(\xi - \xi_0)^2 \quad (3.12)$$

where  $B$  controls the strength of the clustering (Postl, Personal Communication). The clustering in the downstream direction is used to maintain grid density on the concave section of the ramp, since the quasi-conformal mapping tends to cluster points near convex regions and away from concave regions.

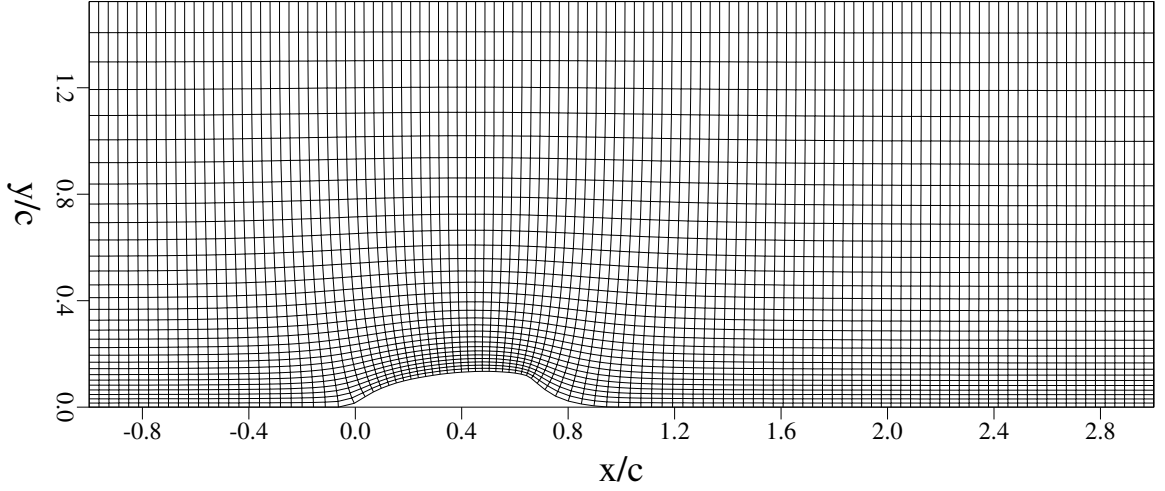


FIGURE 3.4. Computational grid. Every fifth point in  $y$  and tenth point in  $x$  is shown. The stretched region actually extends to  $x/c = 14.0$ .

Orthogonality is imposed through the boundary condition

$$\frac{\partial x}{\partial \xi} \frac{\partial x}{\partial \eta} + \frac{\partial y}{\partial \eta} \frac{\partial y}{\partial \xi} = 0. \quad (3.13)$$

The remaining boundary condition is obtained by requiring the points to lie on the desired boundary curve,

$$F(x, y) = 0. \quad (3.14)$$

For the curved lower wall boundary, cubic splines are used to approximate the boundary curve, from the QA data provided by the experimentalists.

The grid generation equation (3.7a) and its associated boundary conditions (3.13) and (3.14) are solved using successive over-relaxation (SOR). For three dimensional cases the grid is generated in two dimensions and extruded uniformly across the span. As part of the outflow treatment, a strongly stretched rectangular grid is patched onto the end of the domain. A typical grid is shown in figure 3.4.

## Chapter 4

# ERROR ANALYSIS AND TURBULENCE MODEL VALIDATION

“You mean it’s okay to say something that’s wrong as long as the reason is right.”

“Of course. Why else go to the trouble of being a rational animal?”

UMBERTO ECO, *Foucault’s Pendulum*

For simulations of laminar flows the error, defined as the difference between the exact solution of the Navier-Stokes equations and the computed solution of the discretized equations, is determined purely by the numerical scheme employed. For unsteady simulations of turbulent flows, due to the chaotic nature of the flow field, global convergence cannot be achieved over physically relevant timescales using any computationally affordable timestep and grid spacing. Consequently the error is measured in terms of statistics of the flow. (Using statistics in this way is highly non-trivial, as will be shown in section 4.1.) This introduces an additional source of error associated with the convergence of the statistics as approximated from a finite time series, which will be referred to as the averaging error. If the turbulent flow is computed using a model equation, rather than the Navier-Stokes equations, then a third error is introduced, the modeling error.

Ideally, when performing a simulation a desired error tolerance would be specified and the sum of the errors would be required to be smaller than this specified tolerance. In reality the available computational resources and the available time to solve the problem are often what determines the error. Since one of the error terms may dominate the total error it is important to understand the magnitude of each term and the relative cost for reducing each term individually. In this way effort can be targeted toward reducing the dominant error term, and practical limitations on the

accuracy can be understood.

In this chapter each of these error terms will be considered separately. The expected forms of each of the error terms will be analyzed and the mathematical tools used to evaluate them will be briefly introduced. This discussion should establish three things: (1) that the largest error is likely to be the averaging error, (2) that the cost of reducing the averaging error is prohibitive, and (3) that the averaging error is only available as an error bound, and can not be held constant as the other errors terms are investigated. This means that for any validation study, errors smaller than the averaging error cannot be determined. Although this may appear to be an insurmountable problem, it is offset by the fact that in a predictive calculation the averaging error is the term which governs the overall error, and therefore in real world applications numerical and modeling errors need only be made smaller than the averaging error.

## 4.1 Numerical Errors

### 4.1.1 Grid Convergence for Large-Eddy Simulation

Consider the FNS equations (2.8) and (2.10), closed using the standard Smagorinsky model, eq. 1.12 (the argument may be trivially generalized to any model parameterized in terms of a cutoff length scale). The eddy viscosity is:

$$\nu_T = \ell^2 |\mathbf{S}|.$$

The length scale  $\ell$  is a parameter which must be specified. In this form the model is a PDE which, in theory, can be solved exactly for any specified value of  $\ell$ . If one is to perform a grid resolution study for a discretization of this PDE it is necessary to hold  $\ell$  fixed as the grid is refined. If instead the length scale is chosen in a fixed ratio to the grid width,  $\ell = C_S \Delta$ , as is commonly done, then the resulting equation is no longer purely a PDE. If the grid is refined holding  $C_S$  constant, the discretized



equation is formally consistent not with a turbulence model equation, but rather is consistent to second order (in the “model” term) with the unfiltered Navier-Stokes equations.

To better clarify the meaning of  $\ell$ , consider the following thought experiment. Perform a wall resolved DNS for a specified flow. Then perform a series of standard Smagorinsky LES simulations for the same flow, holding  $\ell$  fixed, while refining the grid. By comparing the spectrum extracted from the DNS to the spectrum from the fully grid converged LES it should be possible to estimate what the filter for the LES model is. Pope (2000) points out that this filter is implicitly defined by the model. He further points out that this *implicit Smagorinsky filter* is the filter represented by the overbar in the FNS equations, and it is different than any explicitly applied filter which may be used in the numerical solution procedure. Extending this line of argument, it is possible to extract a characteristic filter width,  $\delta$  from the LES data. Considering the physical arguments underlying the model, it is reasonable to expect that  $\delta$  is roughly proportional to  $\ell$ . Note that the constant of proportionality,  $C_\ell = \ell/\delta$ , is a property of the Smagorinsky model considered as a PDE, and is not the same as the Smagorinsky coefficient  $C_S$  which is related to the grid spacing. We can relate the two constants by defining a coefficient  $\beta$  which represents the number of grid points required to resolve one characteristic filter width. The model then becomes,

$$\nu_T = (C_\ell \beta \Delta)^2 |\mathbf{S}|,$$

where  $C_\ell \beta = C_S$ . From this analysis it is clear that the Smagorinsky coefficient represents the combined effect of both a model property and a grid resolution parameter. In this sense there is no physically “correct” value of  $C_S$ . If  $C_S$  is sufficiently small the simulation will be underresolved. If  $C_S$  is sufficiently large, the filter width will be too large relative to the size of the energy containing eddies. In this light it must be understood that the value of  $C_S$  proposed by Lilly (1967) is really a calibration

for  $C_\ell$ .

#### 4.1.2 Model of the Error

To better illustrate the behavior of the error terms, consider the following model. Let  $\bar{u}$  be the solution to the FNS equations closed with a turbulence model with a characteristic filter width,  $\delta$ . For an order  $n$  numerical method the discretization error contains terms that are typically of the form

$$\text{Discretization Error} \propto \Delta^n \frac{\partial^n \bar{u}}{\partial x^n}. \quad (4.1)$$

In order to obtain an estimate for the derivative term note that (Pope, 2000)

$$\begin{aligned} \left\langle \left( \frac{\partial^n \bar{u}}{\partial x^n} \right)^2 \right\rangle &\sim \int_0^\infty \kappa^{2n} \bar{E}(\kappa) d\kappa \\ &= \int_0^\infty \kappa^{2n} \hat{G}(\kappa) C \varepsilon^{2/3} \kappa^{-5/3} d\kappa \end{aligned} \quad (4.2)$$

where  $\hat{G}(\kappa)$  is the implied filter associated with the turbulence model. Since  $\hat{G}(\kappa)$  is dependent on  $\delta$ , so too is the integral in (4.2). To recast this integral in a form independent of  $\delta$ , we can express the implicit filter as  $\hat{G}(\kappa) = g(\kappa\delta)$ , where  $g$  is a filter kernel shape which is independent of  $\delta$ . So,

$$\left\langle \left( \frac{\partial^n \bar{u}}{\partial x^n} \right)^2 \right\rangle \sim C \varepsilon^{2/3} \int_0^\infty \kappa^{2n-5/3} g(\kappa\delta) d\kappa \quad (4.3)$$

$$= C \varepsilon^{2/3} \delta^{2/3-2n} \int_0^\infty \kappa'^{2n-5/3} g(\kappa') d\kappa' \quad (4.4)$$

where we note that the integral is now independent of  $\delta$ . Substituting this into the expression for the discretization error yields

$$\begin{aligned} \text{Discretization Error} &\propto \Delta^n \delta^{1/3-n} \\ &= \beta^{1/3-n} \Delta^{1/3}, \end{aligned} \quad (4.5)$$

or,

$$= \beta^{-n} \delta^{1/3}. \quad (4.6)$$

where  $\delta = \beta \Delta$ . (Note that there is no requirement that the filter width,  $\delta$ , be chosen proportional to the local filter width. However since this form is commonly used, and is employed in the current work, it is useful to consider.) One important consequence of this analysis is that if a conventional grid refinement study is performed, in which the grid is refined while keeping the model parameters constant, i.e.,  $\Delta \rightarrow 0$  while  $\beta = \text{constant}$ , then the discretization error will scale with  $\Delta^{1/3}$ , regardless of the order of the numerical method. Nevertheless, higher order methods still retain an advantage in that, for a fixed value of  $\beta$  (that is, a fixed number of points per characteristic filter width) the discretization error is likely to be smaller for higher order methods, due to the  $\beta^{-n}$  term.

Now assuming that the subfilter stress scales as  $\delta^2$ , and noting that most models to leading order also scale as  $\delta^2$ , it is reasonable to assume that the model error term is also second order, or at least no worse than second order. Combining these two estimates we can write

$$\text{Total Error} = \text{Discretization Error} + \text{Model Error} \quad (4.7)$$

$$= C_1 \beta^{-n} \delta^{1/3} + C_2 \delta^2, \quad (4.8)$$

or,

$$= C_1 \beta^{1/3-n} \Delta^{1/3} + C_2 \beta^2 \Delta^2 \quad (4.9)$$

Note that the constant  $\beta$  serves essentially the same role as the FSM  $\beta$  coefficient in the contribution functions (2.38), (2.40), and (2.42), and as the Smagorinsky coefficient,  $C_S$ , in the Smagorinsky model (1.12). Similar coefficients appear in most LES models.

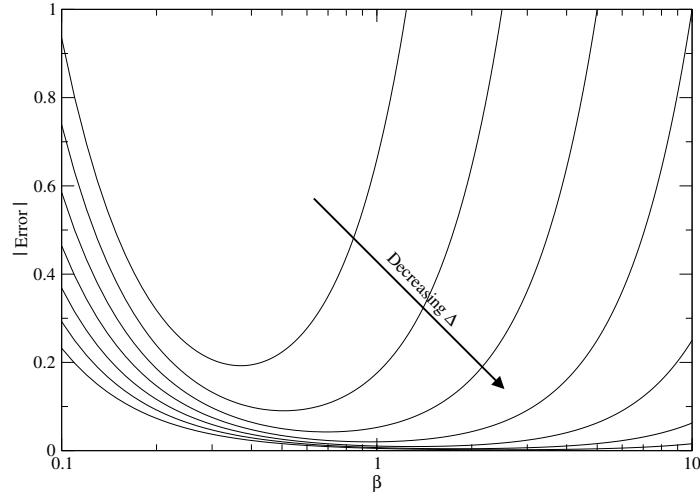


FIGURE 4.1. Behavior of the total (discretization plus model) error, based on the error model (4.9).

The behavior of (4.9) is plotted in figure 4.1. The different curves are for different grid resolutions, with finer grids resulting in a lower total error. For coarse grids there is a clear optimal value of  $\beta$ . For finer grids, however, there is a large range of values for which the error is small, that is, for which the resulting filter width is small relative to the largest scales of the turbulent motion, but still large relative to the grid spacing. So the error is much less sensitive to  $\beta$  for finer grids.

What is important to note is optimal values of  $\beta$  (or  $C_S$  in a Smagorinsky model) culled from numerical studies really only represent the best trade off between numerical and model error for that particular case. The values are therefore both grid and problem dependent. This helps to explain the wide range of “optimal”  $C_S$  values reported in the literature.

It should also be noted that figure 4.1 is based on an order of magnitude analysis. For small values of  $\beta$  we expect that the model will be insufficiently dissipative, whereas for large values of  $\beta$  (the RANS limit) the model dissipation will be too high.

For a code, such as CFL3D, which is dissipative in the leading order error terms, this implies that the discretization error and the model error will tend to combine for high  $\beta$  and to cancel for smaller  $\beta$ . In the  $\beta = 0$  limit, this is precisely the rationale for ILES methods (see section 2.2.3).

### 4.1.3 Convergence of Chaotic Systems

In conventional numerical error analysis the error is defined as the time dependent difference between the exact and numerical solutions. The global error is measured by a quantity such as the  $L^2$ -norm of the instantaneous error. It will be noted that in the previous section the description of a grid convergence study for the FNS equation is given in terms of the error in the statistics of the solution rather than the error in the solution itself. The reason is that for simulations of turbulence it is observed that attaining convergence of the instantaneous solution over a finite time interval is impossible, whereas the statistics are observed to converge. This is a phenomena common to chaotic problems. In order to better understand the behavior, and to justify this use of the statistics of an unconverged solution, it is helpful to look at a lower order model problem.

Consider an iterative mapping  $H : \mathbb{R}^2 \rightarrow \mathbb{R}^2$  defined by:

$$\begin{aligned} x_{i+1} &= y_i + 1 - 1.4x_i^2 \\ y_{i+1} &= 0.3x_i. \end{aligned} \tag{4.10}$$

This is the Hénon map (Hénon, 1976). Although deterministic, this mapping is a chaotic process. Informally this means that the sequence of points generated by this mapping appears to be random, and that the map exhibits sensitive dependence on initial conditions. By sensitive dependence on initial conditions it is meant that there exist pairs of points which are infinitesimally close together but which can be sent a fixed finite distance apart by the action of a finite number of iterations of the map.

Sensitive dependence on initial conditions poses a significant problem for numer-

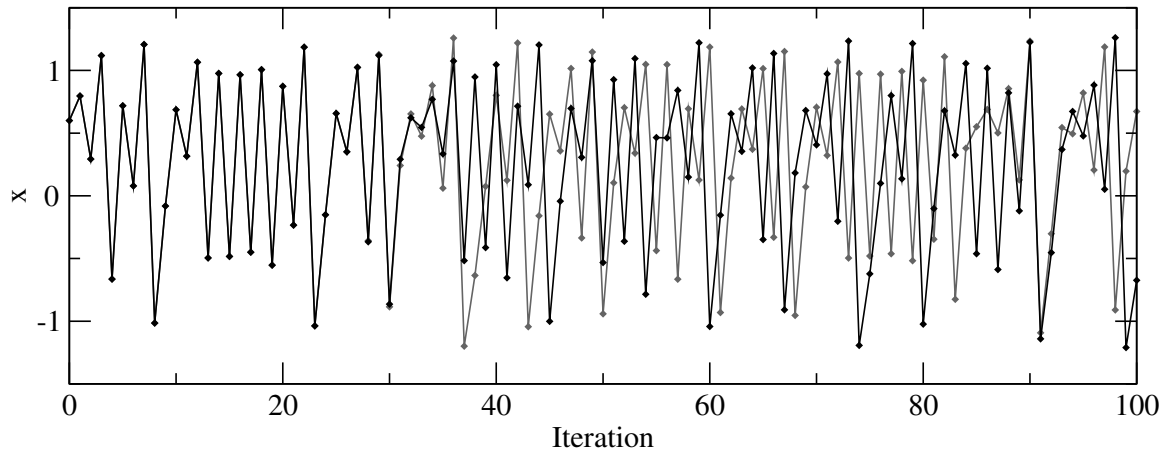


FIGURE 4.2. 100 iteration of  $x$  for the Hénon map with the initial condition  $(x, y) = (1, 1)$ . The grey line is single precision, the black is double precision.

ical simulations. Figure 4.2 shows  $\{x_i\}$  for 100 iterations of the Hénon map. Two realizations are shown: one is computed in single precision arithmetic, the other in double precision. The difference in the round-off error is enough to cause the two solutions to diverge within about 50 iterations. In light of this sensitivity it is reasonable to ask whether it is possible to investigate the “real” (that is, exact) behavior of the map.

If the sequence of points generated by the map is plotted on the Cartesian plane, the results form a distinct pattern (figure 4.3). This is the Hénon attractor. An attractor is a set of points which are invariant under the mapping and to which some larger superset of points eventually tend towards under repeated iterations of the mapping. The Hénon attractor is a *strange attractor* which has a complex and fractal structure as can be seen in the expanded views in the figure. What is more important for our purposes is that in spite of the pointwise divergence of the two realizations show in figure 4.2, the shape of the attractor is virtually unchanged down to the fine scale structure.

This type of behavior is observed in many chaotic systems, and is generally ex-

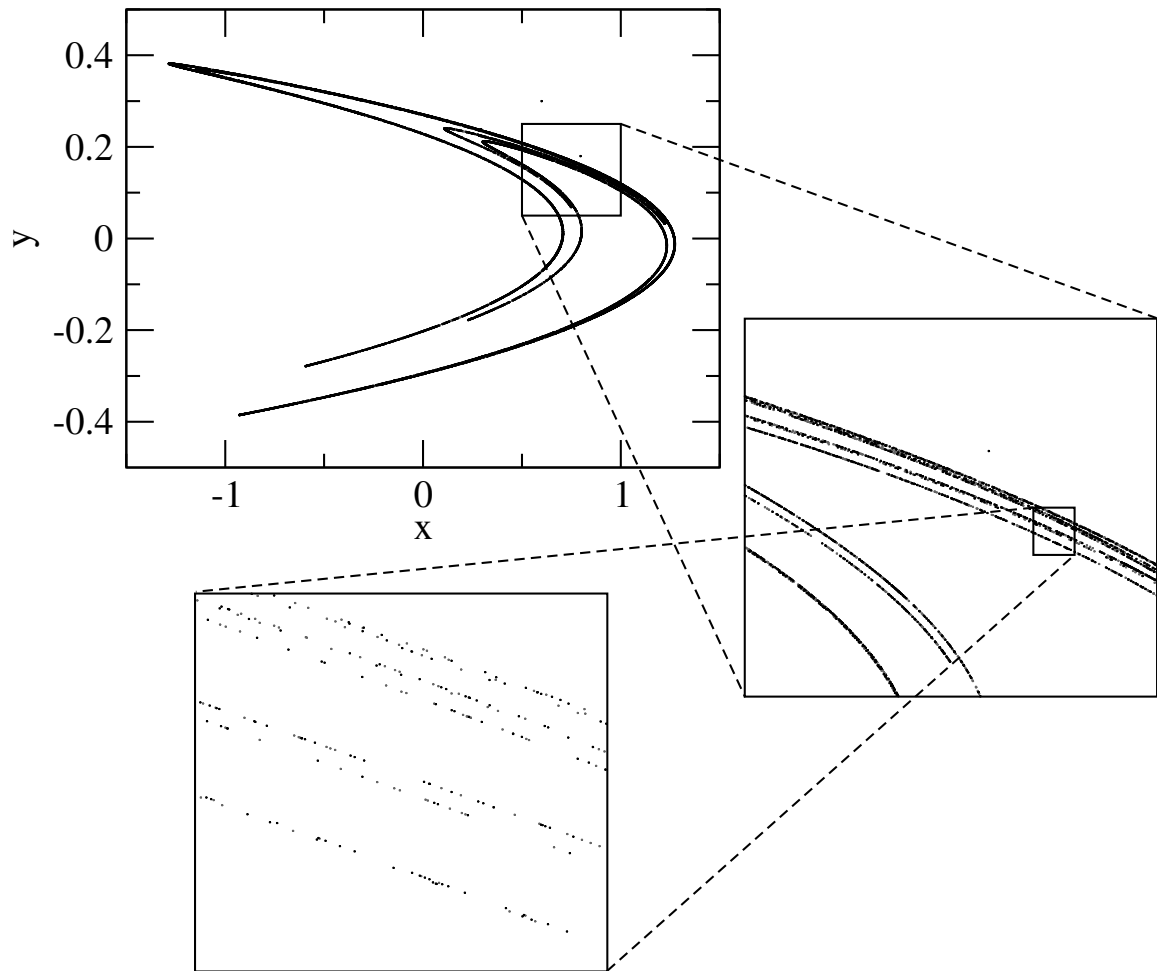


FIGURE 4.3. The Hénon attractor (10,000 points are shown). Both single precision (grey) and double precision (black) realizations are shown.

plained by in terms of a *shadowing property* (Pilyugin, 1999). The shadowing property for a particular mapping is a statement that a slightly perturbed version of the mapping (such as that induced by a finite precision numerical simulation) is in some sense close to some exact history of the unperturbed mapping. More formally we can consider a metric space  $(X, r)$ , where  $X$  is the set and  $r : (X, X) \rightarrow \mathbb{R}$  is the metric, and a mapping

$$\phi : X \rightarrow X. \quad (4.11)$$

Define an orbit as a sequence generated by iterating the map,

$$O(x) = \{\phi^n(x) | n \in \mathbb{N}, x \in X\}. \quad (4.12)$$

We now define a  $\delta$ -pseudo orbit as a sequence  $\{x_i\}$  with the property

$$r(x_{i+1}, \phi(x_i)) < \delta. \quad (4.13)$$

The pseudo-orbit does not have to be generated by a specific mapping, although in the case of interest here it is generated by the numerical procedure (with round-off errors included). The pseudo-orbit can be thought of as the result of a numerical realization for which there is an upper bound on the error committed at any single time advancement step.

An orbit  $O(x_0)$  is said to  $\epsilon$ -shadow a pseudo-orbit if

$$r(x_i, \phi^i(x_0)) < \epsilon, \quad (4.14)$$

that is, if the distance between the orbit and the pseudo-orbit remains bounded forever. What we want is a statement that given a number  $\epsilon > 0$  we can find a  $\delta > 0$  such that any  $\delta$ -pseudo orbit is  $\epsilon$ -shadowed by some orbit. This would imply that although a particular numerical realization will diverge from the exact orbit  $O(x_0)$  generated from the identical initial conditions, the realization is still within  $\epsilon$  of *some* real orbit, albeit with a slightly perturbed initial condition, provided the error at each iteration step is made small enough.



It is interesting to note that there is, in fact, no proof available for a shadowing property for the Hénon map. Nevertheless, evidence from numerical experiments, such as the results in figure 4.3, show that it is extremely likely that the Hénon map has this or some similar property.

Most available shadowing results are for systems with a small finite number of degrees of freedom. Turbulence is a problem with an infinite number of degrees of freedom, at least when considered in the infinite Reynolds number limit. For a finite Reynolds number the number of degrees of freedom is still enormous, scaling with  $Re^{9/4}$ . Even for an FNS or VLES approach a formal shadowing theorem is unlikely to be available.

Berkooz (1994) gives several reasons why shadowing is not sufficient to explain the convergence of statistics in a turbulence simulation. First, it is not clear that the Navier-Stokes equations have a shadowing property. (The same objection applies for the FNS equations with a closure model.) In fact, many flows have symmetries which make it likely that there is not a shadowing property. Second, many systems have a shadowing property only in particular subsets. This means that numerical errors may send the solution out of the region in which the shadowing property holds. Third, there is no guarantee that the shadowed orbit is representative of a “typical” solution. For example, the shadowed orbit could be a limit cycle with a very small basin of attraction.

In spite of these issues, it is observed in numerical simulations that turbulent statistics do appear to converge. Berkooz (1994) proposes that this reflects some “deeper dynamical properties of the equations.” Sigeti (1996) presents numerical evidence suggesting that the presence of a region of exponential decay in the high wave number spectrum of a simulation of a chaotic (or turbulent) system is a good indicator that the dynamics have been correctly captured. In what follows it is assumed that the turbulent statistics predicted by the simulations converge in a well behaved manner. However, it should be noted that significant further research is

needed in this area, without which it cannot be definitively asserted that convergence of turbulence statistics will not fail for certain cases.

## 4.2 Averaging Errors

The enormous computational cost in modeling time dependent turbulent flows means that often only a very short physical time can be simulated. While experiments may collect data over thousands of characteristic times, numerical simulations may be limited to less than one hundred. As a result, convergence of statistics collected from simulations may be quite poor. Generally the errors associated with time averaging are assessed only qualitatively. However, in order to properly quantify the numerical and modeling errors present in a particular simulation, it is absolutely necessary to have a quantitative measure of the averaging error.

Given a series of measurements of some variable  $\{x_i\}$ , with a mean value

$$\bar{x} = \frac{1}{N} \sum_{i=1}^N x_i, \quad (4.15)$$

the error is expressed as the standard deviation of the mean,  $\sqrt{\sigma^2/N}$ , where  $\sigma^2$  is the sample variance,

$$\text{var}[x] = \sigma^2 = \frac{1}{N} \sum_{i=1}^N (x_i - \bar{x})^2. \quad (4.16)$$

Formally, if the data points,  $x_i$ , are statistically independent, then the standard deviation of the mean is related to the variance of the mean by,

$$\text{var}[\bar{x}] = \frac{\sigma^2}{N}. \quad (4.17)$$

However, for typical numerical simulations data is available with a high enough time resolution that the points are definitely not statistically independent. In this case the variance of the mean can be approximated (for large  $N$ ) as

$$\text{var}[\bar{x}] = \frac{2\pi\sigma^2}{N} f(0) \quad (4.18)$$

where  $f(\omega)$  is the normalized spectral density function,

$$f(\omega) = \frac{1}{2\pi} \sum_{r=-\infty}^{\infty} e^{-i\omega r} \rho(r). \quad (4.19)$$

and  $\rho(r)$  is the auto-correlation function (Priestly, 1981, section 5.3.2).

Since  $f(\omega)$  is not known, it is estimated by fitting an AR(2) process to the data, with parameters  $a_1, a_2$ . For a discrete AR(2) process, the following formula can be used (Priestly, 1981, equation 4.10.12):

$$f(0) = \frac{(1 - a_2) [(1 + a_2)^2 - a_1^2]}{2\pi (1 + a_2) [(1 - a_2)^2 + a_1^2 + 2a_1(1 - a_2) + 4a_2]}. \quad (4.20)$$

In the remainder of this work all error bars represent the square root of the variance of the mean,  $\sqrt{\text{var}[\bar{x}]}$ , as estimated by this method.

One very important consequence of (4.18) is that the averaging error only decreases as the square root of the computational cost. The cost of reducing the numerical error, however, will scale with the order of the numerical method; therefore the numerical error can be decreased much more cheaply than the averaging error. Consequently it may often be worthwhile to perform simulations with grids and timesteps that are “good enough” in order to focus computational resources on obtaining a long enough time series to obtain well converged statistics. In particular, when comparing different simulations it is important to check that the averaging error is not larger than the effect of whatever parameter changes (whether discretization, modeling, or physical parameters) are being considered.

### 4.3 A Posteriori Analysis

The implicit nature of the model filter, as discussed in section 2.2.1, has important implications for model validation. Experimental and DNS data is unfiltered. Results from model calculations using the FNS equations are filtered values. Since defiltering is generally an ill-posed problem, in principle it is necessary to filter the experimental

or DNS data in order to compare it with FNS results. Such a comparison is called a *a posteriori* analysis. However, due to the implicit nature of the filter, the filter which must be applied in order to make the comparison correct is unknown.

Actually, from a purely theoretical point of view, the problem is even greater than what is typically presented in the literature. By filtering the Navier-Stokes equations to remove the small scales information has been lost. Consequently it is impossible for the result of a FNS simulation to actually track a full Navier-Stokes solution. More precisely, if we let  $v$  denote a solution of the FNS equations coupled with some specific closure model, *there is no reason to expect that there exists a filter operator,  $\mathcal{G}$ , and a corresponding valid solution to the Navier-Stokes equations,  $u$ , such that*

$$v = \mathcal{G}[u].$$

It is widely recognized (see Lesieur, 1990, for example) that the true intention of LES is to reproduce the same statistics (to some order) as the original flow, and perhaps mimic the dynamics of the large structures. This criteria stands in contradiction to the standard development of the LES equations in terms of a specific deterministic filter. However, it remains beyond the scope of the present work to address this issue except to suggest that perhaps a dynamical systems approach, similar to the shadowing theorems discussed in section 4.1.3, might provide a promising avenue for further investigating the problem.

#### 4.3.1 Mean Flow

In practice the simplest statistics to obtain from experiments are time averaged moments. Generally this means either mean flow quantities (first order moments) or Reynolds stresses (second order moments). These are easy to compute for most experiments. For time accurate FNS simulations time averaging yields not the time mean quantities,  $\langle \phi \rangle$ , but the time averaged filtered quantities,  $\langle \overline{\phi} \rangle$ . That these are not equivalent in general can be easily seen by considering a shear flow profile, for

example, and a spatial convolution filter applied across the layer. Nevertheless, since the filter should ideally only effect small scale motions, and since the time average filters out the small scales, it is reasonable to assume that

$$\langle \overline{\phi} \rangle \approx \langle \phi \rangle. \quad (4.21)$$

This assumption can also be viewed from the reverse perspective. In principle, if the FNS filter was known the experimental data could be filtered to obtain  $\langle \overline{\phi} \rangle$ . In practice this is impossible since the implicit filter is not known. However, even were the filter available this procedure would only be useful for validating models where exact data is available, but not for predictive calculations which would require defiltering to back out the needed data from the FNS calculation. Therefore (4.21) can be understood as a necessary condition for a model to be a useful predictive tool, and it is fair to simply assert it as a requirement of a properly formed model that its implicit filter obeys (4.21).

Higher order moments are computed using the same assumption. The most common moment of interest is the Reynolds stress which can be written

$$\langle u'_i u'_j \rangle = \langle u_i u_j \rangle - \langle u_i \rangle \langle u_j \rangle. \quad (4.22)$$

The Reynolds stress from the FNS simulation is then approximated as

$$\begin{aligned} \langle \overline{u_i u_j} \rangle - \langle \overline{u_i} \rangle \langle \overline{u_j} \rangle &= \langle \overline{u_i} \overline{u_j} + \tau(u_i, u_j) \rangle - \langle \overline{u_i} \rangle \langle \overline{u_j} \rangle \\ &= \underbrace{\langle \overline{u_i} \overline{u_j} \rangle - \langle \overline{u_i} \rangle \langle \overline{u_j} \rangle}_{\text{resolved stress}} + \underbrace{\langle \tau(u_i, u_j) \rangle}_{\text{model stress}}. \end{aligned} \quad (4.23)$$

Similarly, for compressible flows we have

$$R_{ij} = \underbrace{\langle \overline{\rho} \tilde{u}_i \tilde{u}_j \rangle - \langle \overline{\rho} \rangle \langle \tilde{u}_i \rangle \langle \tilde{u}_j \rangle}_{\text{resolved stress}} + \underbrace{\langle \tau_{ij} \rangle}_{\text{model stress}} \quad (4.24)$$

### 4.3.2 Phase Averages

If in addition to mean quantities it is desired to investigate the physics of large coherent structures it becomes necessary to identify a procedure for extracting such

structures from the data. The literature on coherent structures for turbulence is quite extensive, suffice it to say that there is no single agreed upon definition of what constitutes a coherent structure. Among the more popular methods are proper orthogonal decomposition (POD) and vortex identification parameters such as the  $Q$  or  $\lambda_2$  criteria (Dubief and Delcayre, 2000). One simple model for coherent structures in a turbulent flow is the triple decomposition associated with the phase average (Reynolds and Hussain, 1972). This decomposition has been successfully used to model growth rates for several types of turbulent shear flows in which large coherent structures are present (Reau and Tumin, 2002a,b).

The phase average is defined as

$$\hat{\phi}(t) = \lim_{N \rightarrow \infty} \frac{1}{N} \sum_{n=1}^N \phi(t + n\Delta t), \quad (4.25)$$

where  $\Delta t$  is the period. Again we make the assumption that

$$\hat{\phi} \approx \hat{\bar{\phi}}. \quad (4.26)$$

This assumption is justifiable when there is a large separation of scales between the period of the phase average and the timescale associated with the filter width. For larger filter widths, this assumption may break down. In this case it may again be better to understand (4.26) as a condition on the model, rather than an assumption about filters in general.

For purposes of analysis, Reynolds and Hussain (1972) decomposed the flow into three components: a mean flow, a purely fluctuating phase averaged component, and the random incoherent fluctuations:

$$\phi = \underbrace{\langle \phi \rangle}_{\text{mean flow}} + \underbrace{(\hat{\phi} - \langle \phi \rangle)}_{\text{periodic fluctuations}} + \underbrace{(\phi - \hat{\phi})}_{\text{non-periodic fluctuations}} \quad (4.27)$$

In validating the FSM a slightly different decomposition is more natural. The primary term is a phase averaged (mean and fluctuating) component. The remaining

incoherent fluctuations are decomposed into resolved and unresolved (or subfilter) components:

$$\phi = \underbrace{\hat{\phi}}_{\text{coherent}} + \underbrace{(\bar{\phi} - \hat{\phi})}_{\text{resolved fluctuations}} + \underbrace{\phi'}_{\text{subfilter fluctuations}}. \quad (4.28)$$

This decomposition assumes that, consistent with (4.26),

$$\hat{\phi}' = 0.$$

Applying this decomposition to the resolved Reynolds stress (4.23) yields:

$$\begin{aligned} \langle \bar{u}_i \bar{u}_j \rangle - \langle \bar{u}_i \rangle \langle \bar{u}_j \rangle &= \langle \hat{u}_i \hat{u}_j \rangle + \langle \hat{u}_i (\bar{u}_j - \hat{u}_j) \rangle \\ &\quad + \langle (\bar{u}_i - \hat{u}_i) \hat{u}_j \rangle + \langle (\bar{u}_i - \hat{u}_i) (\bar{u}_j - \hat{u}_j) \rangle - \langle \hat{u}_i \rangle \langle \hat{u}_j \rangle \\ &= \underbrace{\langle \hat{u}_i \hat{u}_j \rangle - \langle \hat{u}_i \rangle \langle \hat{u}_j \rangle}_{\text{coherent stress}} + \underbrace{\langle (\bar{u}_i - \hat{u}_i) (\bar{u}_j - \hat{u}_j) \rangle}_{\text{incoherent stress}} \end{aligned} \quad (4.29)$$

where the cross terms  $\langle (\bar{u}_i - \hat{u}_i) \hat{u}_j \rangle = 0$  because of the orthogonality of the periodic and non-periodic fluctuations.

### 4.3.3 A Note on Ensemble Averages

Conventionally the ensemble average is defined as an average over a large number of realizations of a turbulent flow. Formally,

$$\lim_{N \rightarrow \infty} \frac{1}{N} \sum_{i=1}^N u^{(i)}(x, t) \quad (4.30)$$

where  $u^{(i)}(x, t)$  is one particular realization. The problem with this definition is that the result strongly depends on what set of realizations the sum is taken over. For experiments, the different realizations are identified with different repetitions of the experiment. From a mathematical point of view, defining the set in this way is highly unsatisfactory. For numerical experiments the problem becomes much clearer. Using deterministic equations each repetition will produce exactly identical results, unless

a perturbation is explicitly applied. In this case, the value of the ensemble average might depend on the set of perturbations chosen.

A more formally rigorous definition of the ensemble average can be formulated as follows. Denote by  $u(t|u_0, t_0)$  the solution at time  $t$  of the Navier-Stokes solved using the initial condition  $u(t_0) = u_0$ . If  $\Omega$  is the space of all possible initial conditions and  $p : \Omega \rightarrow \mathbb{R}$  is a probability density function that identifies a particular set of initial conditions, the ensemble average can be expressed as

$$\langle u(x, t) \rangle = \int_{\Omega} u(x, t|v, t_0) p(v) dv. \quad (4.31)$$

Note that, under either definition, the ensemble average is still potentially a space and time dependent field.

To illustrate why this is important, consider a flow dominated by a periodic component, such as the shedding of the turbulent separation bubble. If the ensemble is chosen so that the initial instant always corresponds to the same phase in the shedding cycle, the resulting ensemble average will be equivalent to a phase average. If, however, the phases at the initial instant are random, the result will be equivalent to a time average. This has important consequences for modeling. Additionally, when invoking the ergodic theorem to identify the ensemble average with a homogeneous space or time average, it is important to consider exactly which ensemble is being employed, and whether ergodicity can be applied to that particular ensemble.



## Chapter 5

### RESULTS I: LAMINAR SIMULATIONS

In preparation for the turbulent simulations laminar flow for a similar geometry was investigated. These laminar simulations serve two purposes. The first is to help understand the extent to which the large structures in the flow and the physical mechanisms of flow control are the same for the laminar and turbulent flow. Second, the results for the laminar calculations are of practical importance for many applications where the flow remains laminar, such as Micro Aerial Vehicles (MAVs).

The laminar calculations used the earlier experimental geometry of Seifert and Pack (1999). As can be seen in figure 1.2, the two profiles are almost identical. (Note that Seifert and Pack used a slightly different length scale, the geometry has been rescaled to conform to the normalization used in the CFDVal Workshop.) Experimental results for the turbulent flow over the two profiles showed little significant difference between the experiments except for the strength of the suction peak, which can be attributed to a difference in the tunnel blockage ratio for the two experiments (Greenblatt et al., 2004). For the Seifert and Pack experiments the “hump” was mounted on the tunnel side wall, and the computational geometry includes the entire tunnel width. The hyper-stretched region extends from  $x/c = 3$  to  $x/c = 14$  and all cases are computed in two-dimensions. A longer slot was used than in the experiments, the slot extends from  $x/c = 0.45 - 0.65$ . This slot length was chosen to be one-quarter of the wavelength associated with the natural shedding frequency in order to optimize the receptivity of the flow according to linear stability theory. The Reynolds number based on chord is  $Re_c = 10^4$ , and the Mach number is  $Ma = 0.25$ .

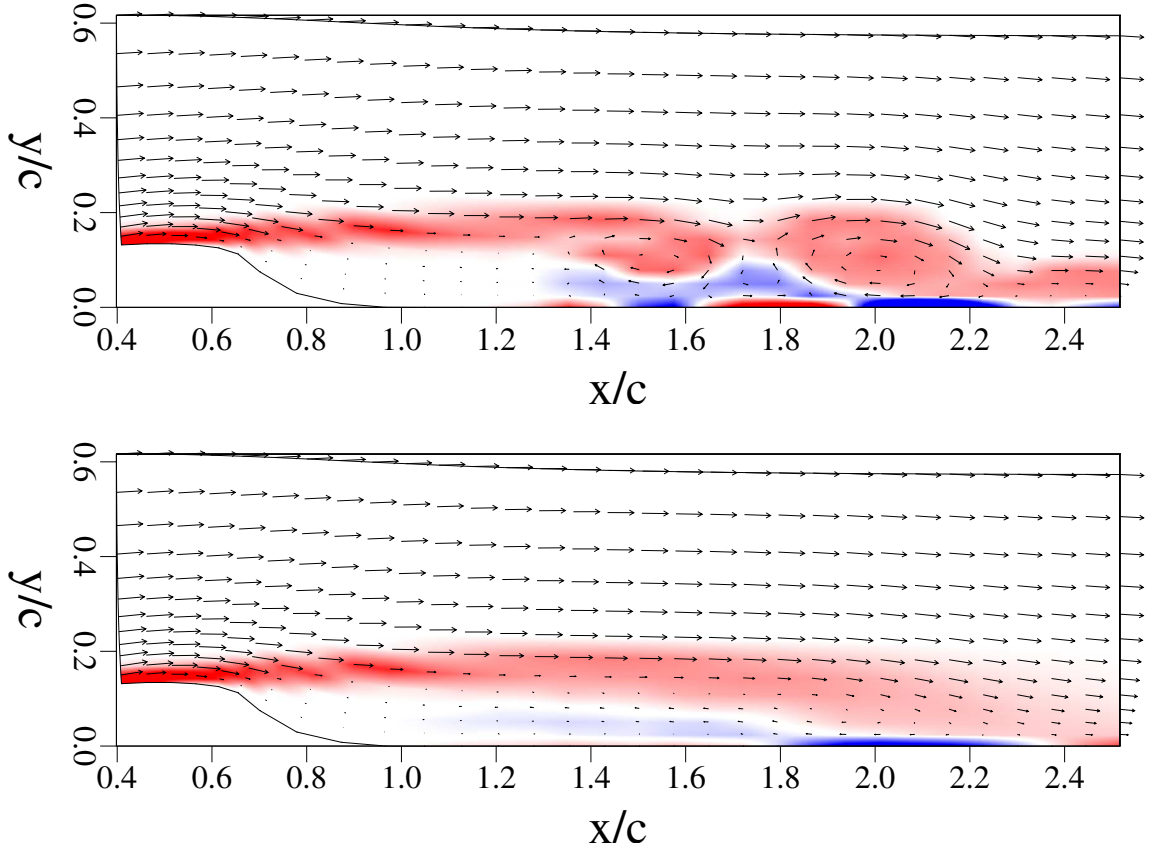


FIGURE 5.1. Instantaneous (top) and mean (bottom) velocity vectors and contours of spanwise vorticity for the baseline (unforced) flow

## 5.1 Baseline Case

Figure 5.1 shows the instantaneous and mean flow fields for the flow without any control. In the experiments the flow was turbulent and the mean separation location was at the sharp corner ( $x/c = 0.66$ ). For the laminar calculations the unsteady separation initially appears at the corner but since laminar flows are less resistant to separation the separation point moves upstream to a mean location of  $x/c \approx 0.57$ . For the unforced case we observe “massive” separation over the rear of the hump, with a “dead” region of quiescent fluid extending over most of the ramp and downstream to almost  $x/c = 1.3$ . Initially, the formation and shedding of large structures occurs

over the ramp between  $x/c = 0.66 - 1.0$ , however, the “dead” region grows as the simulation progresses, and the location at which the large structures begin to form moves downstream, extending from  $x/c = 1.4 - 2.2$ . Mean reattachment occurs at  $x_{\text{reattach}}/c = 2.36$ .

The unsteady pressure data from the simulation were averaged in time to obtain a streamwise distribution of  $C_p$  (shown in figure 5.3 by the solid line). The flow experiences a sharp pressure drop as it accelerates over the front side of the airfoil, with a peak at  $x/c \approx 0.4$ . A pressure plateau develops extending over most of the length of the separation region. Near the reattachment point there is a small pressure increase. This peak is also observed near the reattachment point for other reattachment geometries (such as the backward facing step) and is caused by the streamline curvature as the flow turns parallel to the wall.

Examination of the flow field over a large number of shedding cycles shows a long time drift of the location of the “mean” reattachment point. This drift is associated with variations in the size of the “dead” region over long time scales.

Much of the literature, particularly the results of Seifert and Pack (1999) report frequency information in terms of a reduced frequency scaled by the bubble length,  $F^+ = fl_{\text{sep}}/U_\infty$ , where  $f$  is the dimensional frequency and  $l_{\text{sep}}$  is the length of the separation bubble. While arguably useful for comparison of different geometries and parameters, this scaling is problematic for three reasons. First, the unforced bubble length is difficult to determine with accuracy. (In fact, Seifert and Pack (1999) report  $l_{\text{sep}}/c = 0.57 \pm 0.03$ , but they use a value of  $c/2$  for scaling their reduced frequencies.) In addition to the long time-scale drift of the bubble length, which we observe, it is also difficult or impossible to measure the reattachment location directly in an experiment. Second, for each forcing case the bubble length changes, so to maintain a physically relevant length scale, one ought to scale the frequency with the separation length corresponding to that particular forcing case. However, since the bubble length is a function of amplitude as well as frequency, this would mean that our reduced

frequency would change if we performed an amplitude response study. Finally, while it seems dimensionally correct to assume that the relevant scaling parameter is some length scale associated with the bubble, it is not clear that the bubble height, for example, is not the correct scaling. In fact, we might argue that while for an absolute instability the convective time-scale of the bubble is the relevant parameter (and therefore the correct length scale is  $l_{\text{sep}}$ ), for a convectively unstable bubble, or for a flow which has been attached by the successful application of active flow control, we are interested in the local instability modes which should scale on a wall normal length scale, such as the bubble height or boundary layer thickness.

For these reasons, in this section frequency data is scaled by the natural shedding frequency, except where other units are noted for reference purposes. For the unforced case the dominant shedding frequency is  $F_0 = 0.565$  non-dimensionalized by chord and free-stream velocity, which would correspond to a reduced frequency of  $F_0^+ = 1.3$  when scaled by bubble length.

## 5.2 Periodic Forcing

For the oscillatory case the forcing amplitude is characterized by the oscillatory momentum coefficient,

$$\langle c_\mu \rangle = \frac{2b}{c} \frac{\langle \rho U_{\text{jet}}^2 \rangle}{\rho_\infty U_\infty^2},$$

where  $b$  is the slot width and  $c$  is the chord.

### 5.2.1 Effect of Amplitude

At first, forcing was applied with the natural shedding frequency for a wide range of amplitudes. The forcing was accomplished by means of wall normal blowing and suction. Figure 5.2 shows the variation in the reattachment location with forcing amplitude, the reattachment location for the unforced case is indicated by a dashed line.

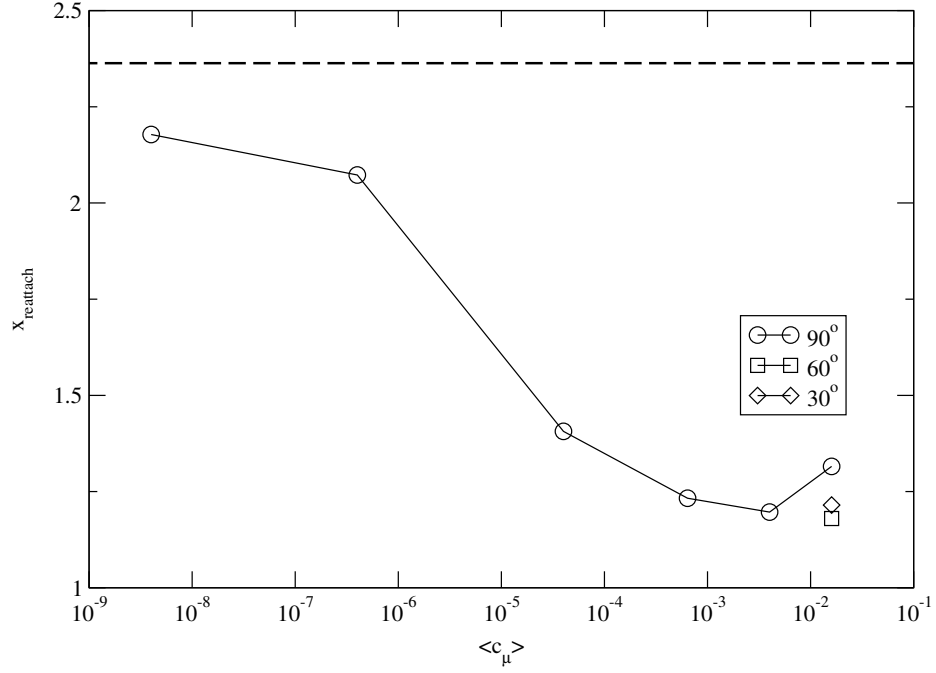


FIGURE 5.2. Reattachment location as a function of forcing amplitude,  $f = 0.565$ . The horizontal dashed line shows the reattachment point for the unforced case, and the symbols indicate the jet angle.

For amplitudes as low as  $U_j/U_\infty = 0.0001$  ( $\langle c_\mu \rangle \approx 4 \times 10^{-9}$ ) the “dead” region is significantly shortened. The forcing becomes dramatically more effective for  $\langle c_\mu \rangle > 0.004\%$  and the effect begins to saturate for  $\langle c_\mu \rangle \sim 0.1\%$ . At  $\langle c_\mu \rangle \sim 1.6\%$  the reattachment length actually begins to increase again. This is apparently due to the wall normal forcing, which penetrates the approach boundary layer completely when applied at this amplitude. As a result the forcing becomes less effective. Additional calculations performed at shallower blowing angles result in better performance (figure 5.2).

While it is not possible to completely reattach the flow, reductions of as much as 65% in the length of the separated region are seen. The LaRC experiments required larger forcing amplitudes to affect the flow. Seifert and Pack (1999) report a level of  $\langle c_\mu \rangle > 0.03\%$  to see a significant change in the mean flow. This may be due to the stronger coherence of the large structures in the laminar case which makes them more

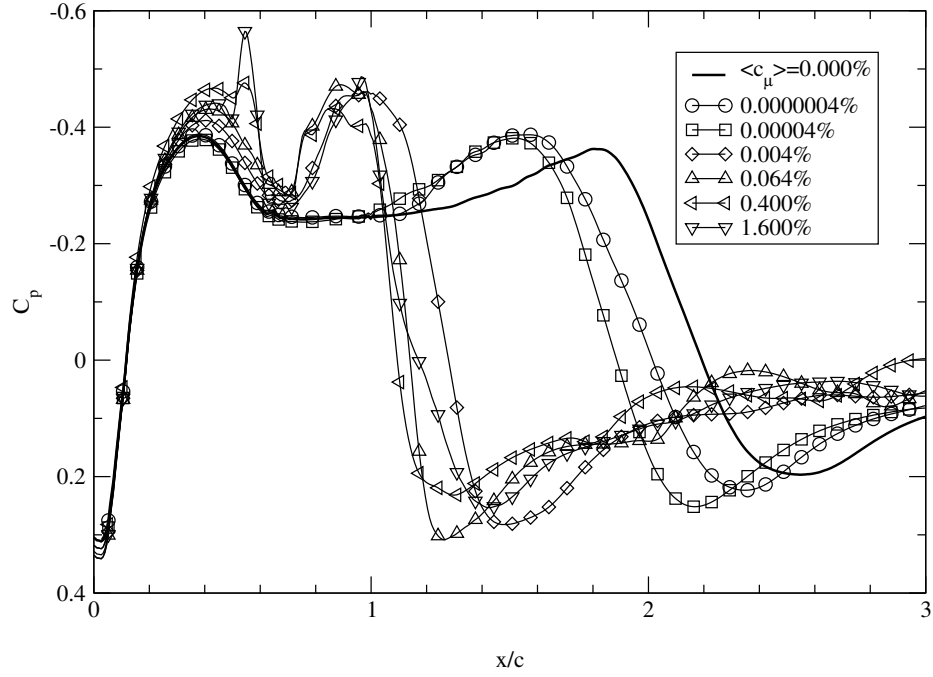


FIGURE 5.3. Effect of forcing on the downstream distribution of  $C_p$  for various forcing amplitudes,  $f = 0.565$ .

receptive to periodic forcing. A lower level of background noise in the simulations may also be a factor.

Figure 5.3 shows the effect of forcing on  $C_p$  for a range of forcing amplitudes at a fixed frequency of  $f = F_0$ , which is the natural shedding frequency. As the forcing amplitude increases, the pressure recovery begins earlier. The higher peak near the reattachment point can be attributed to the sharper curvature of the streamlines due to the shorter separation bubble. The location of the pressure peak is at  $\sim 75\% x_{\text{reattach}}$ .

Figure 5.4 shows the downstream development of the amplitude of the temporal Fourier mode associated with the forcing frequency when the flow is forced at the natural shedding frequency. For small amplitude forcing there is little change from the unforced case. At larger forcing amplitudes, the region of disturbance growth begins further upstream. This, in turn, leads to earlier non-linear saturation. The

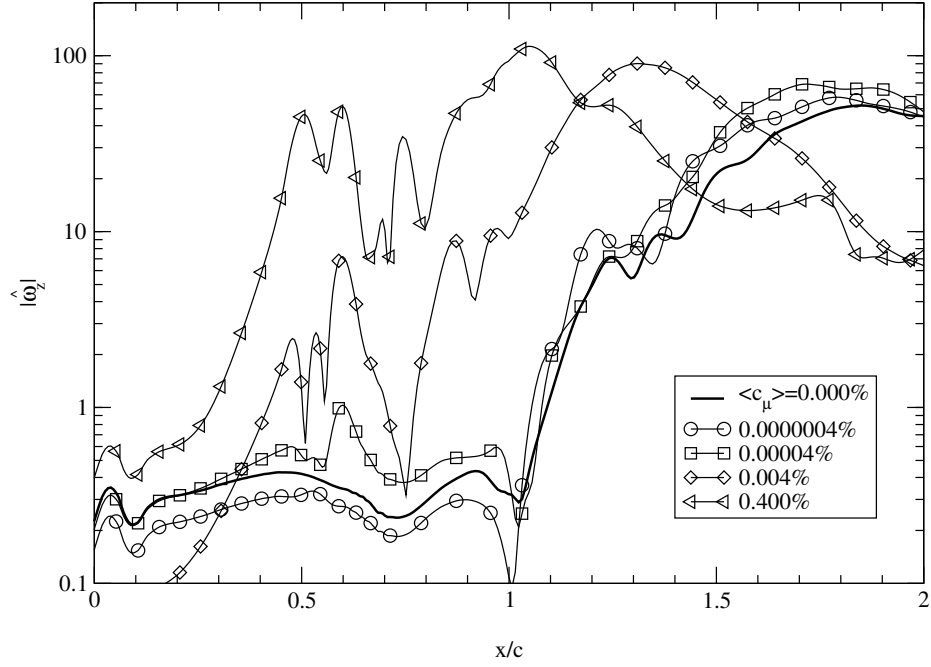


FIGURE 5.4. Downstream evolution of the Fourier amplitude of the response to the forcing frequency,  $f = 0.565$ .

saturation peak for all forcing amplitudes is between  $80 - 90\% x_{\text{reattach}}$ .

Examining the phase speed (figure 5.5) we find that upstream of the reattachment location the phase speed is  $0.24 - 0.35$ . Slightly past the reattachment location the phase speed shows an increase to  $0.71$ . An inspection of the unsteady flow field shows that the structures initially form in the slow moving stagnant region close to the wall and then accelerate as they lift away towards the faster outer part of the boundary layer.

### 5.2.2 Effect of Frequency

A series of simulations were run over a range of forcing frequencies at several amplitudes. In order to eliminate any hysteresis effects, all simulations were initialized with the long-time converged unforced state. The size of the separated region is re-

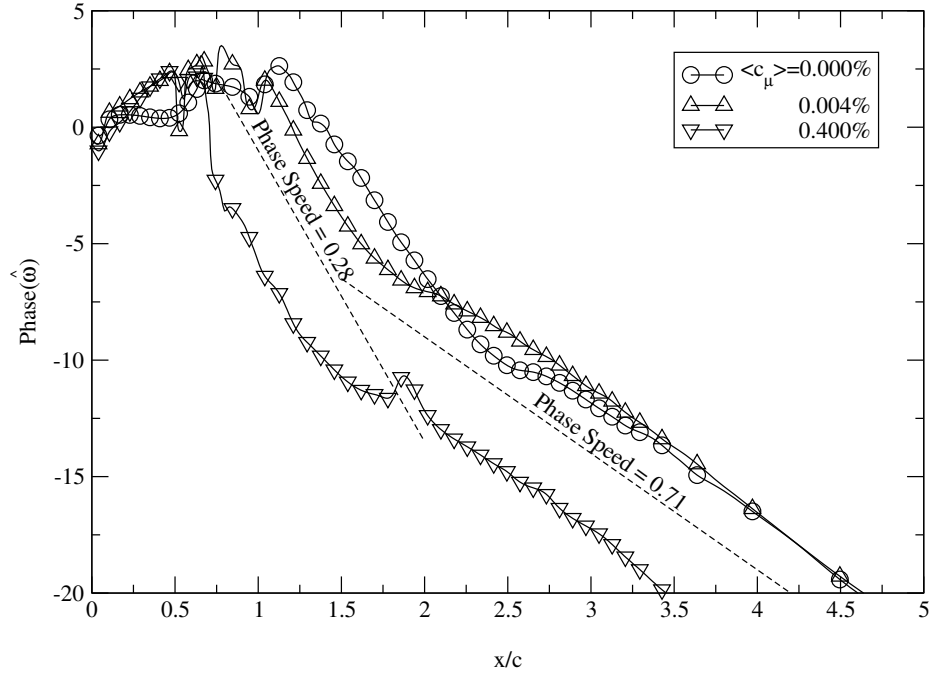


FIGURE 5.5. Downstream evolution of the Fourier phase for the frequency  $f = 0.565$ . Best fit slopes are given for reference.

duced to some extent for all the cases. Since the forced flow has a shorter separation length, we expect that the most effective forcing frequency will actually be somewhat higher than the natural shedding frequency. In fact, the optimal forcing frequency is at  $f = 1.2F_0 = 0.678$ , which corresponds to  $F^+ = 1.6$  when scaled by separation length. It is interesting to note that this agrees with the value observed by Pack and Seifert (2000), even though the flow in the experiments was turbulent and at a much higher Reynolds number. The downstream profiles of the pressure coefficient for the various forcing cases are shown in figure 5.7. For shorter bubbles the pressure peak at reattachment is higher, as we saw in section 5.2.1.

For the lowest forcing amplitude,  $\langle c_\mu \rangle \approx 0.004\%$ , the receptive region is restricted to frequencies near  $1.2F_0$ . At a slightly higher forcing amplitude,  $\langle c_\mu \rangle \approx 0.064\%$ , we see a much broader range of receptive frequencies.

A closer examination of the most effective forcing amplitude,  $\langle c_\mu \rangle \approx 0.064\%$ ,



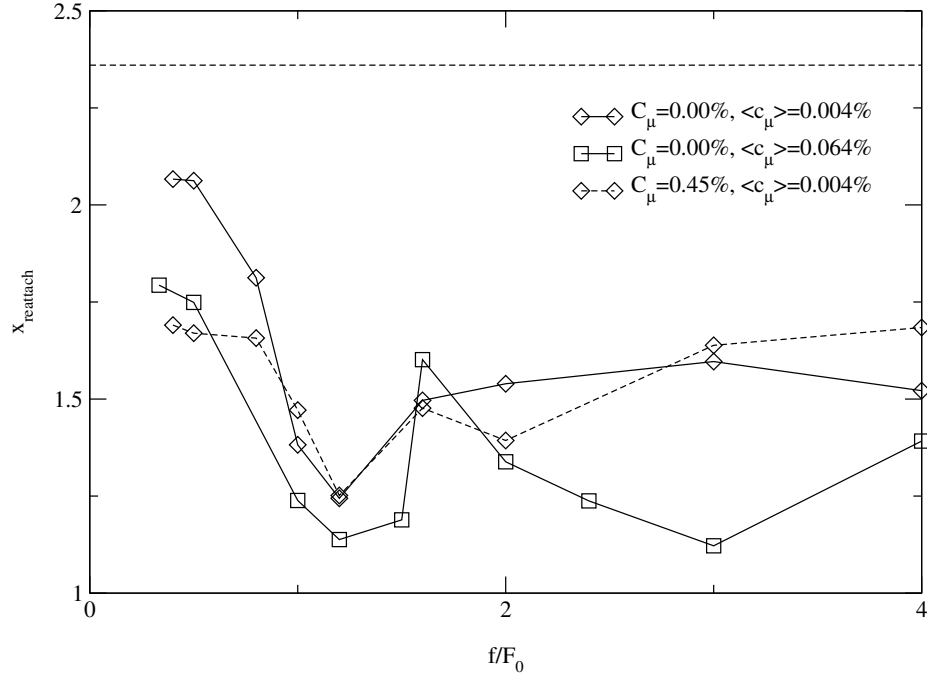


FIGURE 5.6. Effect of forcing frequency on reattachment location for various forcing amplitudes. The dashed curve is for the suction case (section 5.3). The horizontal dashed line shows the reattachment location for the unforced case.

reveals that the bubble wants to respond within a fixed frequency range regardless of the forcing frequency. For frequencies near  $1.2F_0$  the bubble shedding frequency locks in to the forcing frequency. However, for frequencies above a critical value of approximately  $f > 1.6F_0$ , we see vortex merging and the shedding locks in to the subharmonic of the forcing frequency. At  $4F_0$  there are two mergings and the shedding locks in to the second subharmonic. At still higher frequencies no vortex mergings are visible and the effectiveness of the forcing is reduced. The vortex merging can be seen by examining the downstream evolution of the frequency response for three representative forcing frequencies as shown in figure 5.8.

The anomalously long reattachment length for the case  $f = 1.6F_0$  (figure 5.6) can be understood by examining a time trace of the wall vorticity at the station  $x/c = 1.35$  (figure 5.9). At this forcing frequency the flow is unable to lock in to

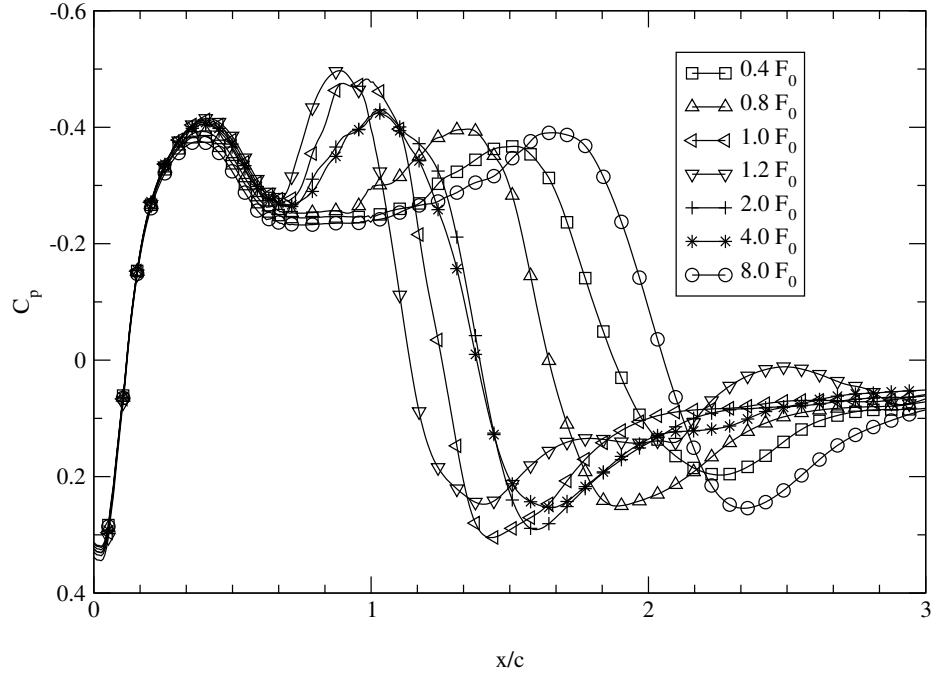


FIGURE 5.7. Effect of forcing on the downstream distribution of for a range of frequencies,  $\langle c_\mu \rangle = 0.004\%$ .

a single frequency. Instead it responds part of the time at the forcing frequency, shedding at  $1.6F_0$ , and part of the time responds at the subharmonic by a process of vortex merging. As a result the forcing is less effective than it would be if the flow could lock into either of these frequencies.

### 5.3 Suction

Greenblatt and Wygnanski (2000) present results showing that once the flow is attached, additional bubble reduction can be obtained by gradually increasing the forcing frequency. This indicates that the problem of keeping a flow optimally attached requires higher frequencies than necessary for attaching a separated flow. This can be explained by the different stability characteristics of the mean attached and mean separated flows. In order to examine this, steady suction was applied to attach the

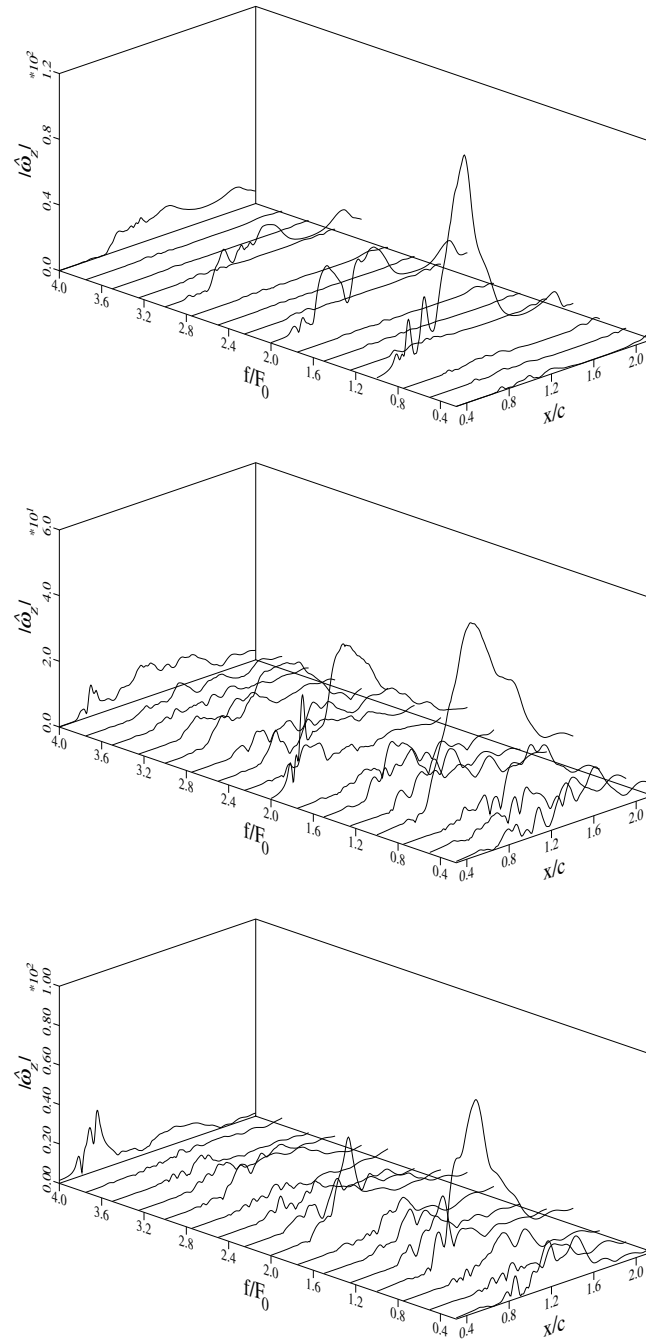


FIGURE 5.8. Downstream evolution of the frequency response for a forcing frequency of  $F_0$  (top),  $2F_0$  (center), and  $4F_0$  (bottom), at  $\langle c_\mu \rangle \approx 0.064\%$ .

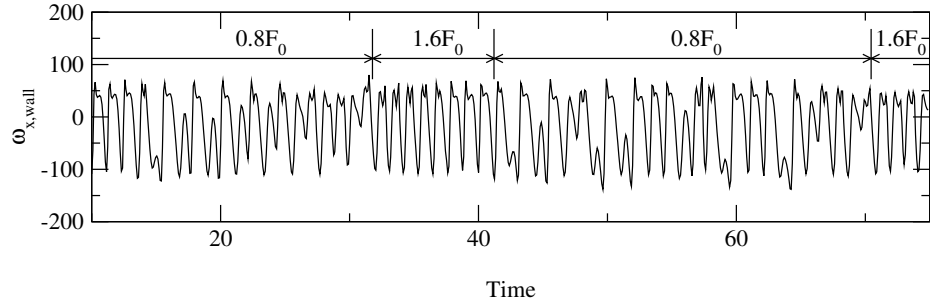


FIGURE 5.9. Time evolution of the wall vorticity at  $x/c = 1.35$  for the forcing frequency  $1.6F_0$  at  $\langle c_\mu \rangle \approx 0.064\%$ .

flow, and then the response of the attached flow to forcing was investigated.

The unforced flow was attached using steady suction with  $c_\mu = 0.45\%$ . The suction was applied across a slot that extends over the sharp corner ( $x/c = 0.59 - 0.69$ ). The resulting mean flow is almost completely attached, with the exception of a shallow separation bubble extending from  $x/c = 0.7 - 0.9$ . This bubble also exhibits periodic shedding with a frequency of  $f = 1.25$ . The shedding is much more strongly periodic than that of the unforced flow without suction and is at a much lower amplitude.

Taking the flow which had been attached by steady suction as an initial condition, forcing was applied to the flow over a range of frequencies. For each frequency, the calculation was started with the steady suction turned on and the flow field converged. The forcing was then applied for several periods to allow the transient associated with the start up of the forcing to convect out of the computational domain. After a periodic state was reached, the suction was gradually reduced to zero. The reattachment location as a function of forcing frequency is shown by the dashed line in figure 5.6. Near the natural frequency of the unforced flow with zero suction the suction has little effect. However, near  $2F_0$  the suction case with an amplitude of  $\langle c_\mu \rangle \approx 0.004\%$  gives a bubble size close to that of the case with  $\langle c_\mu \rangle \approx 0.064\%$  applied to the zero suction unattached profile. This suggests a bi-stable state in which the lower amplitude is enough to maintain the shorter bubble, but to shorten the large

unforced bubble requires a larger forcing amplitude. The fact that the suction profile is more receptive to  $2F_0$  is consistent with the fact that  $2F_0$  is close to the natural shedding frequency for the flow when suction is applied.

## 5.4 Summary

Simulations have been conducted for active control of separation behind a “hump” geometry. The laminar calculations showed a much longer mean separation length than the turbulent experiments. However, when frequencies are rescaled based on the mean separation length, optimal forcing frequencies similar to those in the experiments were found. The amplitudes necessary for the forcing to be effective were significantly lower for our laminar simulations. In addition, at moderate forcing amplitudes, the flow was found to be receptive to higher frequency forcing as well. In these cases vortex merging was observed.

## Chapter 6

### RESULTS II: NASA WORKSHOP SIMULATIONS

The workshop experiments are described in Greenblatt et al. (2004, 2005), with additional details given on the NASA website. The model was designed to replicate the profile of the Seifert & Pack experiments, with the size scaled up by a factor of two. Figure 1.2 shows the profiles for the two models based on QA data; they are very close although not quite identical. The primary difference is in the slot region (figure 1.2, inset); the slot for the workshop experiments is approximately half as wide.

The experiments were performed in the Langley 20"  $\times$  28" shear flow tunnel. The model was mounted on a splitter plate with the leading edge of the plate 1935mm upstream of the leading edge of the model. (In the Seifert and Pack experiments the model was mounted flush with the wind tunnel wall.) In order to reduce the effect of circulation around the splitter plate, a 95mm trailing edge flap was placed at the trailing edge of the plate and deflected 24°. The distance between the plate and the upper wall of the wind tunnel was 382mm. End-plates were placed on either side of the model, 584mm apart. The plates were intended to ensure two dimensionality of the flow, however it was found that the blockage due to the end-plates presented a difficulty for simulations which assumed a purely two-dimensional flow.

Suction was produced by a vacuum pump attached to the plenum through a manifold and flexible tubing. For oscillatory forcing a rigid piston assembly was mounted at the base of the plenum and was activated by six voice-coils. The forcing was calibrated for both a quiescent tunnel as well as with the tunnel on. Changing from the suction manifold to the unsteady actuator reduced the boundary layer thickness by about 20%, however this had a negligible change on the baseline experimental results, and the same inflow conditions were used for all the simulations.

Although several investigators have suggested that it is necessary to model the flow in the plenum in order to obtain accurate results for this geometry, the workshop results do not seem to support this contention (Rumsey et al., 2004). Clearly it is of significant practical benefit if the flow can be predicted with reasonable accuracy without computing the flow in the plenum. Consequently it was decided that this approach should be used here.

The available experimental data includes measurements of the flow near the slot exit. The significant unknowns are the profile of the flow across the slot and the angle at which the flow exits the slot. The current investigations proceeded on the assumption that the local details of the flow near the slot could be rather coarsely resolved, and, in fact a minimal number of grid points were used in this region. Consistent with this the details of the profile across the slot was deemed relatively unimportant and it was modeled with a top hat profile. The flow angle is potentially a more sensitive parameter since it determines the direction of the streamlines near the slot.

The experiments for the NASA Langley CFD Validation Workshop consisted of three cases, a baseline unforced case, flow subjected to steady suction, and flow with periodic zero-mass flux oscillatory forcing. In the current work the FSM was validated against all three cases, but detailed investigations were conducted only for the oscillatory case. Two primary considerations dictated this choice. First, since the unforced bubble is known to be extremely sensitive to low amplitude forcing, discrepancies in the spectra of the background noise for the experiments and the computations might strongly affect the results for the unforced case. Second, the imposed frequency in the oscillatory case makes additional flow diagnostic tools available; in particular it becomes possible to examine the behavior of the large structures by examining phase averaged data. Additionally, in the steady suction case large scale structures seem to play a much reduced role, which makes it a poor choice for evaluating the FSM.

For the FSM calculations a steady RANS turbulent profile is imposed at the in-

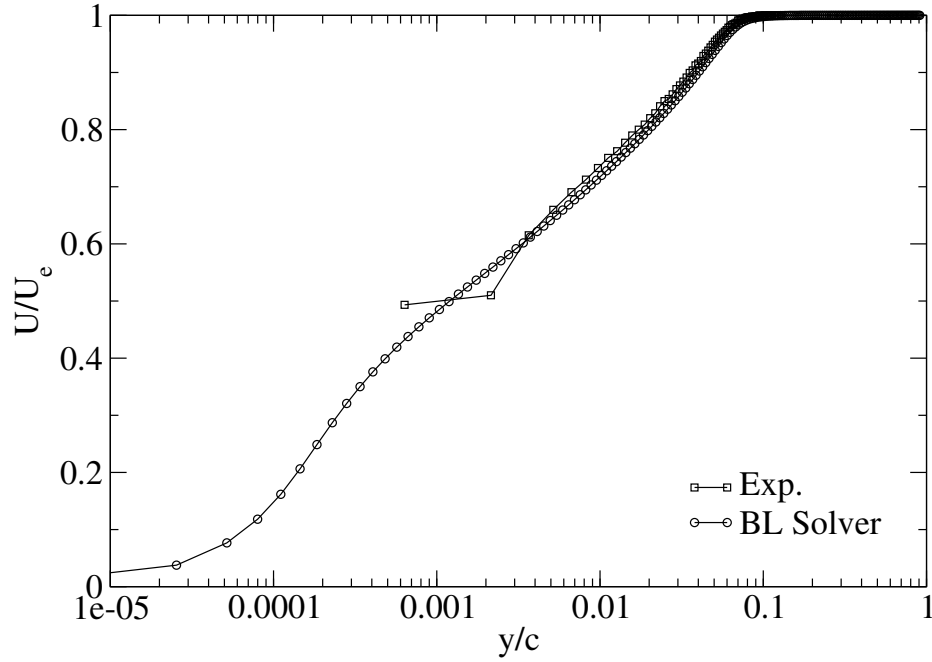


FIGURE 6.1. Boundary layer profile at  $x/c = -2.14$  as predicted by the turbulent boundary layer solver compared to uncorrected Pitot tube measurements from the experiment.

flow boundary. In order to allow upstream pressure disturbances to exit the domain, density, velocity,  $k$ , and  $\varepsilon$  are set to fixed values, and the pressure is extrapolated from the interior. In the computational domain the approach boundary layer remains steady up to the separation location, thus the FSM behaves as a RANS model in this region. Only after separation are unsteady structures allowed to develop in the separating shear layer. The inflow profile is generated by using a stand alone turbulent boundary layer solver for the standard  $k - \varepsilon$  model as described in appendix B.2, with the leading edge placed the same distance upstream of the inflow boundary as in the experiments. Figure 6.1 shows a comparison between the experimentally measured and computationally predicted boundary layers at a representative upstream station. The experimental data is uncorrected Pitot tube measurements; the difficulty measuring near the wall explains the two anomalous points in the figure.



## 6.1 Numerical Convergence

Numerical accuracy of a time-dependent solution produced with an iterative code is controlled by three parameters: the grid spacing, the timestep, and the number of sub-iterations per timestep. Allowing for anisotropic grid refinement increases the number of parameters to five (for structured grids) and evaluating the effect of local grid refinement will further complicate the problem. Although CFL3D is a mature code, and there is significant literature documenting its convergence properties, much of this is for time-steady problems, and none is for the type of hybrid turbulence model that is used here. Since the primary purpose of the current investigations is to evaluate the turbulence model, rather than the code, exhaustive convergence studies were not performed. However, the effect of grid, time step, and number of subiterations was examined for certain representative cases of the oscillatory flow, which should be sufficient to provide confidence in the reported results.

### 6.1.1 Subiterations

In principle, the nominal accuracy of the numerical scheme cannot be recovered unless the implicit solver is allowed to converge to machine precision. In practice the computational cost of completely converging the solver is not justified in terms of the observed improvement in numerical accuracy. Instead the near universal practice is to perform a fixed number of subiterations designed to reduce the residual sufficiently to recover an acceptable level of accuracy. The ideal number of subiterations would minimize overall error of the code for a given amount of computational effort. Generally an efficient compromise value is chosen by monitoring the value of the residual.

When comparing computations performed on different grids, two competing factors affect the rate of convergence. On one hand, convergence tends to be faster on coarser grids. On the other, finer grids may be capable of supporting more multi-grid levels, thereby accelerating convergence. For the current study, three grids were

used, with the two coarser grids created by taking every other point of the next finest grid. The finest grid was therefore capable of supporting two multigrid sub-levels, the medium grid one, and the coarse grid did not support multigrid.

The convergence history for various cases is shown in figure 6.2. For the fine grid (top figure) 10 subiterations per time step is sufficient to reduce the  $L_2$ -norm of the density residual by two orders of magnitude. For the medium grid (middle figure), which only uses one multigrid level, 20 subiterations are required to achieve the same residual. In the coarse grid case (bottom figure), the residual at the first subiteration is approximately an order of magnitude higher than in the two finer grid cases. Although 20 subiterations are sufficient to reduce the residual by two orders of magnitude, it requires 40 subiterations to attain the same residual as achieved using 10 subiterations on the fine grid.

Overall, due to the increased use of multigrid, the finer grids actually converge faster (per subiteration). Nevertheless it should be noted that multigriding significantly increases the computational effort per subiteration. Therefore these results should be viewed with the understanding that the time per subiteration increases much faster than the number of grid points.

For the remainder of this work 10 subiterations were used for the fine and medium grid simulations and 20 subiterations for the coarse grid, except where otherwise noted.

### 6.1.2 Time Step Refinement

In order to assess numerical convergence it is convenient to pick a single figure of merit to quantify the result of each case. The value used here is the coefficient of pressure drag,

$$C_{D_p} = \frac{D_p}{\frac{1}{2}\rho_\infty U_\infty^2 c^2}$$

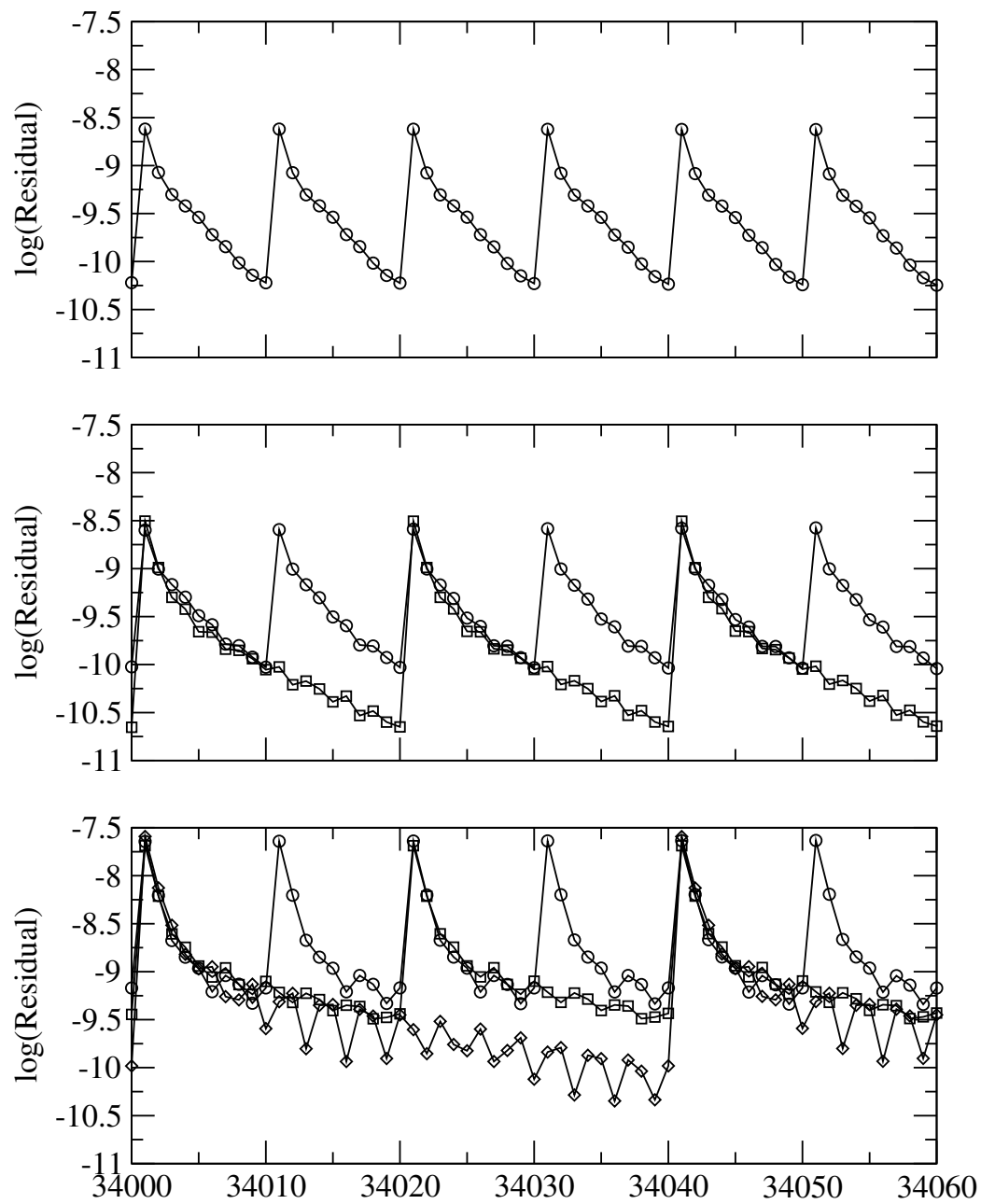


FIGURE 6.2. Convergence history. From top to bottom, fine grid, medium grid, and coarse grid. ( $\circ$ ) 10 subiterations, ( $\square$ ) 20, ( $\diamond$ ) 40.

where

$$D_p = \int \int \langle p \rangle \, dA$$

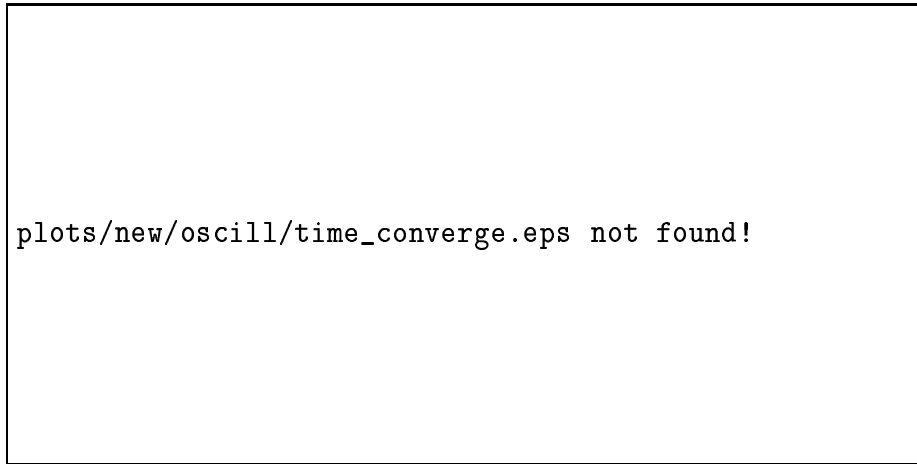


FIGURE 6.3. Time convergence

is the pressure drag, and the integral is over the surface of the “hump.”

Simulations were performed on the medium grid with three different time steps,  $\Delta t = 0.0548$ ,  $0.02974$ , and  $0.01487$  (corresponding to 100, 200, and 400 timesteps per period). The results are shown in figure 6.3. No clear trend is observed. However the results for all time steps are consistent to within the averaging error as indicated by the error bars in the plot (see section 4.2). This suggests that the error due to the time advancement scheme is small relative to the other errors, and the scatter visible in the figure is due to random fluctuations due to the other error terms. Nevertheless, there is still the possibility that the simulation is not fully time step converged. Unfortunately numerical costs preclude further time step refinement. A value of 200 timesteps per iteration was adopted for all remaining calculations in this work.

### 6.1.3 Grid Refinement

As discussed in section 4.1.1, it is vitally important when conducting a grid resolution study that the filter width,  $\delta = \beta\Delta$ , be kept fixed as the grid is refined. In the current case  $\beta = 1$  is used on the coarsest grid, with  $\beta = 2$  and  $4$  on the medium and fine grids

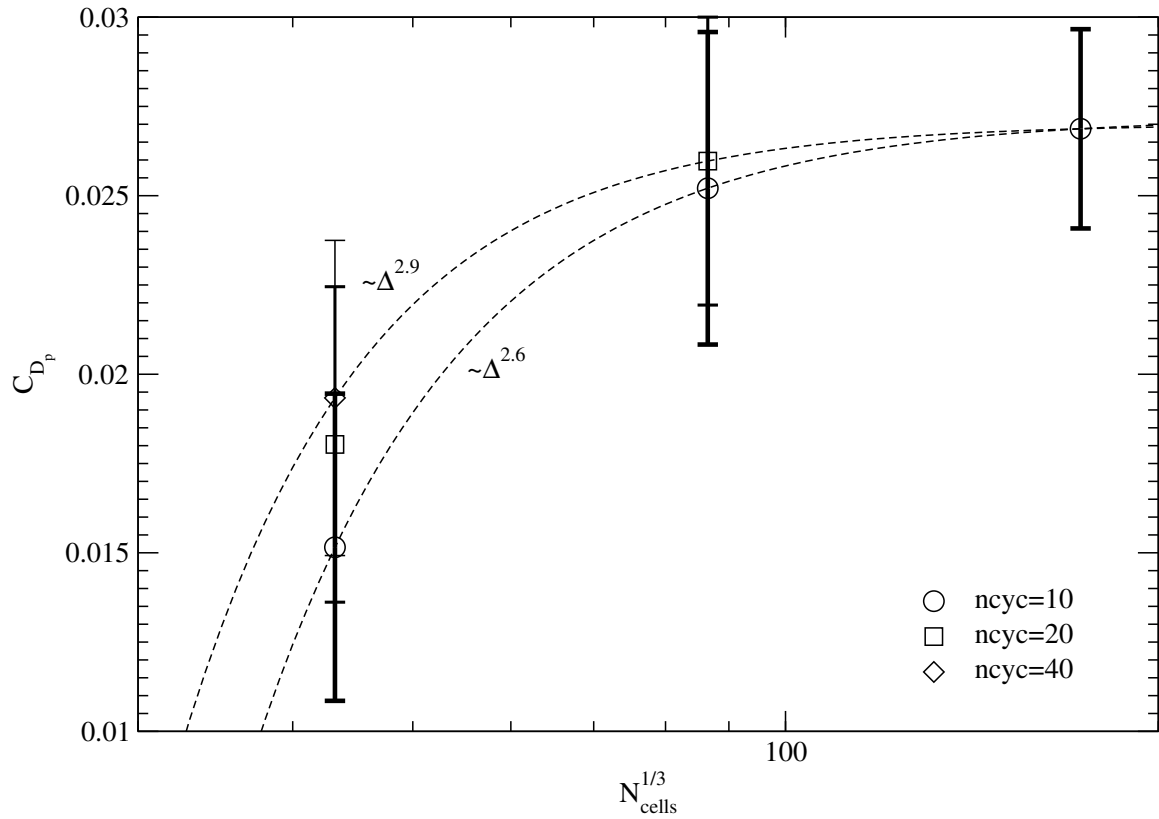


FIGURE 6.4. Grid refinement

respectively. The results are shown in figure 6.4. The symbols indicate the number of subiterations used in each calculation. It is clear that the number of subiterations strongly influences the convergence properties of the scheme. The dashed lines are curve fits to estimate the convergence rate. That the observed convergence appears to be consistently better than second order is presumably explained by the improved convergence on the finer grids. The results further support the idea that it is more computationally efficient to improve the accuracy by refining the grid rather than by increasing the number of subiterations.

## 6.2 Comparison to Experiments

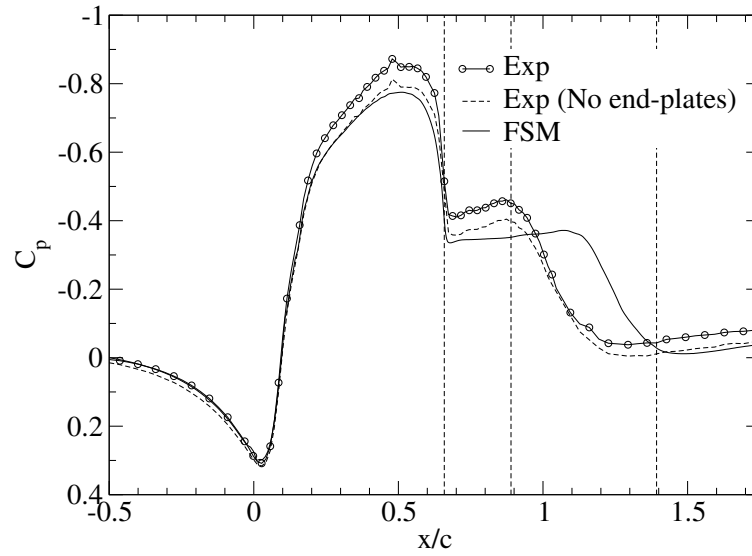
Simulations were run for each of the three Workshop cases. Each was performed on the fine grid, and using a value of  $\beta = 4$  corresponding to approximately four grid points per filter width.

### 6.2.1 Baseline

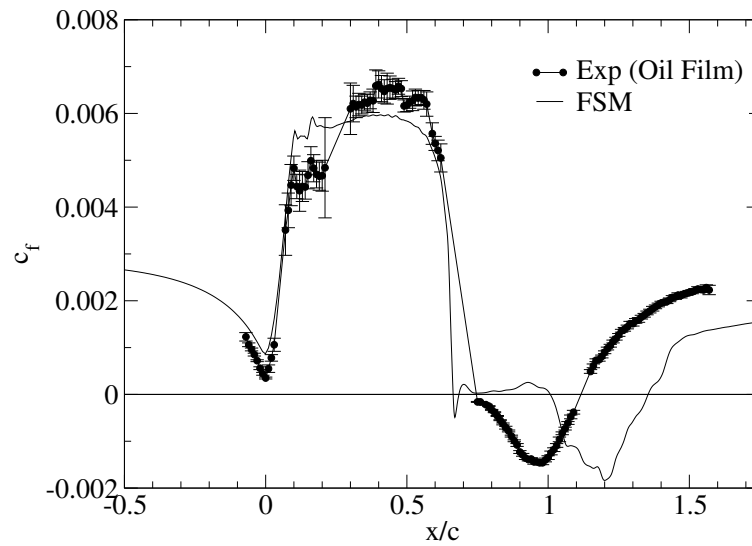
Figure 6.5 shows the downstream variation of the time averaged pressure coefficient and skin-friction coefficient for the unforced flow. The qualitative agreement is good, but the length of the separation is over-predicted by about 50%. This is most likely due to insufficient turbulent mixing in the early part of the bubble where the model transitions from steady to unsteady behavior. This will be further discussed in section 6.3. Another possible factor may be higher levels of background disturbances in the experiments than in the simulations which may be forcing the bubble; certainly for laminar separation we know that the bubble length is quite sensitive to very low amplitude forcing (Israel and Fasel, 2001).

The experimental configuration included end-plates on either side of the “hump.” Although this was intended to aid the match with CFD, by improving the two-dimensionality of the flow, it also introduced additional blockage in the flow over the hump. The difference in the suction peak observed in the experiments and in the simulations is apparently an effect of this blockage. Simulations which model the entire span including the end-plates matched the suction peak correctly (Krishnan et al., 2004). In addition, the experiment was repeated for the unforced case with the end-plates removed. The result without the end-plates is much closer to the CFD prediction (fig. 6.5(a)). Nevertheless, there is still a small mismatch in the suction peak, perhaps due to the blockage from the boundary layers on the side walls of the tunnel itself.

Skin-friction measurements in the experiment were taken using oil film interferom-



(a)



(b)

FIGURE 6.5. Time averaged pressure coefficient (a) and skin-friction coefficient (b) versus downstream distance for the unforced flow. The dashed lines indicate the locations of the spectra in figure 6.7.

etry (Naughton et al., 2004), as shown in figure 6.5(b). The shape of the skin-friction profile after separation is very similar for the experiments and simulations, however

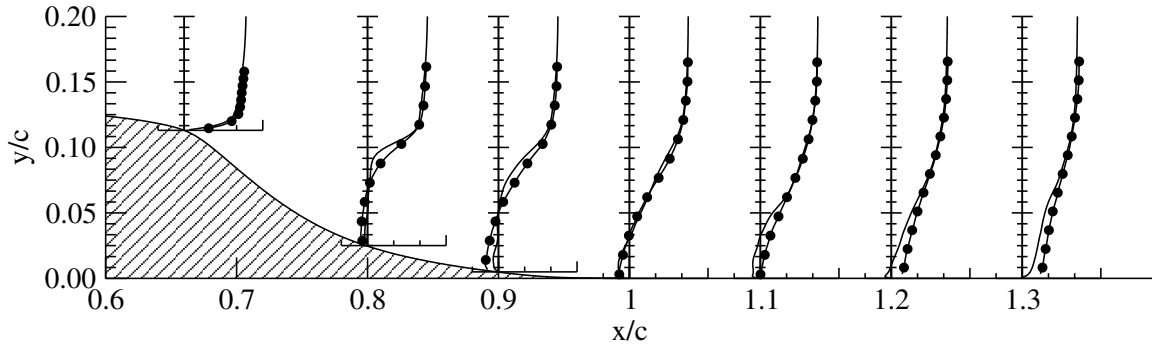


FIGURE 6.6. Profiles of  $u$ -velocity at seven downstream stations for the unforced flow ( $x/c=0.66, 0.8, 0.9, 1.0, 1.1, 1.2$ , and  $1.3$ ). (—) simulations; (●) experiments.

the simulation data is shifted downstream by about 20% chord due to the longer reattachment length. In examining the experimental data for the skin friction it should be noted that it is not possible to take data very near the separation location. Nevertheless, from the shallow slope and negative curvature seen at the first available measurement stations past separation it is possible to infer that there may be a small region of positive skin-friction just past the separation point. This would indicate that a small region of counterclockwise rotating fluid resides inside the clockwise rotating separation bubble, as is seen, albeit with a much greater downstream extent, in the simulations.

The velocity profiles (figure 6.6) also reflect the late reattachment. The very good agreement at separation ( $x/c = 0.66$ ) shows that the EASM model is successful at modeling the approaching boundary layer. Within the bubble the agreement is not as good, with the exception of the profile at  $x/c = 1.0$ , perhaps connected with the fact that near this location both the  $C_p$  and  $c_f$  values for the experiments and simulations agree. As expected the near wall profiles downstream of reattachment are not as full as those measured in the experiments due to the delayed reattachment.

Pressure fluctuation spectra at the wall for three selected downstream locations



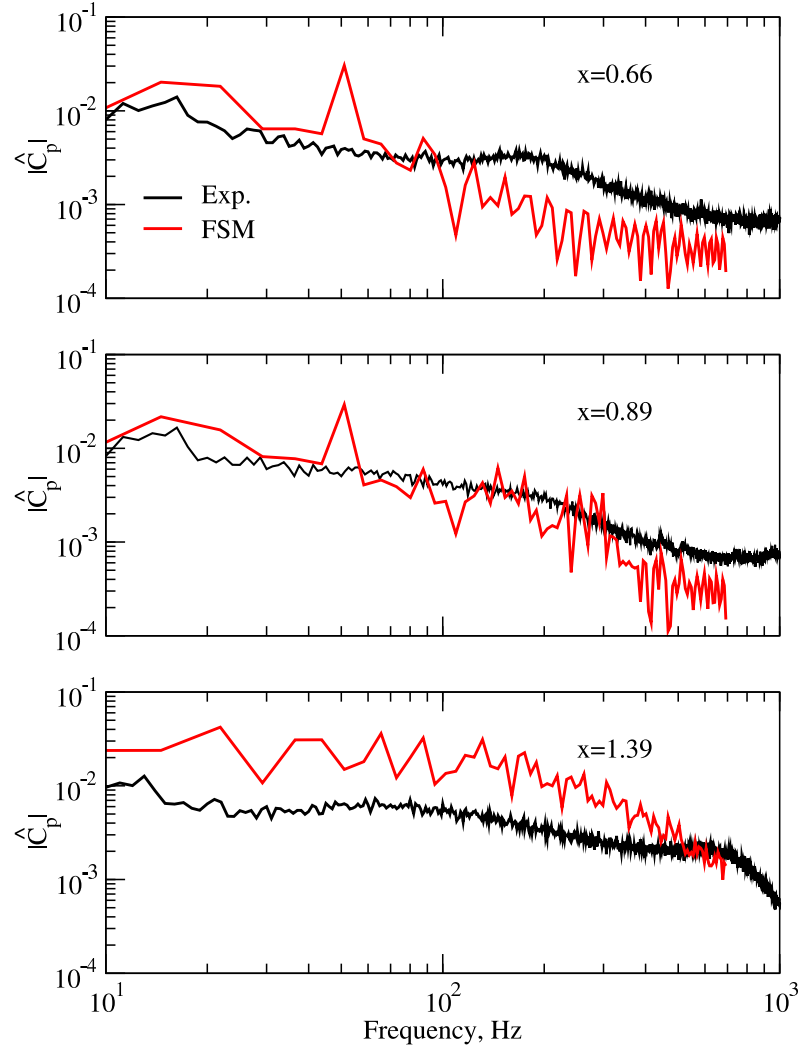


FIGURE 6.7. Wall pressure fluctuation spectra for the unforced flow. The locations of the spectra are indicated in figure 6.5(a) by the dashed lines.

are shown in figure 6.7. The experimental  $C_p$  spectra were computed from the dynamic pressure time-history data at the same locations (Greenblatt et al., 2004). The location of the spectra are indicated by the dashed lines in figure 6.5(a). The envelope of the experimental and computed spectra are similar, however the spectrum for the FSM has a sharp peak at 50 Hz (corresponding to a reduced frequency of  $F^+ \sim 0.3$ ).

Visualization of the instantaneous flow field data shows that this frequency is associated with the natural shedding of large structures observed in the simulations; however it is also present upstream of the “hump.” This upstream traveling acoustic disturbance may indicate a greater degree of coherence for the large scale structures observed in the FSM than for those in the experiment, but the possibility that it is a numerical artifact of feedback between the bubble and the inflow boundary can not be excluded.

Overall, the turbulence model simulations predict approximately the correct intensity for the turbulent fluctuations. However, near the separation location the fluctuation intensity is under-predicted. This may be explained by the nature of the model which transitions from RANS behavior upstream of separation to LES in the separated flow. In the region just downstream of separation the model is still transitioning between RANS and LES, and the turbulent fluctuations have not had sufficient time to grow. After separation, the intensity of the background fluctuations rapidly increases and inside the bubble it matches the experimental values quite well. Downstream of the experimental reattachment point the simulated turbulence level is over-predicted; this is consistent with the later reattachment observed in the simulation.

### 6.2.2 Steady Suction

Preliminary calculations indicated that the effect of steady suction is highly dependent on the angle at which the flow enters the slot. For this reason modeling the slot with a fixed transpiration velocity is not an optimal approach as it requires a fortuitous choice of suction angle. In keeping with the initial hypothesis that the details of the flow inside the slot are not important to the outer flow, a pressure boundary condition was employed. In this approach the pressure along the slot is set to a fixed value, and both the normal and tangential velocity are allowed to develop naturally.

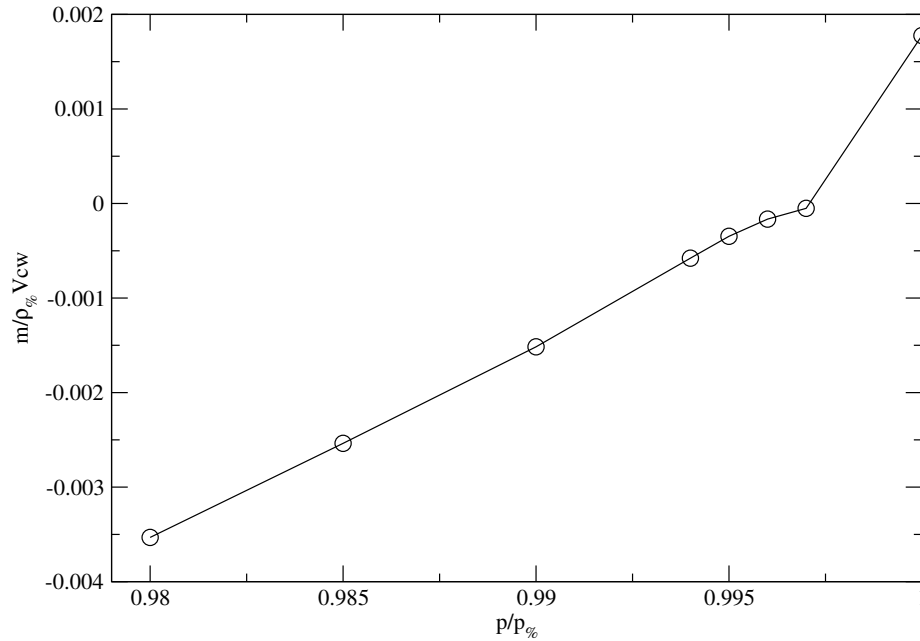


FIGURE 6.8. Mass flow rate as a function of back pressure in the slot

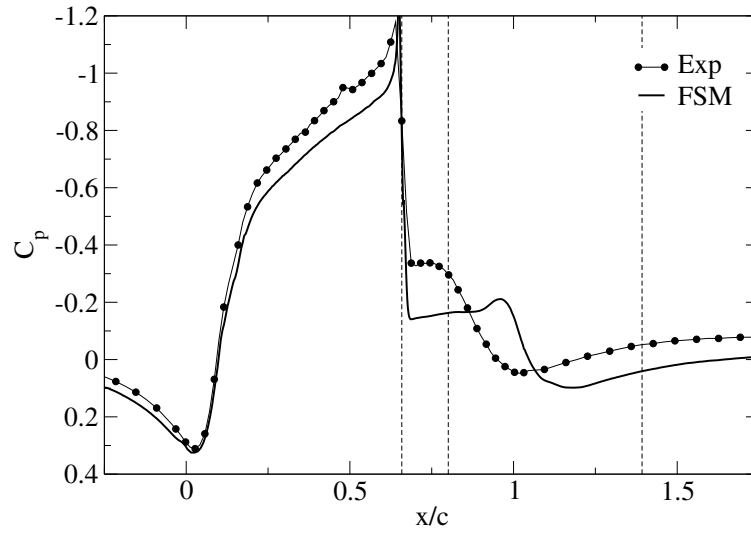
Since the rate of suction affects the global pressure distribution there is no simple way to predict the pressure required to maintain a given flow rate. Instead, a series of short two-dimensional RANS simulations is used to estimate the response of the flow. As CFL3D is a finite-volume code it is reasonable to calibrate flow forcing in terms of the integral quantities (mass and momentum flux) rather than differential quantities (velocities). The normalized mass flow rate per unit chord as a function of back pressure in the slot is shown in figure 6.8. The flow rate for the experiment is

$$\frac{\dot{m}}{\rho_\infty V_{cw}} = \frac{0.1518 \text{ kg/s}}{(1.185 \text{ kg/m}^3)(34.6 \text{ m/s})(0.42 \text{ m})(0.584 \text{ m})} = 1.509 \times 10^{-3}.$$

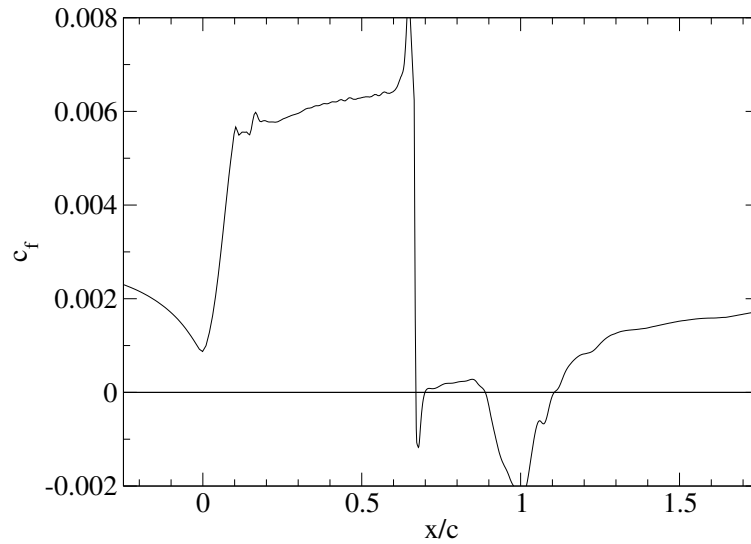
Extrapolating from the plot, this requires a back pressure of

$$\frac{p}{p_\infty} \approx 0.99.$$

For this case the velocity profiles (figure 6.10) also reflect a late reattachment relative to the experimental measurements. The spectrum (figure 6.11) near the



(a)



(b)

FIGURE 6.9. Time averaged pressure coefficient (a) and skin-friction coefficient (b) versus downstream distance for the flow with steady suction. The dashed lines indicate the locations of the spectra in figure 6.11.

separation point slightly under-predicts the intensity of the background turbulence, as in the unforced case. There is not a strong peak in the spectrum, as there was in the unforced case. This is expected since the bubble is much weaker as is the intensity

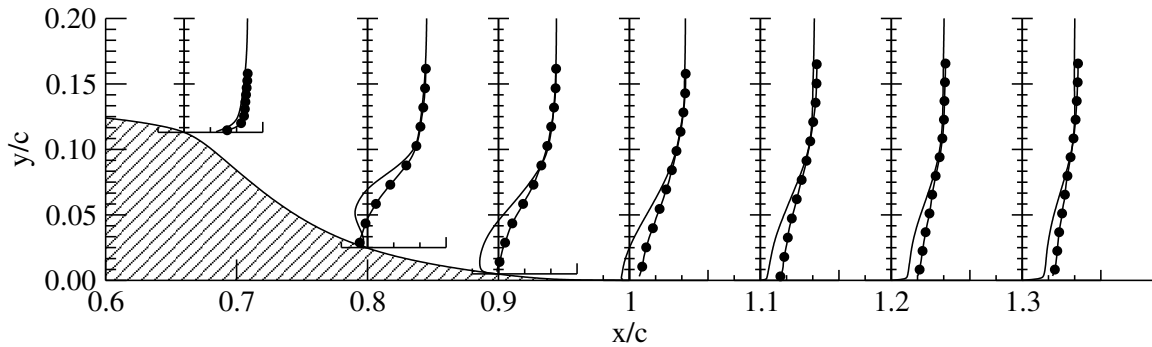


FIGURE 6.10. Profiles of  $u$ -velocity at seven downstream stations for the flow with steady suction ( $x/c=0.66, 0.8, 0.9, 1.0, 1.1, 1.2$ , and  $1.3$ ). (—) simulations; (●) experiments.

of the shedding.

### 6.2.3 Oscillatory Blowing

Oscillatory forcing is imposed by varying the velocity over the slot sinusoidally in time. In the experiment the direction of the flow through the slot will also vary periodically based on the dynamics of the flow near the slot and inside the nozzle. However, we assume that as long as the unsteady forcing excites the unstable shear layer modes the results should be insensitive to the detailed behavior of the flow near the slot. We have found that if the forcing is introduced normal to the boundary layer, then at higher amplitudes the unsteady momentum penetrates the boundary layer completely and is not effective. For this reason, the forcing for this case is introduced at an angle approximately corresponding to the nozzle exit angle of the experimental forcing slot.

The agreement is generally quite good (figure 6.12(a)). The discrepancy in the height of the suction peak is likely due to blockage effects, as in the unforced case, but no experimental data is available for the forced case without the end-plates. The over-prediction of the reattachment length is not due to excessive damping of the

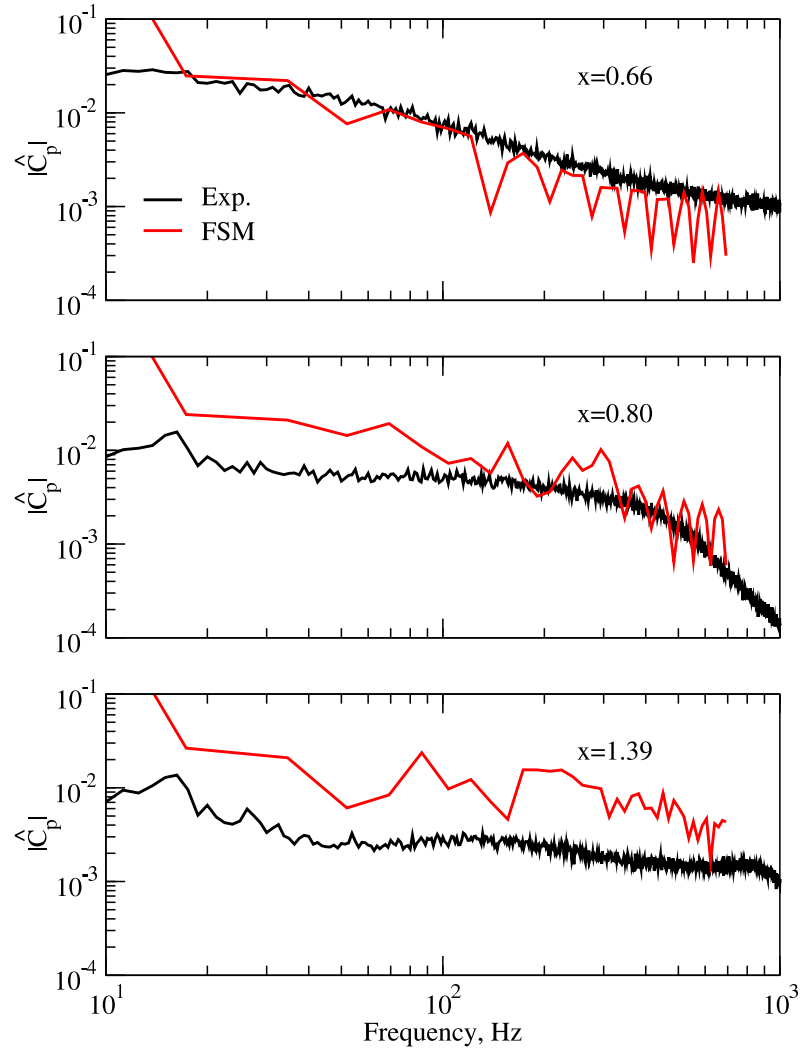
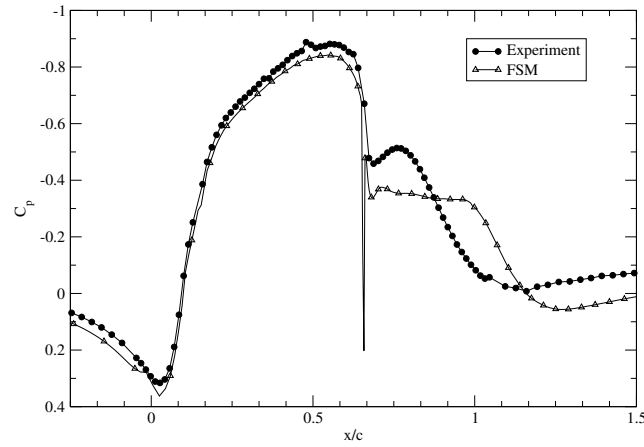
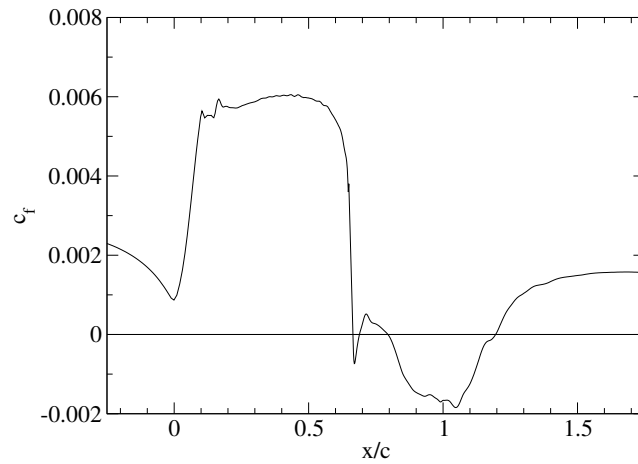


FIGURE 6.11. Wall pressure fluctuation spectra for the flow with steady suction. The locations of the spectra are indicated in figure 6.9(a) by the dashed lines.

structures by the turbulence model, since the results are insensitive to the degree of model contribution (as will be discussed in section 6.3). One possibility is that transition from the RANS region to the LES region occurs slightly too late. Another possibility is that as the contribution function decreases there is a loss of modeled turbulent kinetic energy without an explicit mechanism to transfer that energy back



(a)



(b)

FIGURE 6.12. Time averaged pressure coefficient (a) and skin-friction coefficient (b) versus downstream distance for the flow with oscillatory forcing. The dashed lines indicate the locations of the spectra in figure 6.15.

into unsteady resolved small-scale motions. This means that the initial disturbance level experienced by the shear layer is slightly too low. This may cause a noticeable lag in the amplitude attained by the disturbance waves in the shear layer.

The  $u$ -velocity profiles show a somewhat weaker backflow than observed in the experiments. As in the unforced case, the development of the near wall profile is delayed corresponding to the later reattachment. The action of the forcing in the

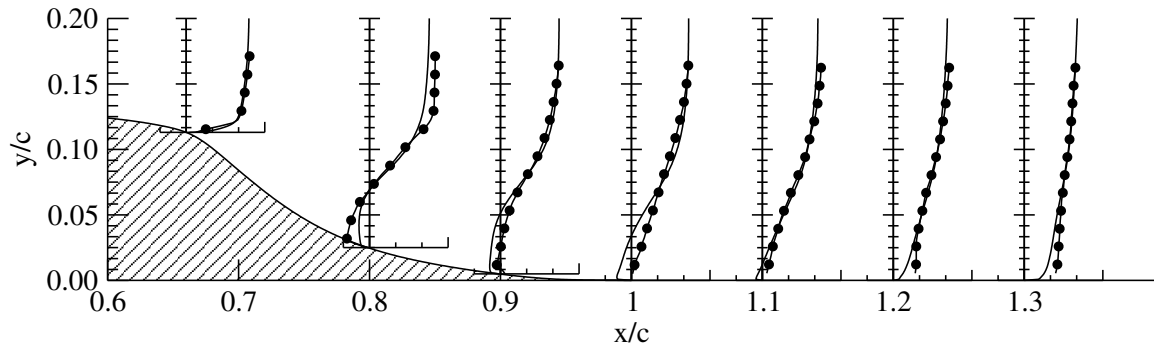


FIGURE 6.13. Profiles of  $u$ -velocity at seven downstream stations for the flow with oscillatory forcing ( $x/c=0.66, 0.8, 0.9, 1.0, 1.1, 1.2$ , and  $1.3$ ). (—) simulations; (●) experiments.

vicinity of the slot can be seen in figure 6.14. At  $\phi = 0$ , which is between the suction and the blowing phase, the shear layer is close to the wall and the separation point is somewhat far downstream. During the blowing cycle, which peaks at  $\phi = 90$  the shear layer is deflected away from the wall and the separation point moves up close to the disturbance slot. As the blowing phase concludes, the flow remains separated near the slot, until the suction phase, which peaks at  $\phi = 270$ , during which the flow begins to turn close to the surface again, and the separation point is pushed far downstream.

The spectra for the wall pressure fluctuations show good agreement for the coherent signal represented by the sharp peaks in figure 6.15. The experimental peaks are hard to see, since they lie right on the numerical data. For the experimental data the even harmonics of the fundamental forcing frequency exhibit a lower envelope than the odd modes, a feature which is not reproduced by the calculations. Other than that, the simulation reproduces the response to the forcing quite well. The background turbulence level is somewhat under-predicted at the first location, again, probably because we are still too close to the RANS region. Also, at this first location the 138.5 Hz peak in the experimental spectrum is slightly broader than seen in the simulation, although by  $x/c = 0.8$  the spectrum from the simulation has broadened



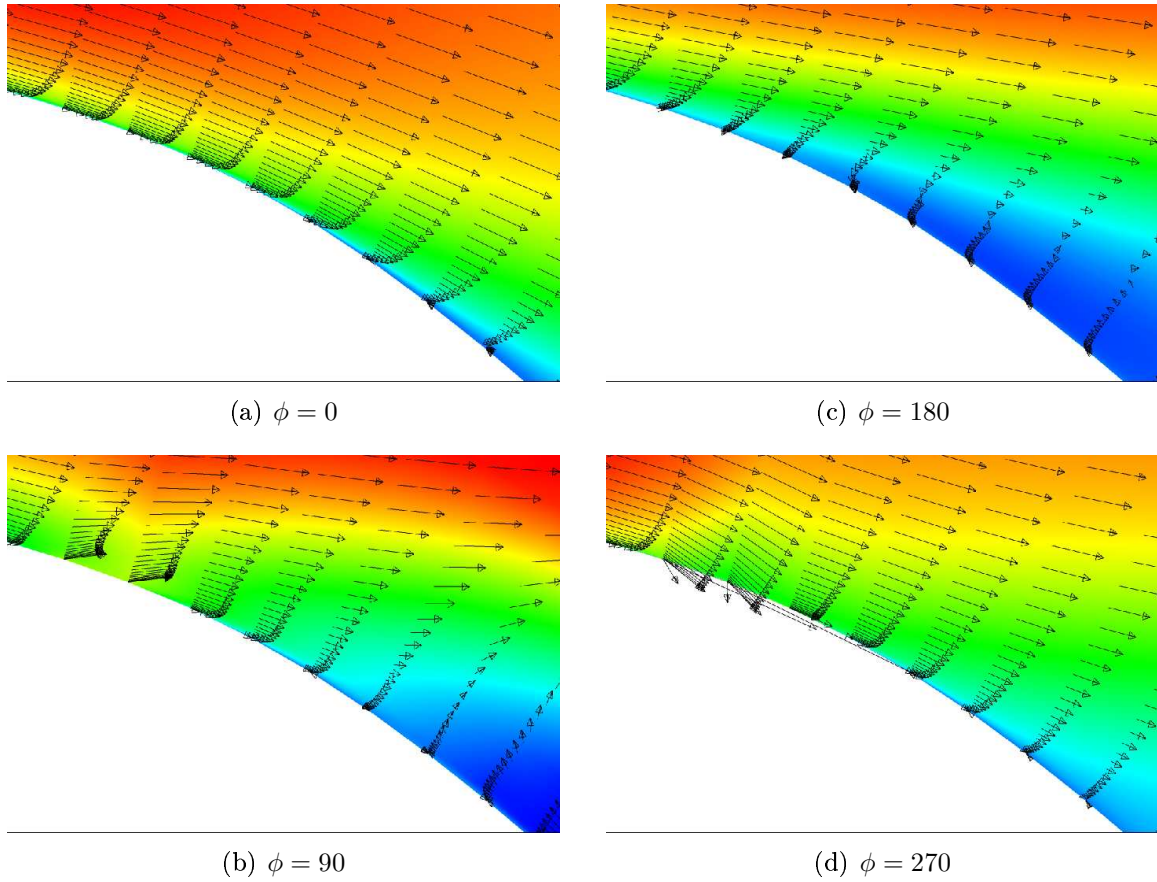


FIGURE 6.14. Phase averaged vorticity and velocity vectors near the slot

such that the shape of that peak is nearly identical to the experimental data.

Somewhat farther downstream, in the recirculation zone (the middle plot), the higher modes have begun to decay, as in the experiment, while the background turbulence level has risen to match the experimental values. A slight remnant of the higher harmonics is present in the simulation results, although no longer visible in the experiment. Far downstream the spectrum is very similar to the unforced case, except that the background turbulence level of the experiment is not overpredicted quite as much.

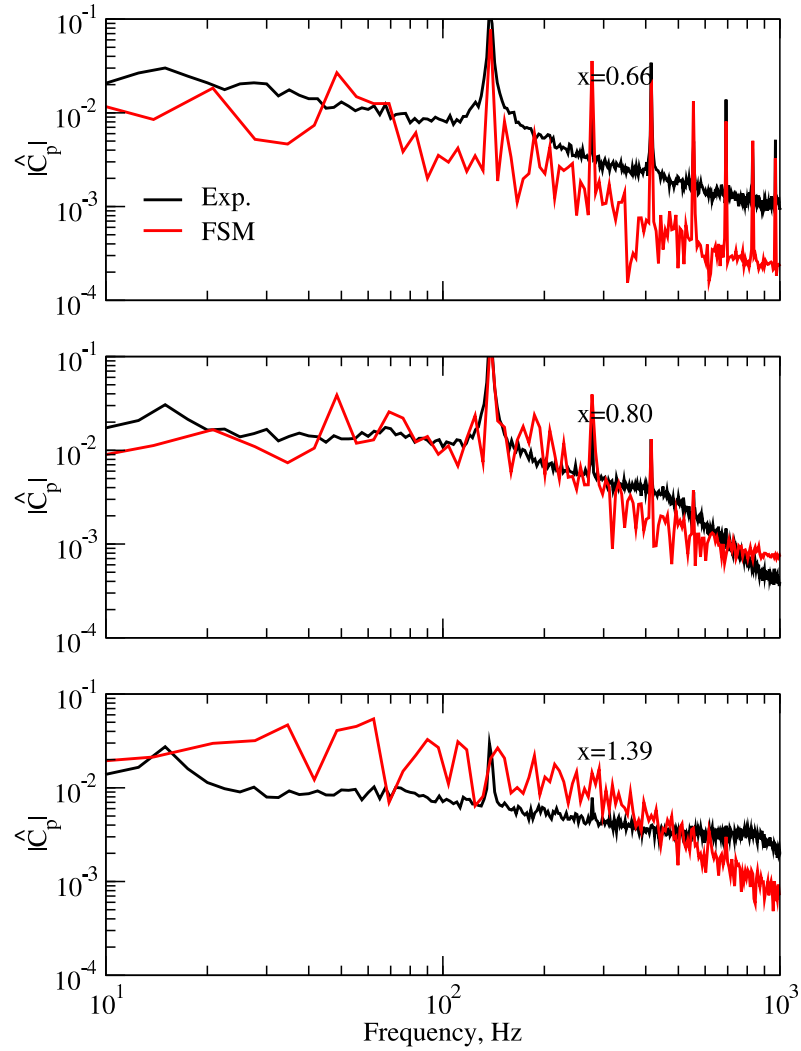


FIGURE 6.15. Wall pressure fluctuation spectra for the flow with oscillatory forcing. The locations of the spectra are indicated in figure 6.9(a) by the dashed lines.

### 6.3 Model Performance

Overall the results for the three cases (baseline, steady suction, and oscillatory) are qualitatively good, but the length of the separated region is consistently overpredicted. However, the model does predict a significant reduction in the size of the separation

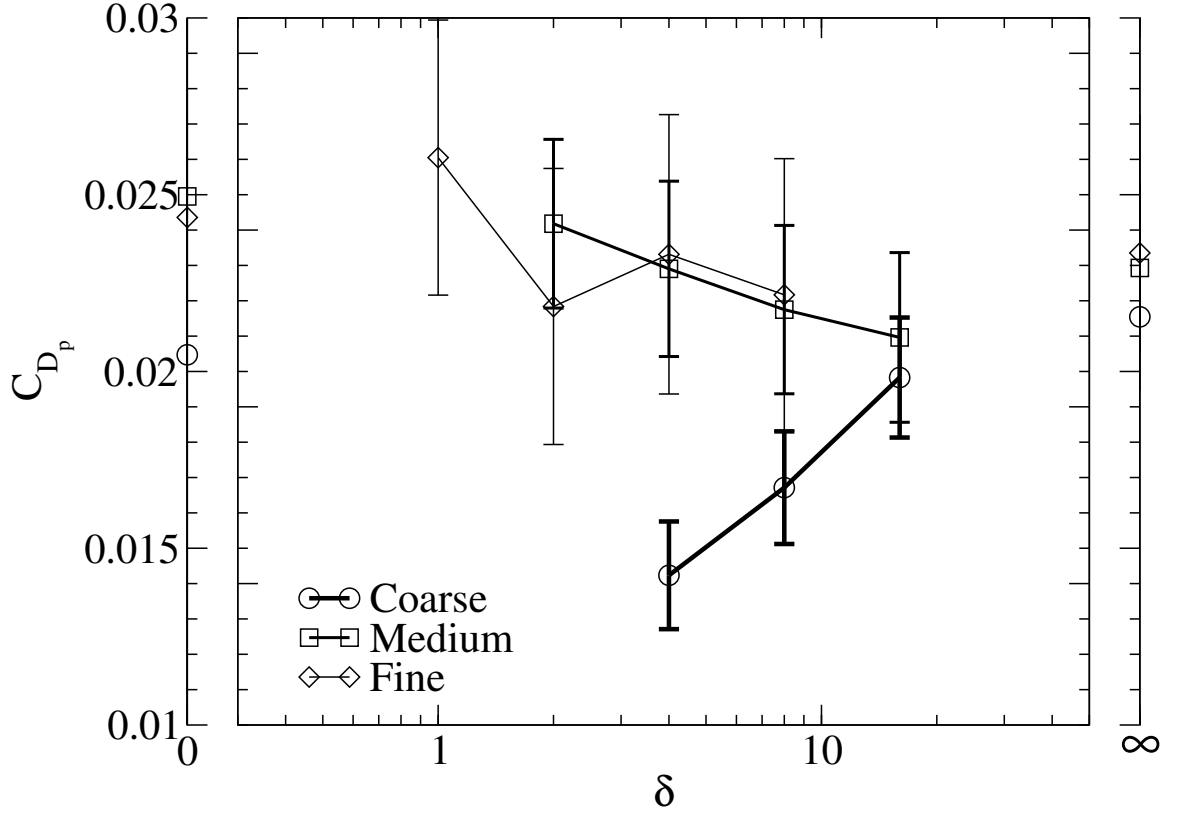


FIGURE 6.16. Pressure drag as a function of filter width for various values of  $\beta$ . For reference the values at the  $\beta = 0$  and  $\beta \rightarrow \infty$  limits are shown schematically on either side.

bubble due to forcing. In order to further investigate the performance of the model, and in particular, to assess the effectiveness of the hybrid methodology, additional simulations were run for the oscillatory case using varying grids and filter widths.

### 6.3.1 Pressure Drag

Figure 6.16 shows the variation in the pressure drag with the model filter width  $\delta$ . Since  $\delta$  is a spatially varying quantity, the value is normalized such that  $\delta = 1$  corresponds to the fine grid with  $\beta = 1$ . That is, taking  $\delta = \beta\Delta$ , and setting  $\Delta_{\text{fine}} = 1$ . The values for the limiting cases of  $\beta = 0$  and  $\beta \rightarrow \infty$  are shown on the left and right

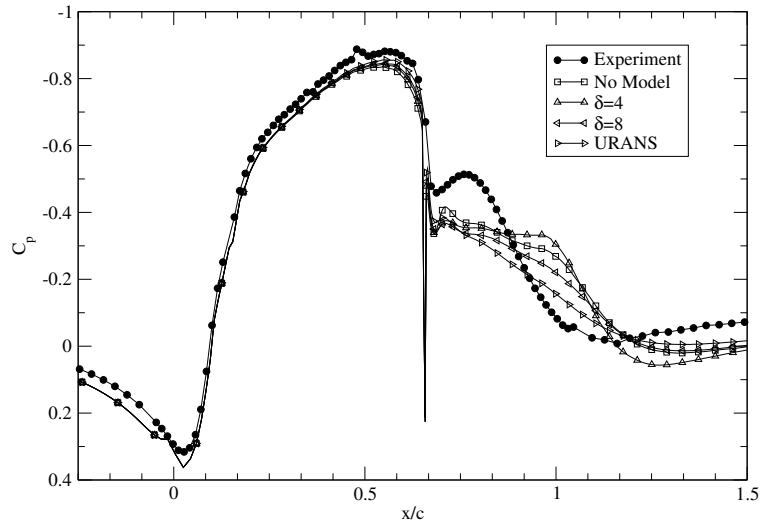


FIGURE 6.17. Time averaged pressure coefficient versus downstream distance for several model filter widths.

side of the plot, respectively. Several points are important to note about this figure. First, while the coarse grid is clearly not well converged, the results on the medium grid appear to be relatively good. Second, it is clear that the resolution requirements do not scale with the filter width; the coarse grid results remain poor even for a very coarse filter. This suggests that the grid requirements are primarily determined by the need to properly resolve either the mean flow or the largest turbulent structures.

### 6.3.2 Surface Pressure Distribution

The experimentally measured pressure drag coefficient of  $C_{D_{p,\text{exp}}} \approx 0.036$  is under-predicted by all the simulations. Observing the trend in figure 6.16 one might be tempted to conclude that the best results are obtained for  $\delta \rightarrow 0$ . However, examining the  $C_p$  profiles (figure 6.17) strongly suggests that this is not the case. Instead it would appear that the best results (at least as far matching the shape of the pressure plateau in the bubble) is for the case of  $\delta = 4$ . The results in figure 6.16 can then be understood as the results of two distinct modeling errors. The first is the overall

lengthening of the bubble due to the slow growth of the fine scale structures in the RANS/LES transition region. This discrepancy is relatively insensitive to the value of  $\delta$ . The second error accounts for the trend in figure 6.16. In this case the discretization error and the model error may be of opposite sign with the optimal behavior in the range of  $\delta \sim 4$ .

### 6.3.3 Reynolds Stresses

To better understand the dynamics of the FSM, and in particular, the reason for the delayed reattachment, it is helpful to examine the various Reynolds stress terms for the different simulations. The Reynolds stress components are shown in figures 6.18-6.21, with the total turbulent stress, which includes of both a resolved scale component and a modeled component, indicated by the solid curves (see equation 4.23). The modeled portion of the stress is indicated by the dashed curves.

Qualitatively, the agreement is reasonably good overall. Several general features should be noted. Consistent with the observations in section 6.2, the delayed reattachment seems to be associated with the transition from RANS to LES. Near the separation location ( $x/c = 0.66$ ) the flow is still essentially steady except in a thin layer immediately adjacent to the slot. At this point the FSM is still functioning as a RANS and therefore there is no significant dependence of the results on the filter width. At  $x/c = 0.8$  the model is still transitioning from RANS to LES behavior, and the fluctuations are underpredicted. As the filter width is increased, so is the model contribution. This suppresses the growth of the resolved structures. As a result, in spite of the larger model contribution, the total Reynolds stress is smallest for the URANS and increases with decreasing filter width. Farther downstream, in the bubble, the overall level is closer to the experimentally observed values. Additionally, the strength of the fluctuations cease to be correlated with the filter width, which is an indication that the RANS to LES transition process has saturated. Finally, at

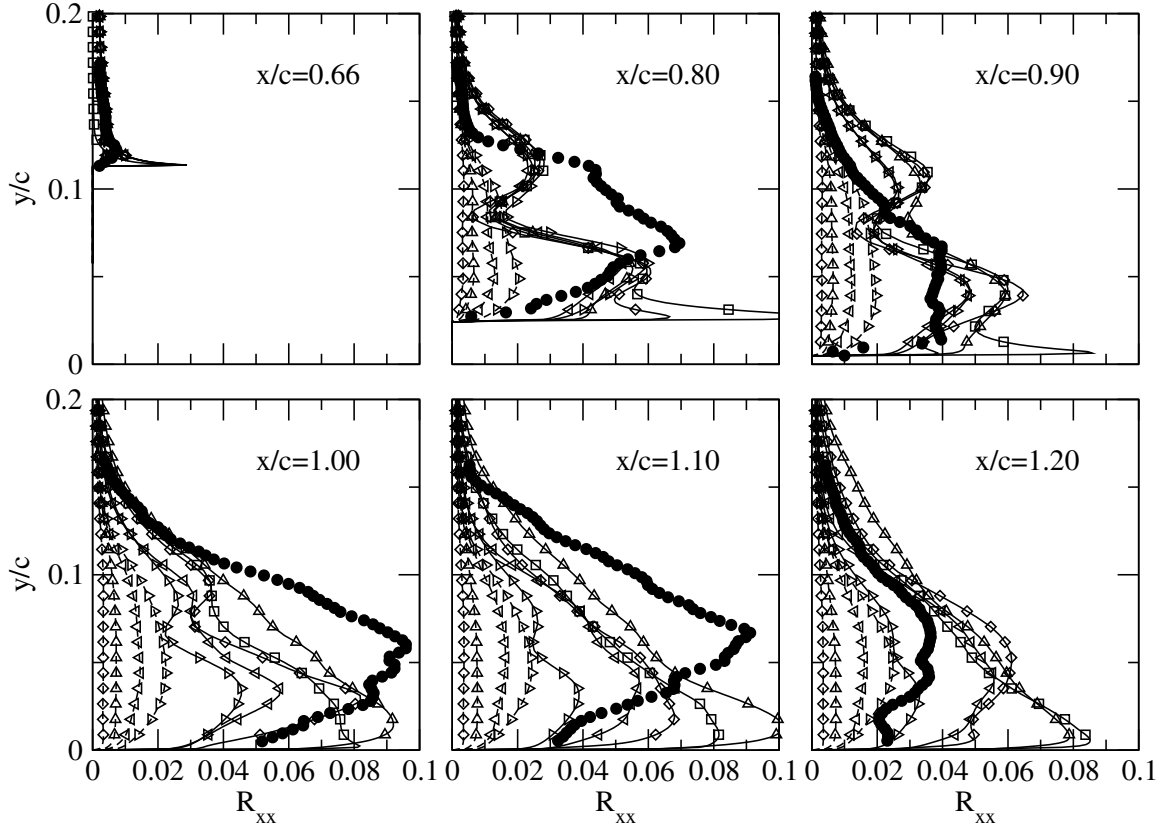


FIGURE 6.18.  $R_{xx}$  profiles for several downstream locations. Experimental data ( $\bullet$ ) and FSM with  $\beta=0$  ( $\square$ ), 2 ( $\diamond$ ), 4 ( $\triangle$ ), 8 ( $\triangleleft$ ), 16 ( $\nabla$ ), and  $\infty$  ( $\triangleright$ ). Dashed lines indicate the model stress, and solid lines the total (modeled plus resolved) stress.

$x/c = 1.2$ , which is near the reattachment point for the simulations, the strength of the fluctuations is overpredicted. This is consistent with the fact that at this location the experimental flow has already reattached and the highest levels of fluctuations are generally seen just upstream of reattachment.

The results for  $\delta = 4$  seem to be overall the best match with the experiments. Interestingly while the  $R_{xx}$  and  $R_{xy}$  stress components are generally underpredicted, the  $R_{yy}$  component is overpredicted, at least for  $\delta \lesssim 4$ . (No experimental data was available for  $R_{zz}$ .)

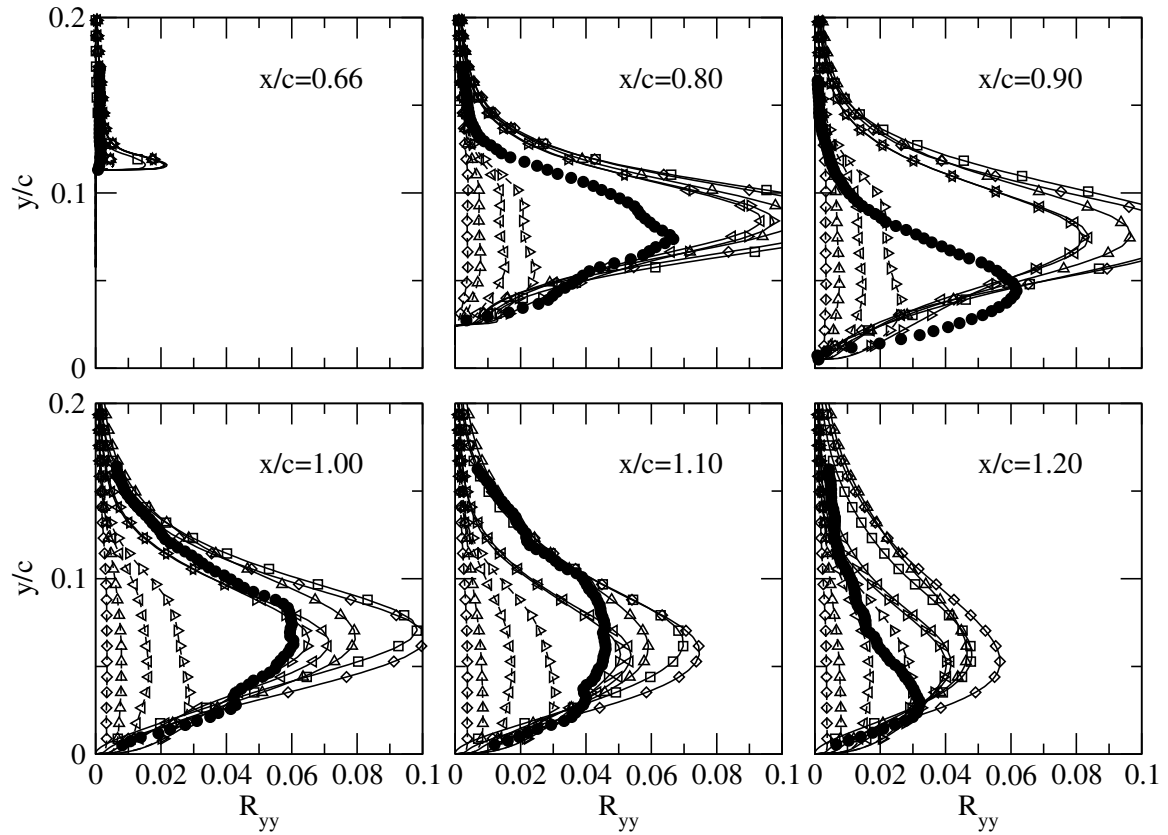


FIGURE 6.19.  $R_{yy}$  profiles for several downstream locations. Experimental data ( $\bullet$ ) and FSM with  $\beta=0$  ( $\square$ ), 2 ( $\diamond$ ), 4 ( $\triangle$ ), 8 ( $\triangleleft$ ), 16 ( $\nabla$ ), and  $\infty$  ( $\triangleright$ ). Dashed lines indicate the model stress, and solid lines the total (modeled plus resolved) stress.

#### 6.3.4 Phase Averaged Structures

Another way to examine the dynamics of the flow is by considering the phase averaged structures (section 4.3.2). Figure 6.22 shows the color contours of the phase averaged vorticity at six different phases. (The phase is defined such that  $\phi = 90$  corresponds to the peak of the blowing phase, consistent with the nomenclature of Greenblatt et al., 2004). Two features to notice are the rapid decay of the structures (although not quite as rapidly as is observed in the experimental data) and that they are quickly swept towards where they dissipate at a location which corresponds roughly to the mean reattachment point.

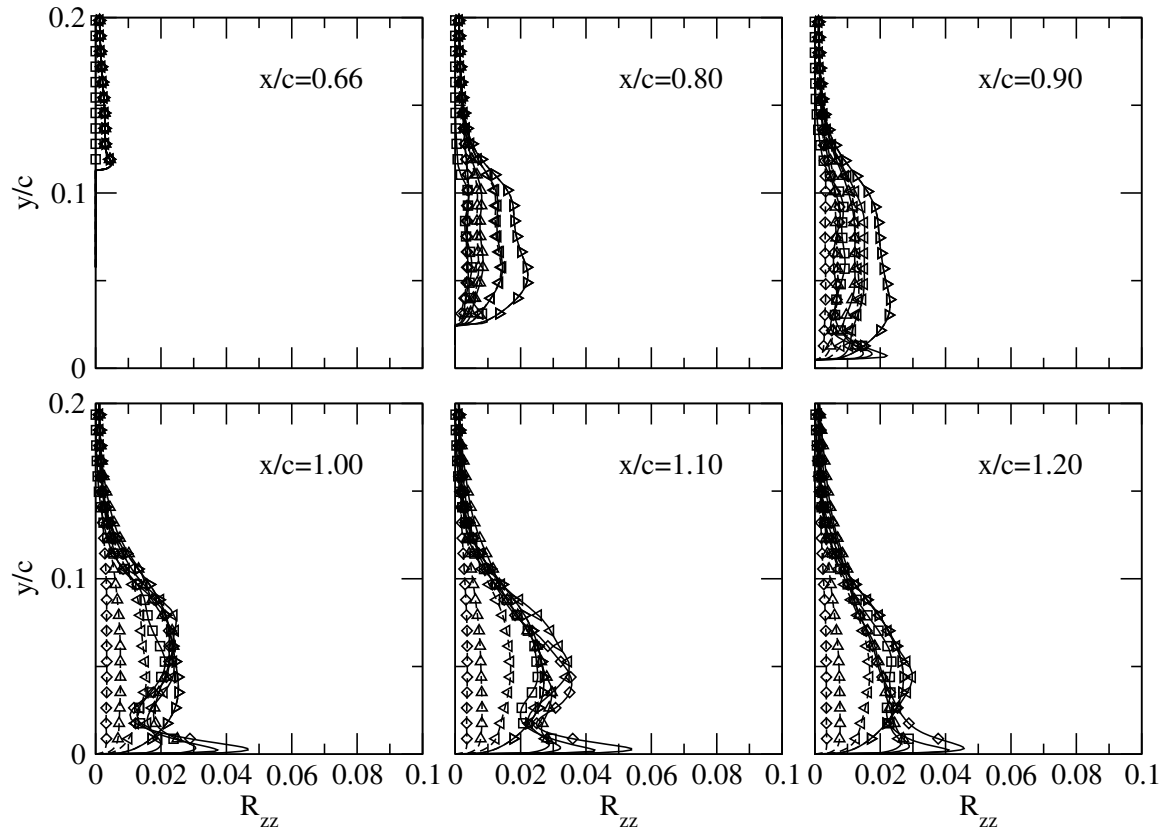


FIGURE 6.20.  $R_{zz}$  profiles for several downstream locations. FSM with  $\beta=0$  ( $\square$ ), 2 ( $\diamond$ ), 4 ( $\triangle$ ), 8 ( $\triangleleft$ ), 16 ( $\nabla$ ), and  $\infty$  ( $\triangleright$ ). Dashed lines indicate the model stress, and solid lines the total (modeled plus resolved) stress.

Another more quantitative comparison is shown in figure 6.23. The wall phase averaged pressure at the wall is shown for four different phases. The circles are the experimental data, and the different curves correspond to different filter widths. The simulations capture the evolution of pressure disturbances quite well, especially near the slot; farther downstream the structures in the simulation start to lag the experimental results somewhat. What is surprising is that the strength of the structures (at least as far as the pressure field is concerned) is almost completely independent of the filter width, in spite of the fact that the kinetic energy does vary significantly, particularly for the URANS case (as can be seen from the diagonal Reynolds stresses,



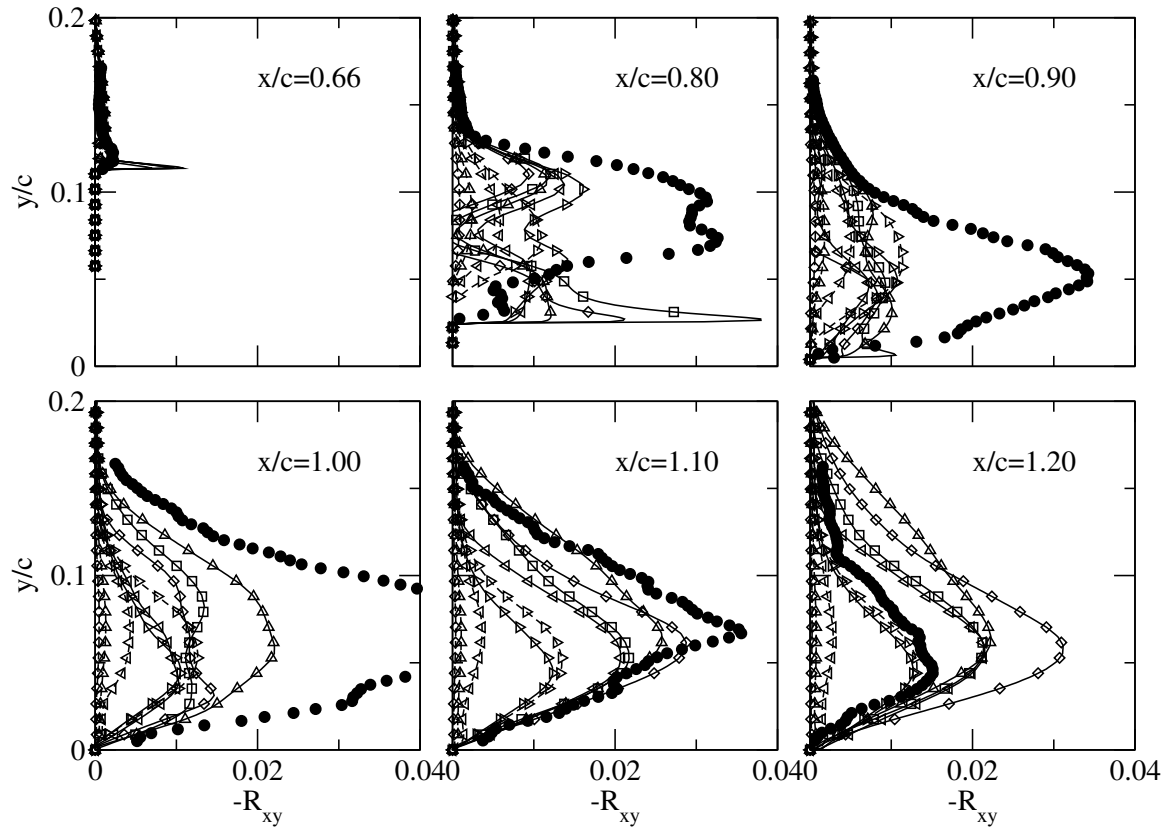


FIGURE 6.21.  $R_{xy}$  profiles for several downstream locations. Experimental data ( $\bullet$ ) and FSM with  $\beta=0$  ( $\square$ ), 2 ( $\diamond$ ), 4 ( $\triangle$ ), 8 ( $\triangleleft$ ), 16 ( $\nabla$ ), and  $\infty$  ( $\triangleright$ ). Dashed lines indicate the model stress, and solid lines the total (modeled plus resolved) stress.

figure 6.18-6.20).

To better comprehend the action of the FSM, it is helpful to further decompose the resolved scale motions into a coherent (phase averaged) and an incoherent part. Figure 6.24 shows the Reynolds stress decomposed into the coherent, incoherent, and modeled parts. The columns are different  $x$  stations, while the rows are different filter widths. As expected, at the first station,  $x/c = 0.8$ , the incoherent motions are quite small and the stress is dominated by the coherent motions when the filter width is small, with the model becoming significant for the coarser filter cases. This is consistent with the understanding that at this station the RANS to LES transition

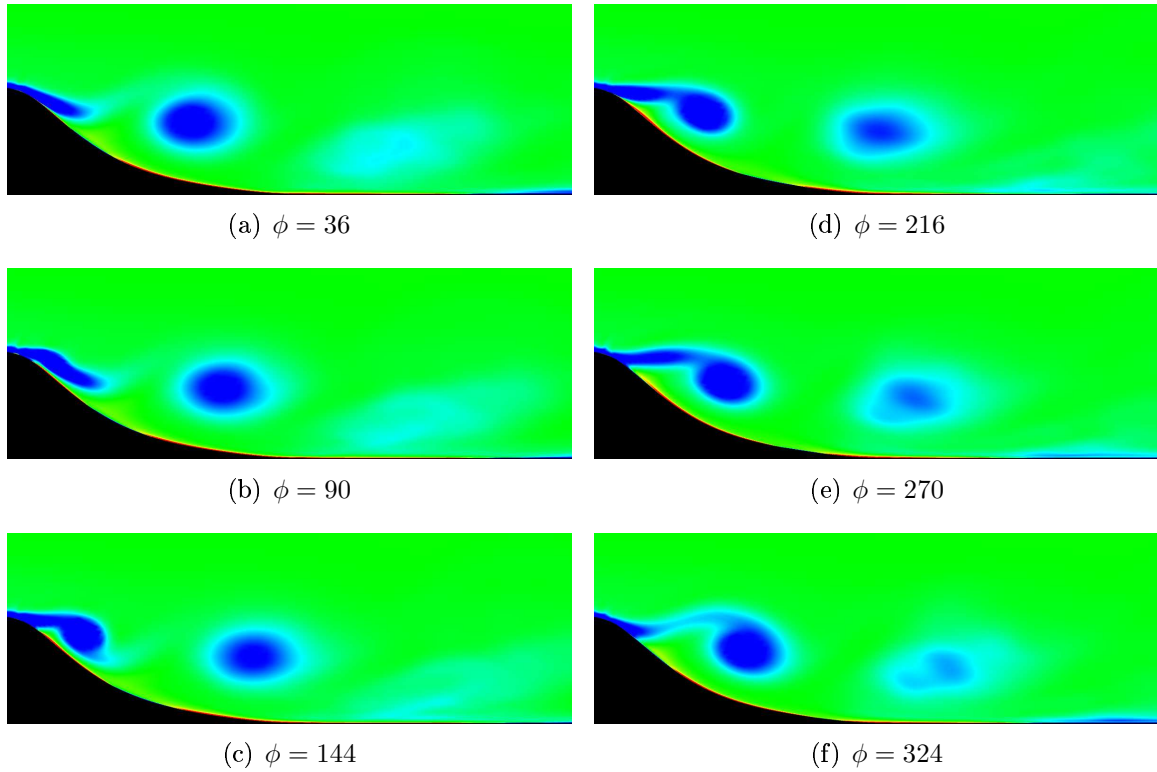


FIGURE 6.22. Phase averaged vorticity

has not finished. By  $x/c = 0.9$ , however, the incoherent part plays a significant role, and by  $x/c = 1.1$ , the incoherent part dominates the flow.

It is also interesting to note that the contribution of the coherent part is generally positive, although the total Reynolds stress remains negative. This positive Reynolds stress is consistent with the coherent Reynolds stress predicted for the mixing layer by Reau and Tumin (2002b). The experimental measurements for the phase averaged Reynolds stress exhibited strong positive regions in the structures, although for the coherent Reynolds stress itself these regions averaged out and no significant positive Reynolds stress was observed.

Based on these observations a much clearer picture of the behavior of the FSM emerges. The principal operation of the FSM in the LES region is to partitioning the energy of the incoherent motions between the model and the incoherent resolved stress

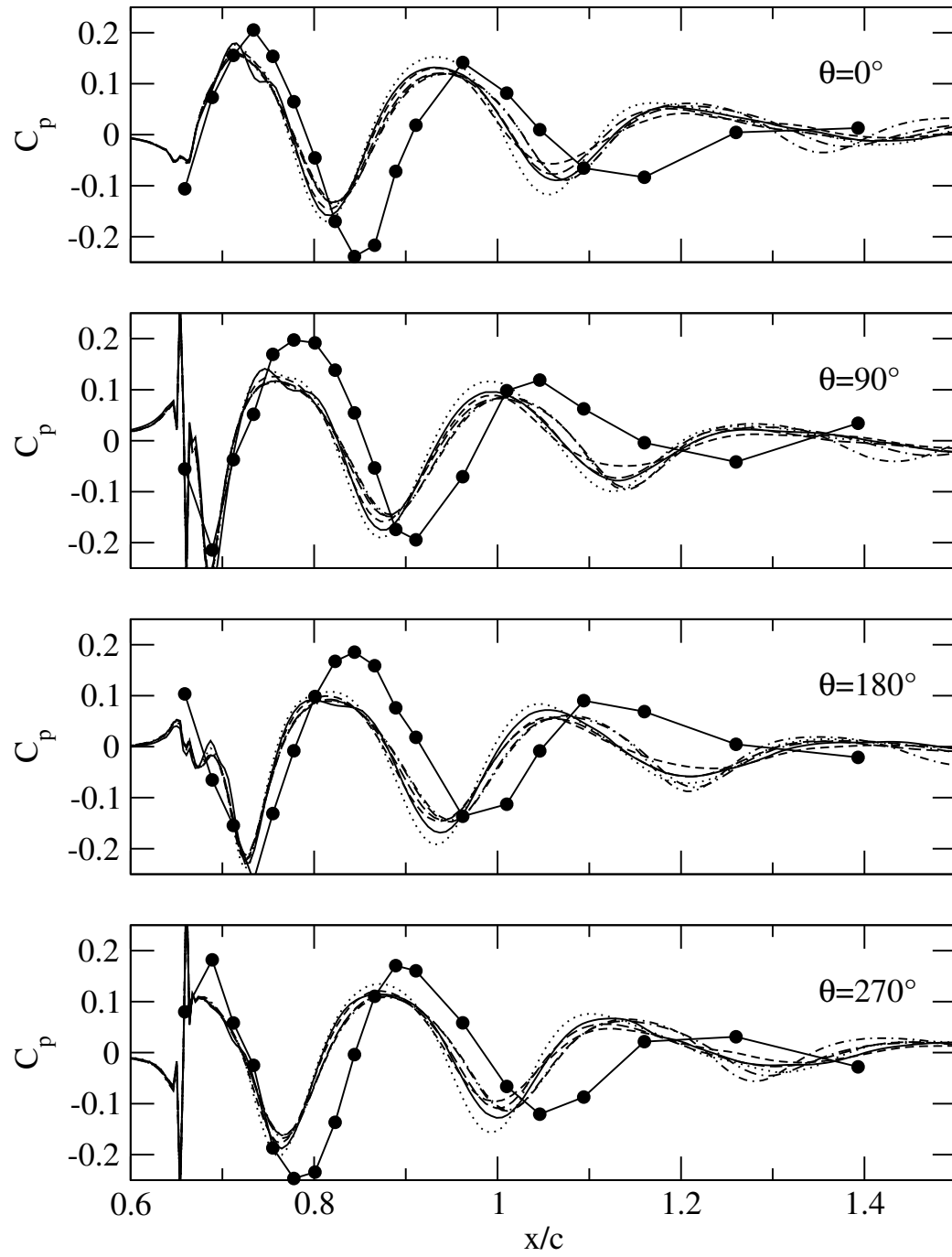


FIGURE 6.23. Phase averaged pressure.

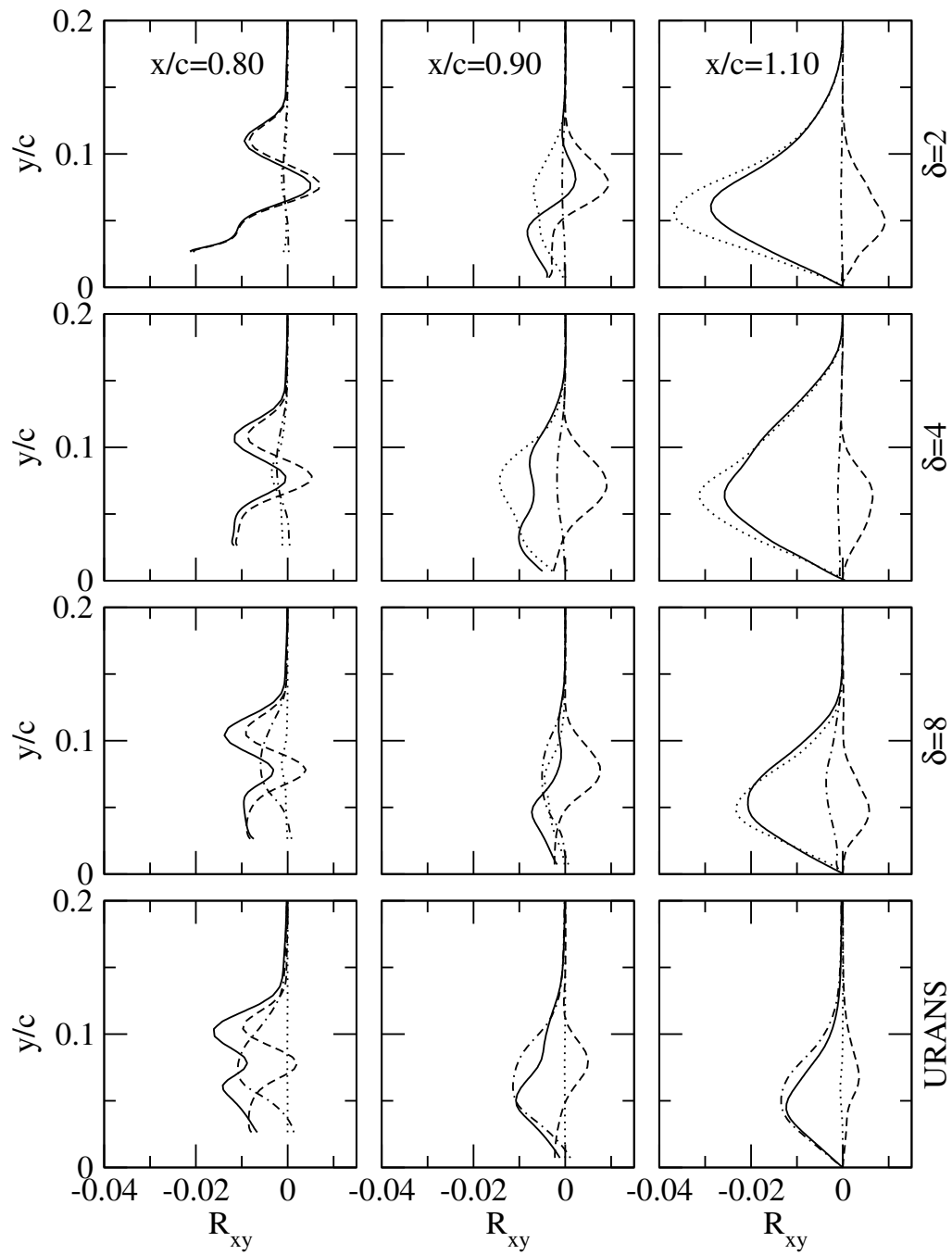


FIGURE 6.24. Reynolds stress terms for several filter widths and downstream locations. Total stress (—), coherent stress (---), incoherent stress (···), and model stress (·-·-)

terms, with the coherent motions remaining largely unaffected. This is consistent with the triple decomposition approach of Reau and Tumin (2002b); in which the coherent structure interacts with itself in a deterministic way but interacts with the incoherent turbulence in a statistical way. In this model, the energy of the coherent part cannot be partially transferred to the model terms, since what would remain in the resolved field would be “part” of a structure: such a decomposition could not be expected to properly capture the essential physics of the dominant coherent structure.

As the FSM filter width is made larger, at some point  $\delta/L \sim 1$  and the model will very quickly begin to behave as a URANS. For the current simulations,  $\delta = 8$  remains an LES, but by  $\delta = 16$  the results are almost identical to the URANS case. With this change, the dynamics of the modeling are completely switched. Instead of being dominated by the incoherent resolved motions, the model terms take over. Nevertheless, over the entire range of filter widths, the strength of the pressure field associated with the large coherent structures, at least as recorded by the footprint on the wall, is only very weakly effected, making the coherent wall pressure trace a poor diagnostic.

Finally, it is important to note that the apparently small size of model contribution for most FSM simulations is somewhat misleading in that even a very small change in model contribution can yield a large change in the other components.

### 6.3.5 Spectra

The effect of  $\beta$  can also be seen in the spectra (figure 6.25). The broad peak at 50Hz, which reflects the natural shedding frequency, as well as the sharp peak at the forcing frequency (138.5Hz) and its harmonics are largely unaffected by the magnitude of the model contribution. As the model contribution is increased the broader baseline spectra, which represents the background turbulence, is suppressed especially at higher frequencies. The higher harmonics of the forcing frequency, however, are not

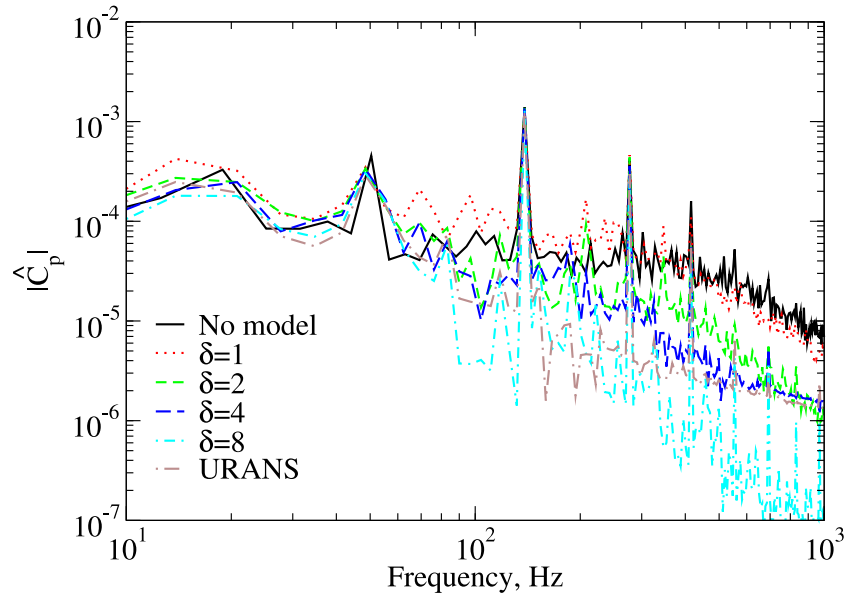


FIGURE 6.25. Wall pressure fluctuation spectra for the flow with oscillatory forcing at  $x/c = 0.8$ . The arrow indicates the trend for increasing  $\beta$ .

noticeably affected. These discrete frequencies represent the periodic part of the signal with period identical to the forcing period. This suggests that the large structures triggered by the forcing are not significantly distorted by the model.

### 6.3.6 Instantaneous

Additional physical insight on the effect of  $\beta$  can be obtained by observing the flow structures at a particular instant in time (figure 6.26). Here the structures identified by the  $\lambda_2$  vortex identification criterion (Jeong and Hussain, 1995) are plotted for different values of  $\beta$ . The same level of  $\lambda_2$  is used to generate all the plots, and they are taken at the identical physical time of the simulation. For all values of  $\beta$  a strong two-dimensional “roller” in the shear layer can be seen just downstream of the separation location. However, the degree of three-dimensional modulation of these

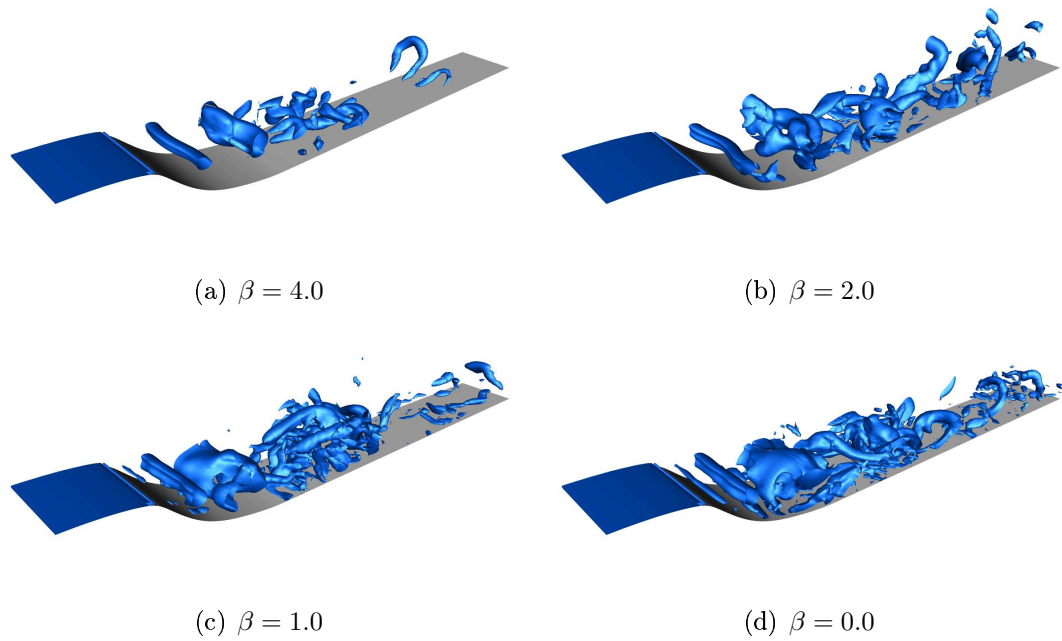


FIGURE 6.26. Isosurfaces of  $\lambda_2$  vortex identification criteria for various values of the contribution constant  $\beta$ .

rollers varies with  $\beta$ . Farther downstream a breakdown of the rollers can be observed; the range of scales resolved clearly increases as the model contribution is reduced.

## Chapter 7

# CONCLUSIONS

Attempts to combine RANS and LES techniques have largely foundered because they treat RANS and LES as completely separate approaches which must be patched together in some manner. The current approach uses the formal similarity between the LES and RANS equations (also called the averaging invariance) to unify the two approaches. This provides a general framework for developing new classes of turbulence models, called bridging models. For the current work, the FSM is presented in the context of this development. In this light the FSM can be understood not as a traditional hybrid model, but as the first true bridging model.

Although the FSM was introduced essentially as a hybrid model, that is, as a way to bridge the divide between RANS and LES, the current results show that one of the primary strengths of the FSM actually lies in its excellent performance as a VLES. It appears that by integrating a state of the art RANS model into the method in the LES regime the model remains robust even for very coarse filters where conventional LES techniques typically perform quite poorly.

Modifying slightly the traditional definition of VLES to a model in which only the largest coherent structures are resolved, it becomes clear that there is little difference between a VLES and a bridging approach. Depending on how coherent structures are defined, for example, a boundary layer may have no large coherent structures. Certainly it has no dominant structures in the phase averaged sense. So with this definition a VLES of boundary layer would reduce to a RANS.

So how does the FSM perform as a bridging model? Qualitatively the FSM is quite promising, but it still suffers from some of the difficulties common to all hybrid models. The first and most significant of these is the artificial transition which occurs as the



model switches from RANS to LES. In such regions the incoming flow is devoid of the small scale incoherent motions that the model requires to replace the subfilter stresses. The only mechanism for generating such structures are hydrodynamic instabilities which follow a route which looks strikingly like transition to turbulence, but which is occurring in a region where the real flow is already fully turbulent. It is not clear to what extent, if any, this artificial transition corresponds to any actual physical process present in the flow.

It is also unclear how the growth of the large coherent waves fares in this transitional region. In the RANS regime these waves are probably overdamped, since traditional RANS models are not designed to include unsteady turbulent structures. It remains to be seen whether further extending the bridging model concept can help to eliminate this problem.

What the FSM does very well is in balancing the action of the model and the incoherent resolved motions, so that it provides relatively robust results over a wide range of filter widths. Although the total Reynolds stress in the LES region is not completely independent of filter width, it is only weakly dependent. And even that weak dependence is likely due to the ad-hoc nature of the contribution function. Although the contribution function introduced in the current work has the correct qualitative behavior, the actual scaling is based on a  $k^{-5/3}$  spectrum, which is probably unrealistic for this flow. Also, even the fine grid is still coarse enough that only a very small range of filter widths can be properly resolved numerically, as discussed in section 4.1.2.

From the work of Bachman (2001) it was already clear that FSM is least successful when the filter width is just slightly smaller than integral length scale. In this regime the model contribution is not large enough to replace the large structures, but is large enough to damp out any large scale structures in the resolved fields. The current work sheds further light on these dynamics. It is clear that the FSM should not be understood in terms of a traditional decomposition into resolved and subfilter

parts, with the contribution function determining the partitioning between them. Instead, a better conceptual model is a triple decomposition, with the resolved motions being further decomposed into coherent motions, which must be resolved, and incoherent motions, whose action is mainly statistical. In this model, the contribution function serves mainly to partition the energy between the model and the incoherent resolved part, with the coherent resolved part remaining, ideally, unaffected. This picture, which in some ways is closer to VLES, points to the potential for improving the methodology to perform well even near the RANS limit, by further refining the contribution function and adjustments to the underlying RANS model.

RANS modeling has been around for about eighty years, and LES for about half that time. In comparison, the concept of a bridging model is still in its infancy. In fact, such ideas as hybrid modeling, VLES, and URANS demonstrate that the turbulence modeling community has still not reached a consensus on the best direction to go forward. What is clear is that we need some form of bridging model. Whether the FSM itself will be that model, or whether other approaches will be developed in the future, the FSM continues to demonstrate the power of the synergy of bridging the RANS/LES divide.

## Appendix A

### THE GENERALIZED MOMENT EQUATIONS

#### A.1 Properties of the Generalized Moments

The generalized second and third order moments are defined as (Germano, 1992):

$$\tau(f, g) = \overline{fg} - \bar{f}\bar{g} \quad (\text{A.1})$$

$$\tau(f, g, h) = \overline{fgh} - \bar{f}\tau(g, h) - \bar{g}\tau(f, h) - \bar{h}\tau(fg) - \bar{f}\bar{g}\bar{h} \quad (\text{A.2})$$

By inspection the moments are invariant under permutation of the arguments. Linearity is straight forward to demonstrate:

$$\begin{aligned} \tau(f_1 + af_2, g) &= \overline{(f_1 + af_2)g} - \overline{(f_1 + af_2)}\bar{g} \\ &= \overline{f_1g} - \bar{f}_1\bar{g} + a(\overline{f_2g} - \bar{f}_2\bar{g}) \\ &= \tau(f_1, g) + a\tau(f_2, g), \end{aligned} \quad (\text{A.3})$$

and similarly for the third order moments. Linearity also implies the product rule for differentiation,

$$\begin{aligned} \frac{\partial \tau(f, g)}{\partial x} &= \frac{\partial}{\partial x} [\overline{fg} - \bar{f}\bar{g}] \\ &= \frac{\partial \overline{f}}{\partial x} \bar{g} - \frac{\partial \bar{f}}{\partial x} \bar{g} + \overline{f \frac{\partial g}{\partial x}} - \bar{f} \frac{\partial \bar{g}}{\partial x} \\ &= \tau\left(\frac{\partial f}{\partial x}, g\right) + \tau\left(f, \frac{\partial g}{\partial x}\right), \end{aligned} \quad (\text{A.4})$$

and

$$\begin{aligned}
\frac{\partial \tau(f, g, h)}{\partial x} &= \frac{\partial}{\partial x} [\overline{fgh} - \overline{f}\tau(g, h) - \overline{g}\tau(f, h) - \overline{h}\tau(f, g) - \overline{f}\overline{g}\overline{h}] \\
&= \frac{\partial \overline{f}}{\partial x} \overline{gh} + \overline{f} \frac{\partial \overline{g}}{\partial x} \overline{h} + \overline{f} \overline{g} \frac{\partial \overline{h}}{\partial x} \\
&\quad - \frac{\partial \overline{f}}{\partial x} \tau(g, h) - \overline{f} \tau\left(\frac{\partial g}{\partial x}, h\right) + \overline{f} \tau\left(g, \frac{\partial h}{\partial x}\right) \\
&\quad - \frac{\partial \overline{g}}{\partial x} \tau(f, h) - \overline{g} \tau\left(\frac{\partial f}{\partial x}, h\right) - \overline{g} \tau\left(f, \frac{\partial h}{\partial x}\right) \\
&\quad - \frac{\partial \overline{h}}{\partial x} \tau(f, g) - \overline{h} \tau\left(\frac{\partial f}{\partial x}, g\right) - \overline{h} \tau\left(f, \frac{\partial g}{\partial x}\right) \\
&\quad - \frac{\partial \overline{f}}{\partial x} \overline{g}\overline{h} - \overline{f} \frac{\partial \overline{g}}{\partial x} \overline{h} - \overline{f} \overline{g} \frac{\partial \overline{h}}{\partial x} \\
&= \tau\left(\frac{\partial f}{\partial x}, g, h\right) + \tau\left(f, \frac{\partial g}{\partial x}, h\right) + \tau\left(f, g, \frac{\partial h}{\partial x}\right). \tag{A.5}
\end{aligned}$$

For the Laplacian of a moment we have

$$\begin{aligned}
\nabla^2 \tau(f, g) &= \frac{\partial}{\partial x_i} \left[ \frac{\partial \tau(f, g)}{\partial x_i} \right] \\
&= \frac{\partial}{\partial x_i} \left[ \tau\left(\frac{\partial f}{\partial x_i}, g\right) + \tau\left(f, \frac{\partial g}{\partial x_i}\right) \right] \\
&= \tau(\nabla^2 f, g) + 2\tau\left(\frac{\partial f}{\partial x_i}, \frac{\partial g}{\partial x_i}\right) + \tau\left(f, \nabla^2 g\right). \tag{A.6}
\end{aligned}$$

It can be useful expression to express the triple correlation in terms of double correlations by noting that

$$\begin{aligned}
\tau(fg, h) &= \overline{fgh} - \overline{f}\overline{g}\overline{h} \\
&= \overline{fgh} - \overline{f}\overline{g}\overline{h} + \overline{f}\overline{g}\overline{h} - \overline{f}\overline{g}\overline{h} \\
&= \overline{fgh} - \tau(f, g)\overline{h} - \overline{f}\overline{g}\overline{h}.
\end{aligned}$$

Substituting into the definition of the triple moment we get

$$\begin{aligned}
\tau(f, g, h) &= \overline{fgh} - \overline{f}\tau(g, h) - \overline{g}\tau(f, h) - \overline{h}\tau(f, g) - \overline{f}\overline{g}\overline{h} \\
&= \tau(fg, h) - \overline{f}\tau(g, h) - \overline{g}\tau(f, h),
\end{aligned}$$

or

$$\tau(fg, h) = \tau(f, g, h) + \bar{f}\tau(g, h) - \bar{g}\tau(f, h). \quad (\text{A.7})$$

## A.2 Generalized Moment Equations

### A.2.1 Generalized Subfilter Stress Equations

Denoting the Navier-Stokes operator by

$$\mathcal{N}[u_i] = 0 \quad (\text{A.8})$$

the evolution equations for the subfilter stress tensor is derived by forming the moment

$$\tau(u_i, \mathcal{N}[u_j]) + \tau(u_j, \mathcal{N}[u_i]) = 0. \quad (\text{A.9})$$

Expanding, we obtain

$$\begin{aligned} & \tau\left(u_i, \frac{\partial u_j}{\partial t}\right) + \tau\left(u_j, \frac{\partial u_i}{\partial t}\right) + \tau\left(u_i, u_k \frac{\partial u_j}{\partial x_k}\right) + \tau\left(u_j, u_k \frac{\partial u_i}{\partial x_k}\right) \\ &= -\frac{1}{\rho} \left[ \tau\left(u_i, \frac{\partial p}{\partial x_j}\right) + \tau\left(u_j, \frac{\partial p}{\partial x_i}\right) \right] + \nu \tau(u_i, \nabla^2 u_j) + \nu \tau(u_j, \nabla^2 u_i) \\ & \frac{\partial \tau(u_i, u_j)}{\partial x} + \tau\left(u_i, u_k \frac{\partial u_j}{\partial x_k}\right) + \tau\left(u_j, u_k \frac{\partial u_i}{\partial x_k}\right) \\ &= -\frac{1}{\rho} \left[ \tau\left(u_i, \frac{\partial p}{\partial x_j}\right) + \tau\left(u_j, \frac{\partial p}{\partial x_i}\right) \right] + \nu \nabla^2 \tau(u_i, u_j) - 2\nu \tau\left(\frac{\partial u_i}{\partial x_k}, \frac{\partial u_j}{\partial x_k}\right), \end{aligned}$$

where we have used (A.6) to recast the diffusion term. The transport terms can be rewritten using (A.7):

$$\begin{aligned} & \tau\left(u_i, u_k \frac{\partial u_j}{\partial x_k}\right) + \tau\left(u_j, u_k \frac{\partial u_i}{\partial x_k}\right) \\ &= \tau\left(u_i, u_k, \frac{\partial u_j}{\partial x_k}\right) + \overline{u_k} \tau\left(u_i, \frac{\partial u_j}{\partial x_k}\right) + \frac{\partial \overline{u_j}}{\partial x_k} \tau(u_i, u_k) \\ &+ \tau\left(u_j, u_k, \frac{\partial u_i}{\partial x_k}\right) + \overline{u_k} \tau\left(u_j, \frac{\partial u_i}{\partial x_k}\right) + \frac{\partial \overline{u_i}}{\partial x_k} \tau(u_j, u_k) \\ &= \frac{\partial \tau(u_i, u_j, u_k)}{\partial x_k} + \overline{u_k} \frac{\partial \tau(u_i, u_j)}{\partial x_k} + \frac{\partial \overline{u_j}}{\partial x_k} \tau(u_i, u_k) + \frac{\partial \overline{u_i}}{\partial x_k} \tau(u_j, u_k) \end{aligned}$$

where we have used incompressibility to combine the triple correlation terms. The pressure term can be rewritten as

$$\tau \left( u_i, \frac{\partial p}{\partial x_j} \right) = \frac{\partial}{\partial x_j} [\tau(u_i, p)] - \left[ \tau \left( p, \frac{\partial u_i}{\partial x_j} \right) \right].$$

The evolution equations for the subfilter stress tensor can therefore be expressed as

$$\frac{\partial \tau(u_i, u_j)}{\partial x} + \overline{u_k} \frac{\partial \tau(u_i, u_j)}{\partial x_k} = \nu \nabla^2 \tau(u_i, u_j) + \Pi_{ij} + \mathcal{D}_{ij} + \mathcal{P}_{ij} - \varepsilon_{ij}, \quad (\text{A.10})$$

where

$$\begin{aligned} \Pi_{ij} &= -\frac{1}{\rho} \left[ \tau \left( p, \frac{\partial u_i}{\partial x_j} \right) + \tau \left( p, \frac{\partial u_j}{\partial x_i} \right) \right] \\ \mathcal{D}_{ij} &= -\frac{1}{\rho} \frac{\partial}{\partial x_j} [\tau(u_i, p)] - \frac{1}{\rho} \frac{\partial}{\partial x_i} \tau(u_j, p) - \frac{\partial \tau(u_i, u_j, u_k)}{\partial x_k} \\ \mathcal{P}_{ij} &= -\frac{\partial \overline{u_i}}{\partial x_k} \tau(u_j, u_k) - \frac{\partial \overline{u_j}}{\partial x_k} \tau(u_i, u_k) \\ \varepsilon_{ij} &= 2\nu \tau \left( \frac{\partial u_i}{\partial x_k}, \frac{\partial u_j}{\partial x_k} \right) \end{aligned}$$

are the pressure-strain rate correlation tensor, the turbulent diffusion of subfilter stress, the production of subfilter stress and the generalized dissipation rate tensor, respectively.

### A.2.2 Generalized Subgrid Dissipation Rate Equations

The equation for the generalized dissipation tensor is derived by forming the moment

$$2\nu \left[ \tau \left( \frac{\partial u_i}{\partial x_k}, \frac{\partial \mathcal{N}[u_j]}{\partial x_k} \right) + \tau \left( \frac{\partial u_j}{\partial x_k}, \frac{\partial \mathcal{N}[u_i]}{\partial x_k} \right) \right] = 0.$$

Expanding, we have

$$\begin{aligned} &\frac{\partial}{\partial t} \left[ \tau \left( \frac{\partial u_i}{\partial x_k}, \frac{\partial u_j}{\partial x_k} \right) \right] + \tau \left( \frac{\partial u_i}{\partial x_k}, \frac{\partial}{\partial x_k} \left[ u_l \frac{\partial u_j}{\partial x_l} \right] \right) + \tau \left( \frac{\partial u_j}{\partial x_k}, \frac{\partial}{\partial x_k} \left[ u_l \frac{\partial u_i}{\partial x_l} \right] \right) \\ &= -\frac{1}{\rho} \left[ \tau \left( \frac{\partial u_i}{\partial x_k}, \frac{\partial}{\partial x_k} \left[ \frac{\partial p}{\partial x_j} \right] \right) + \tau \left( \frac{\partial u_j}{\partial x_k}, \frac{\partial}{\partial x_k} \left[ \frac{\partial p}{\partial x_i} \right] \right) \right] \\ &\quad + \nu \nabla^2 \left[ \tau \left( \frac{\partial u_i}{\partial x_k}, \frac{\partial u_j}{\partial x_k} \right) \right] - 2\nu \tau \left( \frac{\partial^2 u_i}{\partial x_k \partial x_l}, \frac{\partial^2 u_j}{\partial x_k \partial x_l} \right). \end{aligned}$$

Now we can recast the transport terms:

$$\begin{aligned} & \tau \left( \frac{\partial u_i}{\partial x_k}, \frac{\partial}{\partial x_k} \left[ u_l \frac{\partial u_j}{\partial x_l} \right] \right) + \tau \left( \frac{\partial u_j}{\partial x_k}, \frac{\partial}{\partial x_k} \left[ u_l \frac{\partial u_i}{\partial x_l} \right] \right) \\ &= \tau \left( \frac{\partial u_i}{\partial x_k}, \frac{\partial u_l}{\partial x_k} \frac{\partial u_j}{\partial x_l} \right) + \tau \left( \frac{\partial u_i}{\partial x_k}, u_l \frac{\partial^2 u_j}{\partial x_k \partial x_l} \right) + \tau \left( \frac{\partial u_j}{\partial x_k}, \frac{\partial u_l}{\partial x_k} \frac{\partial u_i}{\partial x_l} \right) + \tau \left( \frac{\partial u_j}{\partial x_k}, u_l \frac{\partial^2 u_i}{\partial x_k \partial x_l} \right). \end{aligned}$$

We can recast the first and third term using (A.7), so

$$\begin{aligned} & \tau \left( \frac{\partial u_i}{\partial x_k}, \frac{\partial u_l}{\partial x_k} \frac{\partial u_j}{\partial x_l} \right) + \tau \left( \frac{\partial u_j}{\partial x_k}, \frac{\partial u_l}{\partial x_k} \frac{\partial u_i}{\partial x_l} \right) \\ &= \tau \left( \frac{\partial u_i}{\partial x_k}, \frac{\partial u_l}{\partial x_k}, \frac{\partial u_j}{\partial x_l} \right) + \frac{\partial \bar{u}_l}{\partial x_k} \tau \left( \frac{\partial u_i}{\partial x_k}, \frac{\partial u_j}{\partial x_l} \right) + \frac{\partial \bar{u}_j}{\partial x_l} \tau \left( \frac{\partial u_i}{\partial x_k}, \frac{\partial u_l}{\partial x_k} \right) \\ &+ \tau \left( \frac{\partial u_j}{\partial x_k}, \frac{\partial u_l}{\partial x_k}, \frac{\partial u_i}{\partial x_l} \right) + \frac{\partial \bar{u}_l}{\partial x_k} \tau \left( \frac{\partial u_j}{\partial x_k}, \frac{\partial u_i}{\partial x_l} \right) + \frac{\partial \bar{u}_i}{\partial x_l} \tau \left( \frac{\partial u_j}{\partial x_k}, \frac{\partial u_l}{\partial x_k} \right). \end{aligned}$$

The second and fourth term can be rewritten as

$$\begin{aligned} & \tau \left( \frac{\partial u_i}{\partial x_k}, u_l \frac{\partial^2 u_j}{\partial x_k \partial x_l} \right) + \tau \left( \frac{\partial u_j}{\partial x_k}, u_l \frac{\partial^2 u_i}{\partial x_k \partial x_l} \right) \\ &= \tau \left( \frac{\partial u_i}{\partial x_k}, u_l \frac{\partial^2 u_j}{\partial x_l \partial x_k} \right) + \tau \left( \frac{\partial u_j}{\partial x_k}, u_l \frac{\partial^2 u_i}{\partial x_l \partial x_k} \right) \\ &= \tau \left( \frac{\partial u_i}{\partial x_k}, u_l, \frac{\partial^2 u_j}{\partial x_l \partial x_k} \right) + \bar{u}_l \tau \left( \frac{\partial u_i}{\partial x_k}, \frac{\partial^2 u_j}{\partial x_l \partial x_k} \right) + \frac{\partial^2 \bar{u}_j}{\partial x_l \partial x_k} \tau \left( \frac{\partial u_i}{\partial x_k}, u_l \right) \\ &+ \tau \left( \frac{\partial u_j}{\partial x_k}, u_l, \frac{\partial^2 u_i}{\partial x_l \partial x_k} \right) + \bar{u}_l \tau \left( \frac{\partial u_j}{\partial x_k}, \frac{\partial^2 u_i}{\partial x_l \partial x_k} \right) + \frac{\partial^2 \bar{u}_i}{\partial x_l \partial x_k} \tau \left( \frac{\partial u_j}{\partial x_k}, u_l \right) \\ &= \bar{u}_l \frac{\partial}{\partial x_l} \left[ \tau \left( \frac{\partial u_i}{\partial x_k}, \frac{\partial u_j}{\partial x_k} \right) \right] \\ &+ \frac{\partial}{\partial x_l} \left[ \tau \left( u_l, \frac{\partial u_i}{\partial x_k}, \frac{\partial u_j}{\partial x_k} \right) \right] \\ &+ \frac{\partial^2 \bar{u}_i}{\partial x_l \partial x_k} \tau \left( \frac{\partial u_j}{\partial x_k}, u_l \right) + \frac{\partial^2 \bar{u}_j}{\partial x_l \partial x_k} \tau \left( \frac{\partial u_i}{\partial x_k}, u_l \right). \end{aligned}$$

The pressure term can be rewritten

$$\begin{aligned} \tau \left( \frac{\partial u_i}{\partial x_k}, \frac{\partial}{\partial x_k} \left[ \frac{\partial p}{\partial x_j} \right] \right) &= \tau \left( \frac{\partial u_i}{\partial x_k}, \frac{\partial}{\partial x_j} \left[ \frac{\partial p}{\partial x_k} \right] \right) \\ &= \frac{\partial}{\partial x_j} \left[ \tau \left( \frac{\partial u_i}{\partial x_k}, \frac{\partial p}{\partial x_k} \right) \right] - \tau \left( \frac{\partial p}{\partial x_k}, \frac{\partial}{\partial x_j} \left[ \frac{\partial u_i}{\partial x_k} \right] \right). \end{aligned}$$

Substituting all of the above expressions into the moment equation and multiplying by  $2\nu$  and using the definition of  $\varepsilon_{ij}$  where appropriate we obtain:

$$\frac{\partial \varepsilon_{ij}}{\partial t} + \overline{u_k} \frac{\partial \varepsilon_{ij}}{\partial x_k} = -\mathcal{P}_{ij}^\varepsilon - \Phi_{ij}^\varepsilon + \Pi_{ij}^\varepsilon + \mathcal{D}_{ij}^\varepsilon + \nu \nabla^2 \varepsilon_{ij}, \quad (\text{A.11})$$

where

$$\begin{aligned} \Pi_{ij}^\varepsilon &= \frac{2\nu}{\rho} \left[ \tau \left( \frac{\partial p}{\partial x_k}, \frac{\partial}{\partial x_k} \left[ \frac{\partial u_i}{\partial x_j} \right] \right) \right] + \frac{2\nu}{\rho} \left[ \tau \left( \frac{\partial p}{\partial x_k}, \frac{\partial}{\partial x_k} \left[ \frac{\partial u_j}{\partial x_i} \right] \right) \right] \\ \mathcal{D}_{ij}^\varepsilon &= -\frac{2\nu}{\rho} \left[ \frac{\partial}{\partial x_j} \left[ \tau \left( \frac{\partial u_i}{\partial x_k}, \frac{\partial p}{\partial x_k} \right) \right] \right] - \frac{2\nu}{\rho} \left[ \frac{\partial}{\partial x_i} \left[ \tau \left( \frac{\partial u_j}{\partial x_k}, \frac{\partial p}{\partial x_k} \right) \right] \right] \\ &\quad - 2\nu \frac{\partial}{\partial x_l} \left[ \tau \left( u_l, \frac{\partial u_i}{\partial x_k}, \frac{\partial u_j}{\partial x_k} \right) \right] \\ \mathcal{P}_{ij}^\varepsilon &= \frac{\partial \overline{u_j}}{\partial x_l} \varepsilon_{il} + \frac{\partial \overline{u_i}}{\partial x_l} \varepsilon_{jl} \\ &\quad + 2\nu \frac{\partial \overline{u_l}}{\partial x_k} \tau \left( \frac{\partial u_i}{\partial x_k}, \frac{\partial u_j}{\partial x_l} \right) + 2\nu \frac{\partial \overline{u_l}}{\partial x_k} \tau \left( \frac{\partial u_j}{\partial x_k}, \frac{\partial u_i}{\partial x_l} \right) \\ &\quad + 2\nu \frac{\partial^2 \overline{u_i}}{\partial x_l \partial x_k} \tau \left( \frac{\partial u_j}{\partial x_k}, u_l \right) + 2\nu \frac{\partial^2 \overline{u_j}}{\partial x_l \partial x_k} \tau \left( \frac{\partial u_i}{\partial x_k}, u_l \right) \\ &\quad + 2\nu \tau \left( \frac{\partial u_i}{\partial x_k}, \frac{\partial u_l}{\partial x_k}, \frac{\partial u_j}{\partial x_l} \right) + 2\nu \tau \left( \frac{\partial u_j}{\partial x_k}, \frac{\partial u_l}{\partial x_k}, \frac{\partial u_i}{\partial x_l} \right) \\ \Phi_{ij}^\varepsilon &= 4\nu^2 \tau \left( \frac{\partial^2 u_i}{\partial x_k \partial x_l}, \frac{\partial^2 u_j}{\partial x_k \partial x_l} \right) \end{aligned}$$

### A.2.3 Generalized $k - \varepsilon$ Equations

Defining the subfilter energy as

$$k = \frac{1}{2} \tau(u_i, u_i)$$

the subfilter energy equation can be obtained by taking one half the trace of (A.10). Noting that the pressure-strain rate correlation tensor is traceless we recover the following equation:

$$\frac{\partial k}{\partial t} + \overline{u_k} \frac{\partial k}{\partial x_k} = \nu \nabla^2 k + \mathcal{D} + \mathcal{P} - \varepsilon, \quad (\text{A.12})$$



where

$$\begin{aligned}\mathcal{D} &= -\frac{1}{\rho} \frac{\partial}{\partial x_i} [\tau(u_i, p)] - \frac{1}{2} \frac{\partial \tau(u_i, u_i, u_k)}{\partial x_k} \\ \mathcal{P} &= -\frac{\overline{\partial u_i}}{\partial x_k} \tau(u_i, u_k) \\ \varepsilon &= \frac{1}{2} \varepsilon_{ii} = \nu \tau \left( \frac{\partial u_i}{\partial x_k}, \frac{\partial u_i}{\partial x_k} \right)\end{aligned}$$

Similarly, the scalar dissipation rate equation can be obtained by taking one half the trace of (A.11):

$$\frac{\partial \varepsilon}{\partial t} + \overline{u_l} \frac{\partial \varepsilon}{\partial x_l} = \mathcal{P}^\varepsilon - \Phi^\varepsilon + \mathcal{D}^\varepsilon + \nu \nabla^2 \varepsilon, \quad (\text{A.13})$$

where

$$\begin{aligned}\mathcal{D}^\varepsilon &= -\frac{\nu}{\rho} \left[ \frac{\partial}{\partial x_i} \left[ \tau \left( \frac{\partial u_i}{\partial x_k}, \frac{\partial p}{\partial x_k} \right) \right] \right] - \nu \frac{\partial}{\partial x_l} \left[ \tau \left( u_l, \frac{\partial u_i}{\partial x_k}, \frac{\partial u_i}{\partial x_k} \right) \right] \\ \mathcal{P}^\varepsilon &= -\frac{\partial \overline{u_i}}{\partial x_l} \varepsilon_{il} - 2\nu \frac{\partial \overline{u_l}}{\partial x_k} \tau \left( \frac{\partial u_i}{\partial x_k}, \frac{\partial u_i}{\partial x_l} \right) \\ &\quad - 2\nu \frac{\partial^2 \overline{u_i}}{\partial x_l \partial x_k} \tau \left( \frac{\partial u_i}{\partial x_k}, u_l \right) - 2\nu \tau \left( \frac{\partial u_i}{\partial x_k}, \frac{\partial u_l}{\partial x_k}, \frac{\partial u_i}{\partial x_l} \right) \\ \Phi^\varepsilon &= 2\nu^2 \tau \left( \frac{\partial^2 u_i}{\partial x_k \partial x_l}, \frac{\partial^2 u_i}{\partial x_k \partial x_l} \right)\end{aligned}$$

## Appendix B

### BOUNDARY LAYER SOLVERS

The computational cost of solving the full Navier-Stokes equations necessitates another method for developing profiles for use as inflow conditions and initial data. For this work solutions of the appropriate boundary layer equations provide the required data. In the case of laminar flow a similarity solution is used, whereas in the turbulent case the boundary layer equations for the flow variables, including  $k$  and  $\varepsilon$ , are solved directly. In the following presentation, primary focus will be on areas in which the solution techniques differ from those in the literature.

#### B.1 Compressible Laminar Boundary Layer

A similarity analysis of the incompressible Navier-Stokes equations for a boundary layer results in the classical Falkner-Skan family of profiles (including the zero-pressure gradient Blasius profile). Reducing the compressible equations to a self-similar form requires a number of additional assumptions on the thermodynamic variables and material properties of the fluid. There are several transformation which can be used to obtain a self-similar form of the equations. Here we follow the approach of Illingworth (1950). Introducing the similarity variables<sup>1</sup>

$$\xi(x) = \int_0^x \rho_e(x') \mu_e(x') U_e(x') dx' \quad (\text{B.1})$$

$$\eta(x, y) = U_e(x) \sqrt{\frac{\text{Re}}{2\xi(x)}} \int_0^y \rho(x, y') dy', \quad (\text{B.2})$$

---

<sup>1</sup>The additional factor of  $\sqrt{\text{Re}}$  is due to the non-dimensionalization.

$C$	Pr	Ma	$\gamma$
1.0	0.71	0.25	1.4

TABLE B.1. Parameters for the similarity solution for the laminar boundary layer.

where the subscript  $e$  represents the external flow (outside the boundary layer), we wish to find similarity solutions of the form

$$u(\xi, \eta) = U_e(\xi)f'(\eta) \quad (\text{B.3})$$

$$h(\xi, \eta) = h_e(\xi)g(\eta). \quad (\text{B.4})$$

If we assume a perfect gas we have the following relationship for  $\rho$ :

$$\frac{\rho_e}{\rho} = \frac{T}{T_e} \approx \frac{h}{h_e} = g(\eta). \quad (\text{B.5})$$

Making the additional assumptions of constant specific heats and  $U_e = \text{const}$ ,  $H_e = \text{const}$  (corresponding to a zero-pressure gradient flat-plate) we can substitute (B.1)-(B.4) into the compressible boundary layer equations to obtain the similarity equations (White, 1991, eqs. 7-32a,b, p. 507):

$$(Cf'')' + ff'' = 0 \quad (\text{B.6})$$

$$(Cg')' + \text{Pr}fg' = -\text{Pr}C(\gamma - 1)\text{Ma}^2f''^2, \quad (\text{B.7})$$

where

$$C = \frac{\rho\mu}{\rho_e\mu_e}. \quad (\text{B.8})$$

We further assume  $C = 1$  which implies that the viscosity varies linearly with the temperature.

These equations can be solved by a shooting method (in this work the implementation is that of Press et al., 1986). Table B.1 lists the parameters used in solving for the similarity solution for the zero pressure gradient flat plate boundary layer under investigation. Unlike the incompressible case, a closed form solution for  $v$  requires

the solution of an integral equation in  $g(\eta)$ . To avoid this, the following procedure is adopted. Equation B.2 is inverted to obtain  $y(\eta)$ ,

$$\begin{aligned}\frac{\partial \eta}{\partial y} &= U_e \sqrt{\frac{\text{Re}}{2\xi}} \rho = \rho_e U_e \sqrt{\frac{\text{Re}}{2\xi}} \frac{\rho}{\rho_e} \\ \frac{\partial y}{\partial \eta} &= \frac{1}{\rho_e U_e} \sqrt{\frac{2\xi}{\text{Re}}} g(\eta) \\ y &= \frac{1}{\rho_e U_e} \sqrt{\frac{2\xi}{\text{Re}}} \int_0^\eta g(\eta) d\eta.\end{aligned}\tag{B.9}$$

At each  $x$  station, this expression is used to obtain  $y(\eta)$ . Linear interpolation is used to obtain the variable  $\rho$ ,  $u$ , and  $h$  from the similarity solution. Finally, once the entire flow field has been obtained,  $v$  can be computed from the continuity equation.

## B.2 Turbulent Boundary Layer

The boundary layer equations for a turbulent compressible fluid, including the transport equations for  $k$  and  $\varepsilon$  can be found in varying forms in the literature. For the low Mach number flows under consideration the primitive variable formulation is chosen.

The equations are:

$$\frac{\partial \bar{\rho} \tilde{u}}{\partial x} + \frac{\partial \bar{\rho} \tilde{v}}{\partial y} = 0 \tag{B.10}$$

$$\bar{\rho} \tilde{u} \frac{\partial \tilde{u}}{\partial x} + \bar{\rho} \tilde{v} \frac{\partial \tilde{u}}{\partial y} = -\frac{dp_e}{dx} + \frac{\partial}{\partial y} \left[ \left( \frac{1}{\text{Re}} + \mu_T \right) \frac{\partial \tilde{u}}{\partial y} \right] \tag{B.11}$$

$$\begin{aligned}\bar{\rho} \tilde{u} \frac{\partial \bar{T}}{\partial x} + \bar{\rho} \tilde{v} \frac{\partial \bar{T}}{\partial y} &= (1 - \gamma) \text{Ma}^2 \tilde{u} \frac{dp_e}{dx} + \frac{\partial}{\partial y} \left[ \left( \frac{1}{\text{Re Pr}} + \frac{\mu_T}{\text{Pr}_T} \right) \frac{\partial \bar{T}}{\partial y} \right] \\ &\quad + (1 - \gamma) \text{Ma}^2 \left( \frac{1}{\text{Re}} \right) \left( \frac{\partial \tilde{u}}{\partial y} \right)^2 + (1 - \gamma) \text{Ma}^2 \rho \varepsilon\end{aligned}\tag{B.12}$$

$$\bar{\rho} \tilde{u} \frac{\partial k}{\partial x} + \bar{\rho} \tilde{v} \frac{\partial k}{\partial y} = \frac{\partial}{\partial y} \left[ \left( \frac{1}{\text{Re}} + \frac{\mu_T}{\text{Pr}_k} \right) \frac{\partial k}{\partial y} \right] + \mu_T \left( \frac{\partial \tilde{u}}{\partial y} \right)^2 - \bar{\rho} \varepsilon \tag{B.13}$$

$$\begin{aligned}\bar{\rho} \tilde{u} \frac{\partial \varepsilon}{\partial x} + \bar{\rho} \tilde{v} \frac{\partial \varepsilon}{\partial y} &= \frac{\partial}{\partial y} \left[ \left( \frac{1}{\text{Re}} + \frac{\mu_T}{\text{Pr}_\varepsilon} \right) \frac{\partial \varepsilon}{\partial y} \right] \\ &\quad + C_{\varepsilon 1} \frac{\varepsilon}{k} \mu_T \left( \frac{\partial \tilde{u}}{\partial y} \right)^2 - C_{\varepsilon 2} f_{\varepsilon 2} \frac{\bar{\rho} \varepsilon^2}{k}\end{aligned}\tag{B.14}$$

The formulation given here follows that of Schlichting and Gersten (1999, eqs. 19.8-9,24) with the following additional assumptions and modifications:

1. The equations have been nondimensionalized.
2. The turbulent dissipation rate term has been restored to the temperature equation (Schlichting and Gersten, 1999, eq. 19.24, approximate it with the production,  $\bar{\rho} \widetilde{u''v''} \partial \tilde{u} / \partial y$ ).
3. The molecular diffusion terms have been restored to the  $k$  and  $\varepsilon$  equations.
4. The molecular viscosity and thermal diffusivity are assumed to be constant ( $\mu = \mu_0$  and  $\lambda = \lambda_0$ ).
5. A linear eddy-viscosity model has been substituted for the Reynolds stress term,

$$-\bar{\rho} \widetilde{u''v''} = \mu_T \frac{\partial \tilde{u}}{\partial y},$$

and for the turbulent thermal stress term,

$$-\bar{\rho} \overline{v''T'} = \frac{\mu_T}{\text{Pr}_T} \frac{\partial \bar{T}}{\partial y}.$$

Suitable wall functions have been introduced in order to make the model consistent with the form given in section 2.4.5.

The equations (B.10-B.14) can be solved using a backward Euler method marching downstream, (Tannehill et al., 1997, pp. 447-449). The equations are linearized in  $x$  by lagging the coefficients, yielding a tridiagonal system. Introducing the discretized variable  $\phi_{i,j} = \phi(x_i, y_j)$ , we can express the general advection diffusion equation for  $\phi$  as as

$$\begin{aligned} \bar{\rho}_{i,j} \tilde{u}_{i,j} \frac{\phi_{i+1,j} - \phi_{i,j}}{\Delta x} + \bar{\rho}_{i,j} \tilde{v}_{i,j} \frac{\phi_{i+1,j+1} - \phi_{i+1,j-1}}{y_{j+1} - y_{j-1}} \\ = \frac{1}{y_{j+1} - y_{j-1}} \left[ (D_{i,j+1} + D_{i,j}) \frac{\phi_{i+1,j+1} - \phi_{i+1,j}}{y_{j+1} - y_j} \right. \\ \left. - (D_{i,j} + D_{i,j-1}) \frac{\phi_{i+1,j} - \phi_{i+1,j-1}}{y_j - y_{j+1}} \right] + S_{i,j} \quad (\text{B.15}) \end{aligned}$$

where  $S_{i,j}$  is the source term.

For the zero-pressure gradient flat plate boundary layer ( $dp_e/dx = 0$ ) the equations are solved as follows. Starting at the initial station, where uniform plug flow is assumed, the  $x$ -momentum equation (B.11) is solved for  $\tilde{u}_{i,j+1}$  using the discretization described above. The remaining equations are advanced similarly with all the source terms lagged. (The source terms containing  $\tilde{u}$  could be evaluated without lagging, but for consistency with the non-linear source terms in the turbulent transport equations all source terms were lagged. Test computations showed very little difference between the two methods.) Using the equation of state (2.48) the density at the new station can be evaluated. Finally, the wall normal velocity,  $\tilde{v}$ , can be computed by integrating from the wall according to

$$\frac{\bar{\rho}_{i,j+1}\tilde{u}_{i,j+1} - \bar{\rho}_{i,j}\tilde{u}_{i,j}}{\Delta x} + \frac{\bar{\rho}_{i+1,j+1}\tilde{u}_{i+1,j+1} - \bar{\rho}_{i-1,j+1}\tilde{u}_{i-1,j+1}}{y_{i+1} - y_{i-1}} = 0. \quad (\text{B.16})$$

## REFERENCES

- C. R. Bachman. *A New Methodology for the Numerical Simulation of Wall Bounded Turbulent Flows*. PhD thesis, The University of Arizona, 2001.
- J. Bardina, J. H. Ferziger, and W. C. Reynolds. Improved subgrid models for large eddy simulation. AIAA Paper 80-1357, 1980.
- P. Batten, U. Goldberg, and S. Chakravarthy. Sub-grid turbulence modeling for unsteady flow with acoustic resonance. AIAA Paper 2000-0473, Jan. 2000. 38th Aerospace Sciences Meeting & Exhibit, Reno, NV.
- G. Berkooz. An observation on probability density equations, or, when do simulations represent statistics? *Nonlinearity*, 7:313–328, 1994.
- M. J. Boussinesq. Essai sur la théorie des eaux courantes. *Mémoires A L'académie Des Sciences De L'Institut De France: Sciences Mathématiques Et Physiques*, 23, 1877.
- D. Carati, G. S. Winckelmans, and H. Jeanmart. On the modelling of the subgrid-scale and filtered-scale stress tensors in large-eddy simulation. *J. Fluid Mech.*, 441: 119–138, Aug. 2001.
- J. W. Deardorff. A numerical study of three-dimensional turbulent channel flow at large Reynolds numbers. *J. Fluid Mech.*, 41, part 2:453–480, 1970.
- J. W. Deardorff. The use of subgrid transport equations in a three-dimensional model of atmospheric turbulence. *J. Fluids Eng.*, 95:429–438, Sept. 1973.
- J. A. Domaradzki, Z. Xiao, and P. K. Smolarkiewicz. Effective eddy viscosities in implicit large eddy simulations of turbulent flows. *Phys. Fluids*, 15(12):3890–3893, Dec. 2003.

- Y. Dubief and F. Delcayre. On coherent-vortex identification in turbulence. *J. Turb.*, 1(11), Dec. 2000.
- R. Duraiswami and A. Prosperetti. Orthogonal mapping in two dimensions. *J. Comp. Phys.*, 98:254–268, Feb. 1992.
- G. Erlebacher, M. Y. Hussaini, C. G. Speziale, and T. A. Zang. Toward the large-eddy simulation of compressible turbulent flows. *J. Fluid Mech.*, 238:155–185, 1992.
- H. F. Fasel, J. Seidel, and S. Wernz. A methodology for simulations of complex turbulent flows. *J. Fluids Eng.*, 124:933–942, Dec. 2002.
- F. N. Felten and T. S. Lund. Numerical simulation of parallel airfoil/vortex interaction using a zonal hybrid RANS/LES method. AIAA Paper 2005-5127, AIAA, 2005. 17th AIAA Computational Fluid Dynamics Conference, 6–9 June 2005, Toronto, Ontario, Canada.
- T. B. Gatski and T. Jongen. Nonlinear eddy viscosity and algebraic stress models for solving complex turbulent flows. *Prog. Aero. Sci.*, 36(8):655–682, 2000.
- T. B. Gatski and C. G. Speziale. On explicit algebraic stress models for complex turbulent flows. *J. Fluid Mech.*, 254:59–78, Sept. 1993.
- M. Germano. Turbulence: The filtering approach. *J. Fluid Mech.*, 238:325–336, 1992.
- M. Germano. From RANS to DNS: Towards a bridging model. In *Direct and Large-Eddy Simulation III: Proceedings of the Isaac Newton Institute Symposium/ERCOTAC Workshop, held in Cambridge, U. K. 12-14 May 1999*, volume 7 of *ERCOTAC*, pages 225–236, Dordrecht, 1999. Isaac Newton Institute, Cambridge England, Kluwer Academic Publishers.
- M. B. Glauert. The design of suction aerofoils with a very large  $C_L$ -range. Reports And Memoranda 2111, Aeronautical Research Council, Nov. 1945.



- M. B. Glauert, W. S. Walker, W. G. Raymer, and N. Gregory. Wind-tunnel tests on a thick suction aerofoil with a single slot. Reports And Memoranda 2646, Aeronautical Research Council, Oct. 1948.
- D. Greenblatt and I. J. Wygnanski. The control of flow separation by periodic excitation. *Prog. Aero. Sci.*, 36(7):487–545, Oct. 2000.
- D. Greenblatt, K. B. Paschal, C.-S. Yao, J. Harris, N. W. Schaeffler, and A. E. Washburn. A separation control CFD validation test case Part 1: Baseline & steady suction. AIAA Paper 2004-2220, AIAA, June 2004. 2nd AIAA Flow Control Conference, June 28–July 1, 2004, Portland, OR.
- D. Greenblatt, K. B. Paschal, C.-S. Yao, and J. Harris. A separation control CFD validation test case Part 2. Zero efflux oscillatory blowing. AIAA Paper 2005-0485, AIAA, Jan. 2005. 43rd AIAA Aerospace Sciences Meeting & Exhibit, Reno, NV.
- B. Gustafsson. The convergance rate for difference approximations to mixed initial boundary value problems. *Math. Comp.*, 29(10):396–406, Apr. 1975.
- F. H. Harlow and P. I. Nakayama. Transport of turbulence energy decay rate. Technical Report LA-3854, Los Alamos Scientific Laboratory, Los Alamos, NM, Jan. 1968.
- P. J. Harris. Numerical investigation of the supersonic plane wake using the compressible Navier-Stokes equations. Master’s report, The University of Arizona, 1995.
- M. Hénon. A two-dimensional mapping with a strange attractor. *Comm. Math. Phys.*, 50(1):69–77, 1976.
- C. Hirsch. *Numerical Computation of Internal and External Flows*. John Wiley & Sons, Chichester, 1988.

- M. Y. Hussaini, S. Thangam, S. L. Woodruff, and Y. Zhou. Development and validation of continous models for simulation of turbulent flows. In *Prooceedings of ASME FEDSM'03, 4th ASME/JSME Joint Fluids Engineering Conference*, FEDSM, 2003.
- D. M. Israel and H. F. Fasel. Numerical investigation of compressibility effects on active control of boundary layer separation. AIAA Paper 2001-2771, June 2001. 31st AIAA Fluid Dynamics Conference & Exhibit, 11-14 June 2001, Anaheim, CA.
- D. M. Israel and H. F. Fasel. Numerical investigation of turbulent separation control using periodic disturbances. AIAA Paper 2002-0409, Jan. 2002. 40th AIAA Aerospace Sciences Meeting & Exhibit, 14-17 January, 2002, Reno, NV.
- J. Jeong and F. Hussain. On the identification of a vortex. *J. Fluid Mech.*, 285:69-94, Feb. 1995.
- W. P. Jones and B. E. Launder. The prediction of laminarization with a two-equation model of turbulence. *Inter. J. Heat Mass Trans.*, 15:301-314, 1972.
- V. Krishnan, K. D. Squires, and J. R. Forsythe. Prediction of separated flow characteristics over a hump using RANS and DES. AIAA Paper 2004-2224, AIAA, 2004.
- S. L. Krist, R. T. Biedron, and C. L. Rumsey. CFL3D user's manual (version 5.0). Technical Report TM-1998-208444, NASA, June 1998.
- A. Leonard. Energy cascade in large-eddy simulations of turbulent fluid flows. *Adv. Geophysics*, 18A:237-248, 1974.
- M. Lesieur. *Turbulence in Fluids: Stochastic and Numerical Modeling*. Kluwer Academic Publishers, Dordrecht, The Netherlands, 2nd edition, 1990.

- D. K. Lilly. The representation of small-scale turbulence in numerical simulation experiments. In *Proceedings of the IBM Scientific Computing Symposium on Environmental Sciences*, pages 195–210, Yorktown Heights, NY, 1967.
- J. L. Lumley. Toward a turbulent constitutive relation. *J. Fluid Mech.*, 41, part 2: 413–434, 1970.
- J. L. Lumley, Z. Yang, and T.-H. Shih. A length-scale equation. *Flow Turb. Comb.*, 63:1–21, 1999.
- T. S. Lund. On the use of discrete filters for large eddy simulation. In *1997, Annual Research Briefs*. Center for Turbulence Research, 1997.
- L. G. Margolin and W. J. Rider. A rationale for implicit turbulence modeling. *Inter. J. Numer. Methods Fluids*, 39:821–841, 2002.
- J. C. Maxwell. On the dynamical theory of gases. *Phil. Trans. Royal Soc. Lond.*, 157: 49–88, 1867.
- J. W. Naughton, S. Viken, and D. Greenblatt. Wall shear stress measurements on the NASA hump model for CFD validation. AIAA Paper 2004-2607, AIAA, 2004. Aerodynamic Measurement Technology and Ground Test Conference, June 26–July 1, Portland, OR.
- L. G. Pack and A. Seifert. Dynamics of active separation control at high Reynolds numbers. AIAA Paper 2000-0409, Jan. 2000.
- S. Y. Pilyugin. *Shadowing in Dynamical Systems*, volume 1706 of *Lecture Notes in Mathematics*. Springer, 1999.
- U. Piomelli, E. Balaras, K. D. Squires, and P. R. Spalart. Zonal approaches to wall-layer models for large-eddy simulations. AIAA Paper 2002-3083, June 2002. 3rd AIAA Theoretical Fluid Mechanics Meeting, St. Louis, MO.

- S. B. Pope. A more general effective-viscosity hypothesis. *J. Fluid Mech.*, 72(2): 331–340, Nov. 1975.
- S. B. Pope. *Turbulent Flows*. Cambridge University Press, Cambridge, 2000.
- S. B. Pope. Large-eddy simulation using projection onto local basis functions. To appear in: “Fluid Mechanics and the Environment: Dynamics Approaches” Ed., J. L. Lumley, Springer, 2001.
- S. B. Pope. Ten questions concerning the large-eddy simulation of turbulent flows. *New J. of Phys.*, 6(35), 2003.
- L. Prandtl. Bericht über untersuchungen zur ausgebildeten turbulenz. *Ztschr f. angew. Math. und Mech.*, 5(2):136–139, Apr. 1925.
- L. Prandtl. Über ein neues formelsystem für die ausgebildete turbulenz. *Nachrichten der Akademie der Wissenschaften zu Göttingen, Mathematische-physikalische Klasse*, pages S. 6–19, 1945. Reprinted in Ludwig Prandtl *Gesammelte Abhandlungen Zur Angewandten Mechanik, Hydro- und Aerodynamik*, Ed. Walter Tollmien, Hermann Schlichting, Henry Götler, and F. W. Riegels, Springer-Verlag, Berlin, 1961, v. 2, 874–887.
- W. H. Press, B. P. Flannery, S. A. Teukolsky, and W. Vetterling. *Numerical Recipes*. Cambridge University Press, 1986.
- M. B. Priestly. *Spectral Analysis and Time Series*. Probability and Mathematical Statistics. Academic Press, London, 1981.
- N. Reau and A. Tumin. Harmonic perturbations in turbulent wakes. *AIAA J.*, 40(3): 526–530, Mar. 2002a.
- N. Reau and A. Tumin. On harmonic perturbations in a turbulent mixing layer. *Eur. J. Mech. B*, 21(2):143–155, 2002b.

- O. Reynolds. An experimental investigation of the circumstances which determine whether the motion of water shall be direct or sinuous, and of the law of resistance in parallel channels. *Phil. Trans. Royal Soc. Lond.*, 174:935–982, 1883.
- O. Reynolds. On the dynamical theory of incompressible viscous fluids and the determination of the criterion. *Phil. Trans. Royal Soc. Lond. A*, 186:123–164, 1895.
- W. C. Reynolds and A. K. M. F. Hussain. The mechanics of an organized wave in turbulent shear flow. Part 3. Theoretical models and comparisons with experiments. *J. Fluid Mech.*, 54, part 2:263–288, 1972.
- J. Rotta. Statistical theory of inhomogeneous turbulence. NASA Technical Translation TT F-14560, NASA, Oct. 1972. Translation of “Statistische Theorie nichthomogener Turbulenz. 1. Mitteilung”.
- J. Rotta. Statistische theorie nichthomogener turbulenz. 1. mitteilung. *Ztschr. f. Phys.*, 129:547–572, 1951.
- C. Rumsey, J. Thomas, G. Warren, and G. Liu. Upwind Navier-Stokes solutions for separated periodic flows. *AIAA J.*, 25:535, 1987.
- C. L. Rumsey and T. B. Gatski. Recent turbulence model advances applied to multielement airfoil computations. *J. Aircraft*, 38(5):904–910, Oct. 2001.
- C. L. Rumsey, T. B. Gatski, W. L. S. III, V. N. Vatsa, and S. A. Viken. Summary of the 2004 CFD validation workshop on synthetic jets and turbulent separation control. AIAA Paper 2004-2217, 2004.
- R. Sandberg. *Numerical Investigation of Transitional and Turbulence Supersonic Axisymmetric Wakes*. PhD thesis, The University of Arizona, 2004.

- H. Schlichting and K. Gersten. *Boundary-Layer Theory*. Springer, New York, eighth revised and enlarged edition edition, 1999. English translation of the 9th German completely revised edition. Translated by Katherine Mayes.
- H. Schmidt and U. Schumann. Coherent structure of the convective boundary layer derived from large-eddy simulation. *J. Fluid Mech.*, 200:511–562, 1989.
- U. Schumann. Subgrid scale model for finite difference simulations of turbulent flows in plane channels and annuli. *J. Comp. Phys.*, 18:376–404, 1975.
- A. Seifert and L. G. Pack. Active control of separated flows on generic configurations at high Reynolds numbers. AIAA Paper 99-3403, June 1999.
- A. Seifert and L. G. Pack. Sweep and compressibility effects on active separation control at high Reynolds numbers. AIAA Paper 2000-0410, Jan. 2000a.
- A. Seifert and L. G. Pack. Separation control at flight Reynolds numbers: Lessons learned and future directions. AIAA Paper 2000-2542, June 2000b. Fluids 2000.
- D. E. Sigeti. Survival of deterministic dynamics in the presence of noise and the exponential decay of power spectra at high frequency. *Phys. Rev. E*, 52(3):2443–2457, Sept. 1996.
- J. Smagorinsky. General circulation experiments with the primitive equations: I. the basic experiment. *Mon. Weather Rev.*, 91(3):99–164, Mar. 1963.
- P. R. Spalart and S. R. Allmaras. A one-equation turbulence model for aerodynamic flows. *Recherche Aéronautique*, 1:5–21, 1994.
- P. R. Spalart, W.-H. Jou, M. Strelets, and S. R. Allmaras. Comments on the feasibility of LES for wings and on a hybrid RANS/LES approach. In *Advances in DNS/LES, Proceedings 1st AFOSR International Conference on DNS/LES*, pages 137–147. AFOSR, Greyden Press, Columbus Ohio, Aug. 1997.

- C. G. Speziale. Computing non-equilibrium turbulent flows with time-dependent RANS and VLES. In *15th International Conference on Numerical Methods in Fluid Dynamics*, Monterey, CA, 1996.
- C. G. Speziale. Turbulence modeling for time-dependent RANS and VLES: A review. *AIAA J.*, 36(2):173–184, Feb. 1998a.
- C. G. Speziale. A combined large-eddy simulation and time-dependent RANS capability for high-speed compressible flows. *J. Comp. Phys.*, 13(3):253–274, Sept. 1998b.
- C. G. Speziale and T. B. Gatski. Analysis and modelling of anisotropies in the dissipation rate of turbulence. *J. Fluid Mech.*, 344:155–180, 1997.
- M. Strelets. Detatched eddy simulation of massively separated flows. AIAA Paper 2001-0879, Jan. 2001. 39th AIAA Aerospace Sciences Meeting & Exhibit, January 8–11, 2001, Reno, NV.
- J. C. Tannehill, D. A. Anderson, and R. H. Pletcher. *Computational Fluid Mechanics and Heat Transfer*. Taylor & Francis, Washington DC, 2nd edition, 1997.
- G. I. Taylor. Eddy motion in the atmosphere. *Phil. Trans. Royal Soc. Lond. A*, 215: 1–26, 1915.
- J. F. Thompson, Z. U. A. Warsi, and C. W. Mastin. *Numerical Grid Generation*. Elsevier Science Publishing Co., 1985. Available online at <http://www.erc.msstate.edu/publications/gridbook>.
- A. Thumm. *Numerische Untersuchungen zum laminar-turbulenten Strömungsumschlag in transsonischen Grenzschichtströmungen*. PhD thesis, Universität Stuttgart, 1991.

- A. Travin, M. Shur, M. Strelets, and P. Spalart. Detatched-eddy simulations past a circular cylinder. *Flow Turb. Comb.*, 63:293–313, 1999.
- P. G. Tucker and L. Davidson. Zonal  $k - l$  based large eddy simulations. *Comp. Fluids*, 33(2):267–287, Feb. 2004.
- E. Turkel, S. Abarbanel, and D. Gottlieb. Multidimensional difference schemes with fourth-order accuracy. *J. Comp. Phys.*, 21(1):85–113, May 1976.
- A. Uno, T. Ishihara, M. Yokokawa, K. Itakura, and Y. Kaneda. Structure of turbulence by 4096<sup>3</sup> DNS. In *Bulletin of the American Physical Society*, volume 48, page 8, East Rutherford, NJ, Nov. 2003. American Physical Society, Division of Fluid Dynamics. Gallery of Fluid Motion.
- E. R. van Driest. On turbulent flow near a wall. *J. Aero. Sci.*, pages 1007–1011, 1036, Nov. 1956.
- T. Veldhuizen. Techniques for scientific C++. Computer Science Technical Report 542, Indiana Universit, Aug. 2000.
- D. von Terzi. *Numerical Investigation of Transitional and Turbulent Backward-Facing Step Flows*. PhD thesis, The University of Arizona, 2004.
- F. M. White. *Viscous Fluid Flow*. McGraw Hill, New York, 2nd edition edition, 1991.
- A. Yoshizawa. A statistically-derived subgrid model for the large-eddy simulation of turbulence. *Phys. Fluids*, 25(9):1532–1538, Sept. 1982.
- T. A. Zang, R. B. Dahlburg, and J. P. Dahlburg. Direct and large-eddy simulations of three-dimensional compressible Navier-Stokes turbulence. *Phys. Fluids A*, 4(1): 127–140, Jan. 1992.